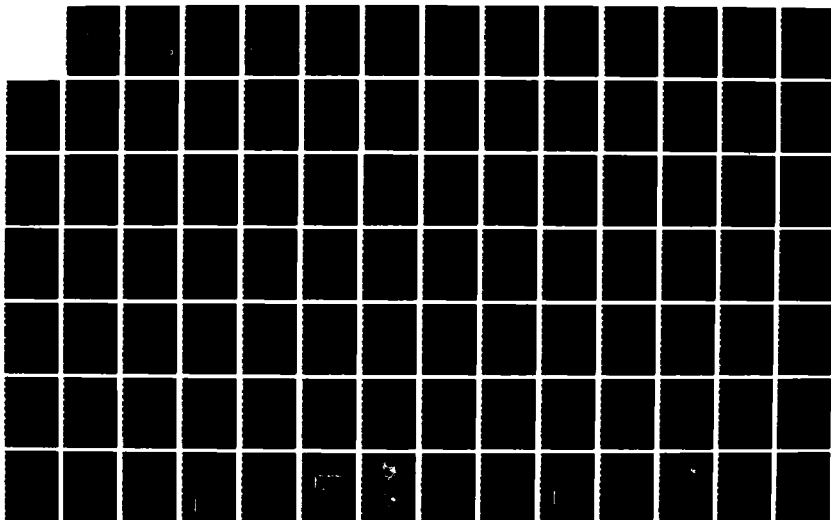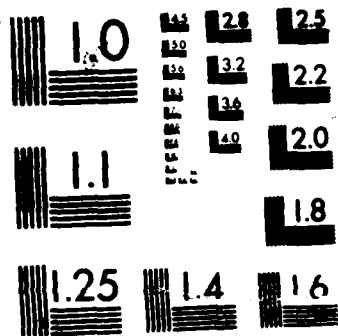AD-A179 792   ALTERNATIVE FORMS OF MOISTURE INFORMATION IN 4-D DATA   1/2
               ASSIMILATION(U) SASC TECHNOLOGIES INC LEXINGTON MA
               D C NORQUIST 15 SEP 86 SCIENTIFIC-11 AFGL-TR-86-0194
UNCLASSIFIED   F19628-82-C-0023   F/G 4/1   NL

MICROCOPY RESOLUTION TEST CHART
NATIONAL BUREAU OF STANDARDS 1963-A

AFGL-TR-86-0194

ALTERNATIVE FORMS OF MOISTURE INFORMATION
IN 4-D DATA ASSIMILATION

AD-A179 792

Donald C. Norquist

SASC Technologies, Inc.
109 Massachusetts Avenue
Lexington, MA 02173

September 15, 1986

Scientific Report No. 11

AIR FORCE GEOPHYSICS LABORATORY
AIR FORCE SYSTEMS COMMAND
UNITED STATES AIR FORCE
HANSCOM AFB, MASSACHUSETTS 01731

87 4 28 078

This technical report has been reviewed and is approved for publication.

ALLAN J. BUSSEY
Contract Manager

FOR THE COMMANDER

ROBERT A. McCLATCHEY, Director
Atmospheric Sciences Division

REPORT DOCUMENTATION PAGE

1a. REPORT SECURITY CLASSIFICATION	1b. RESTRICTIVE MARKINGS
UNCLASSIFIED	

2a. SECURITY CLASSIFICATION AUTHORITY	3. DISTRIBUTION/AVAILABILITY OF REPORT
	Approved for public release; distribution
2b. DECLASSIFICATION/DOWNGRADING SCHEDULE	unlimited

4. PERFORMING ORGANIZATION REPORT NUMBER(S)	5. MONITORING ORGANIZATION REPORT NUMBER(S)
	AFGL-TR-86-0194

6a. NAME OF PERFORMING ORGANIZATION	6b. OFFICE SYMBOL (If applicable)	7a. NAME OF MONITORING ORGANIZATION
SASC Technologies, Inc.		Air Force Geophysics Laboratory

6c. ADDRESS (City, State and ZIP Code)	7b. ADDRESS (City, State and ZIP Code)
109 Massachusetts Avenue Lexington, MA 02173	Hanscom AFB, MA 01731

8a. NAME OF FUNDING/SPONSORING ORGANIZATION	8b. OFFICE SYMBOL (If applicable)	9. PROCUREMENT INSTRUMENT IDENTIFICATION NUMBER
Air Force Geophysics Laboratory	LY	Contract No. F19628-82-C-0023

8c. ADDRESS (City, State and ZIP Code)	10. SOURCE OF FUNDING NOS.			
	PROGRAM ELEMENT NO.	PROJECT NO.	TASK NO.	WORK UNIT NO.
Hanscom AFB, MA 01731	62101F	6670	00	AC

11. TITLE (Include Security Classification) Alternative Forms of Moisture Information in 4-D Data Assimilation

12. PERSONAL AUTHOR(S)
Norquist, Donald C.

13a. TYPE OF REPORT	13b. TIME COVERED	14. DATE OF REPORT (Yr., Mo., Day)	15. PAGE COUNT
Scientific Rpt. No. 11	FROM _____ TO _____	1986/9/15	144

16. SUPPLEMENTARY NOTATION

17. COSATI CODES			18. SUBJECT TERMS (Continue on reverse if necessary and identify by block number)
FIELD	GROUP	SUB. GR.	Data Assimilation/ Normal Mode Initialization
0401			Humidity, Sources
0402			Collocation Studies,

analysis over maintaining the first guess when both were compared with verifying observations. Finally, the sensitivity of the AFGL GSM to initial humidity states was tested by initializing a series of 48h forecasts from several humidity fields. The NMC-1981 version of the GSM without convective adjustment was found to be largely insensitive to specification of initial moisture, with the model establishing its moisture bias profile irrespective of specified initial humidity conditions. (Keywords;)

Accession For	
NTIS GRA&I	☒
DTIC TAB	☐
Unannounced	☐
Justification	

By	
Distribution/	
Availability Codes	
Dist	Avail and/or Special
A-1	

QUALITY
INSPECTED
1

TABLE OF CONTENTS

I. INTRODUCTION

Various methods of four-dimensional data assimilation have been in practice both operationally and in a data archival mode over the past ten years. Most current methodologies use a global objective analysis procedure, an initialization program to remove gravity modes and their tendencies, and a short-term (usually 6h) global forecast model to step ahead to the next time period. An example of an operational global data assimilation system is that used at the National Meteorological Center (NMC) (Dey and Morone, 1985), while the European Centre for Medium Range Weather Forecasts (ECMWF) has used its data assimilation procedure for the formulation of the FGGE III-B analysis archives (Bengtsson et al., 1982) as well as for operational purposes (Lorenc, 1981).

Until recently, the focus of attention in the development and use of four-dimensional data assimilation systems has been on mass and motion fields. Although the NMC objective analysis procedure, the optimum interpolation method, does use analyzed winds and temperatures in its special univariate horizontal and vertical correlation functions for relative humidity, the observational data used in the analysis are limited to rawinsonde and surface weather observation measured humidities. Operationally, ECMWF has analyzed integrated water vapor mixing ratio of layers using measured temperature and dewpoint from rawinsonde reports and relative humidity inferred from four layers below 300 mb from surface weather observations (Tibaldi, 1982). Recently, the use of layer precipitable water from satellite soundings has been studied at ECMWF (Lönnborg, private communication) but as yet it has not been included in its operational optimum interpolation procedure for moisture. Therefore, the large regions of the globe where conventional observations of humidity are sparse or non-existent are not updated in the analysis phase of the assimilation, and in these regions the forecast model is allowed to create its own moisture climatology.

An accurate depiction of cloud distribution is of great importance in Air Force operations, in both the analysis and forecast modes. Thus, it is essential that some kind of updating of the forecast humidity field take place in data void regions to ensure the best possible representation of clouds in those regions from both the present analysis and forecast humidities. Obviously, the expense of attempting to cover data

1

void regions adequately with conventional observations on a routine basis would be prohibitive, so other forms of humidity information must be sought for such regions. Previously mentioned satellite profiles of layer precipitable water offer some hope if they are recovered from satellite radiance measurements with sufficient accuracy. Another form of global moisture information that may prove useful in updating forecast humidities is relative humidities inferred from cloud cover values of automated nephanalyses. One source of cloud analyses is the 3DNEPH cloud analysis procedure of the Air Force Global Weather Central (AFGWC) (Fye, 1978).

This report focuses on the use of such alternative forms of humidity information to supplement conventional humidity observations in preparing global analyses of relative humidity in a data assimilation environment. Humidities derived from satellite soundings and inferred from surface weather observations (SWO) and AFGWC cloud analyses (3DN) are studied for possible use in the AFGL Statistical Analysis Program (ASAP), and data assimilation sequences are run with and without the more promising forms of alternative humidity information. Conclusions are then drawn from the results as to the effect on both humidity analysis climatologies and humidity forecasts of using such supplemental humidity information.

II. DESCRIPTION OF THE GLOBAL AFGL DATA ASSIMILATION SYSTEM (AGDAS)

The triad of objective analysis, initialization, and global forecast model programs used in the global AFGL data assimilation system consists of the ASAP optimum interpolation (OI) analysis, the Machenhauer non-linear normal mode initialization (NMI) (Ballish, 1980) using four vertical modes and two iterations, and the AFGL global spectral model (GSM) (Brenner et al., 1982). The AFGL GSM used in this study was modified in the structure of its numerics from the NMC spectral model (Sela, 1980), but changed in the physics only to allow for a different distribution of vertical layers. Two later upgrades of the physics parameterizations (NMC 1983, NMC 1985) have since been carried out in the NMC operational GSM. A 30 wave rhomboidal truncation on 12 σ layers is used in the NMI and GSM, and the analysis is performed on σ layers in the ASAP to avoid vertical interpolation of fields between pressure levels and σ layers. The remainder of the description in this section concerns the OI procedure ASAP.

Originally, ASAP was developed directly from the 1979 multivariate OI procedure as described by Bergman (1979); in fact, the codes were developed

2

using only Bergman's article and the companion paper by McPherson et al., (1979) as references. With some assistance from NMC personnel (Morone, 1983, private communication), a multivariate temperature (T) and zonal (u) and meridional (v) wind component analysis code on σ layers and a separate surface pressure OI analysis code were formulated. The surface pressure analysis was later dropped and the T, u, v, σ layer analysis was replaced by a height (Z), u, v, analysis on σ layers. The equations for computing the corrections for an analysis grid point based on weighted sums of surrounding observation-minus-first guess residuals for the normalized analysis error, and for the computation of the horizontal and vertical correlation functions from Bergman are used without modification. Still later, cycling of the analysis error and the great circle distance method for correlation functions equatorward of 70° latitude were included as described by Dey and Morone (1985) without changing the Bergman formulation (including map factor) for latitudes $|\phi| \geq 70°$. The following paragraphs give a detailed description of the four codes that make up ASAP.

A. The Pre-Analysis Program (PRANAL)

PRANAL converts spectral coefficients of absolute vorticity (η), divergence (D), T, specific humidity (q, carried only in the lowest seven σ layers), and surface pressure p_* from the previous forecast (first guess) to grid point values on both the analysis grid (61 equally spaced longitudes by 62 Gaussian latitudes) and the interpolation grid (1° latitude x 1° longitude). Thus, values of T, u, v, relative humidity (r), and p_* are located on the respective grids on 12 σ layers for T, u, v, and seven σ layers for r, representing the first guess. In PRANAL, each grid value of T, q, and p_* is used to compute the corresponding grid value of r using the relations

$$r_\ell = e_\ell / e_{s_\ell} \tag{1}$$

$$e_{s_\ell} = 6.11 \exp\{19.9274 - 5443.3618 / T_\ell\} \tag{2}$$

$$e_\ell = w_\ell p_* \sigma_\ell / (1 + w_\ell) \tag{3}$$

$$w_\ell = q_\ell / [\epsilon(1 - q_\ell)] \ ; \ \epsilon = .622 \tag{4}$$

where the subscript ℓ represents the index of the σ layer. In addition, PRANAL also converts the spectral coefficients of height analysis error (α_z)(12 σ layers) and relative humidity analysis error α_r (seven σ layers) from the previous analysis to 61x62 grid values. In cases where the present cycle is the first in a series, the analysis error conversion is not performed in PRANAL, since no previous analysis in that series exists.

B. The Mass-Motion Analysis Program (ASAPOI)

The upper air analysis of Z, u, v is multivariate and is carried out at the sigma layer surfaces of the GSM forecast. Fig. 1 shows the relative positions of the sigma layers (σ_ℓ) and sigma levels (σ_ℓ) currently used in the AGDAS. Horizontal (μ) and vertical (ν) correlation functions for the autocorrelations and cross-correlations involving Z, u, v used are those given by Bergman (1979) for latitudes ϕ such that $|\phi| \geq 70°$, and by Dey and Morone (1985) for $|\phi| < 70°$. The respective distance formulations from the two articles, as well as the values for constants from Dey and Morone, are used. ASAPOI also uses the rawinsonde, pibal, and single-level wind observation error standard deviation values from Dey and Morone, but uses standard deviation values for satellite height observation errors derived from a collocation study with rawinsondes to be discussed later in this report. Values for k_h, the constant in the horizontal autocorrelation function for Z, are the same as those specified by Dey and Morone, but are used at σ layers 1-9, σ layers 10 and 11, and σ layer 12 respectively.

Because the analysis is performed on the σ layers rather than on pressure surfaces, representations of the various types of observations used in the analysis must be obtained at the pressure levels of the σ layers at each observation site. Interpolation procedures used for this purpose are discussed in detail in the following section. ASAPOI inputs four types of observations from the FGGE II-B data sets: (1) Type 1 observations, which include rawinsondes, pilot balloons (pibals), dropsondes and other direct profiling instruments, (2) Type 4 observations, which are the satellite soundings of layer mean temperature and layer precipitable water, (3) Type 2 observations, aircraft observations, and (4) Type 6, single level cloud track wind observations. Each data type is ordered by latitude from south to north prior to its use in ASAPOI, in order to facilitate the location of

$$\hat{\sigma}_{12} = .000$$
$$\sigma_{12} = .021$$
$$\hat{\sigma}_{11} = .050$$
$$\sigma_{11} = .074$$
$$\hat{\sigma}_{10} = .100$$
$$\sigma_{10} = .124$$
$$\hat{\sigma}_{9} = .150$$
$$\sigma_{9} = .175$$
$$\hat{\sigma}_{8} = .200$$
$$\sigma_{8} = .225$$
$$\hat{\sigma}_{7} = .250$$
$$\sigma_{7} = .275$$
$$\hat{\sigma}_{6} = .300$$
$$\sigma_{6} = .337$$
$$\hat{\sigma}_{5} = .375$$
$$\sigma_{5} = .436$$
$$\hat{\sigma}_{4} = .500$$
$$\sigma_{4} = .574$$
$$\hat{\sigma}_{3} = .650$$
$$\sigma_{3} = .724$$
$$\hat{\sigma}_{2} = .800$$
$$\sigma_{2} = .862$$
$$\hat{\sigma}_{1} = .925$$
$$\sigma_{1} = .962$$
$$\hat{\sigma}_{*} = 1.0$$
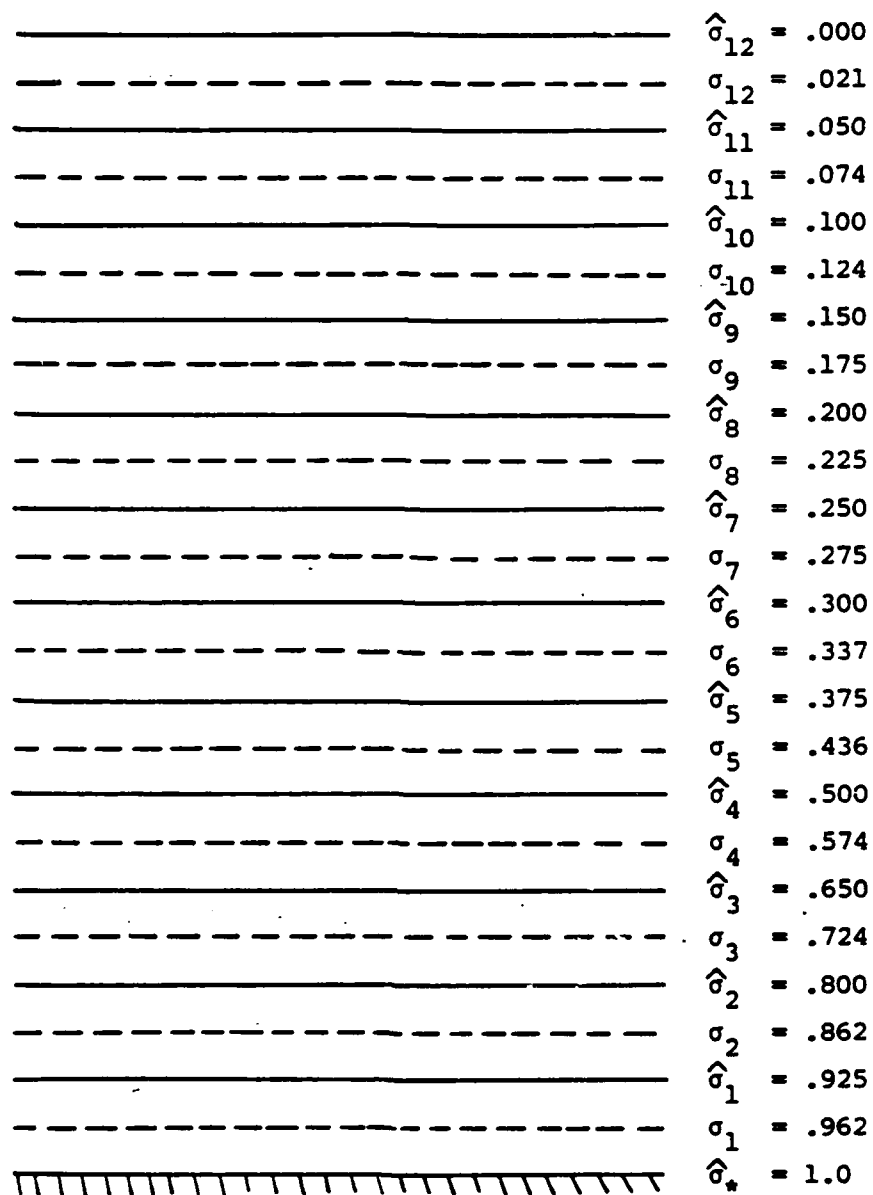
$$\sigma_k = \left[\frac{\hat{\sigma}_k^{1+\kappa} - \hat{\sigma}_{k+1}^{1+\kappa}}{(1+\kappa)(\hat{\sigma}_k - \hat{\sigma}_{k+1})} \right]^{(1/\kappa)} \quad ; \quad \kappa = R/C_p$$

Fig. 1 Distribution of σ Layers and Levels

5

the proper latitudes of 1° x 1° first guess values from which to interpolate
bilinearly to each observation site as it is processed. This horizontal
interpolation to the observation location is performed for the σ layer
variables T, u, v, r, and for p_*. Then σ layer T is converted to σ
level Z using

$$Z^\wedge_{\sigma_\ell} = Z^\wedge_{\sigma_{\ell-1}} + (R/g)T_{\sigma_\ell} \ln(\sigma^\wedge_{\ell-1}/\sigma^\wedge_\ell) \quad , \ell = 1, 2,..., L \quad (5)$$

where $Z^\wedge_{\sigma_0} = Z_*$, the model terrain height interpolated from the 1° x 1°
grid, and $\sigma^\wedge_L = 0.01$ for the purposes of establishing a value of Z for the
uppermost level. These values of Z, u, v, r are subtracted from the
corresponding estimates of observation values of Z, u, v, r to form the
residuals used in the analysis. The residuals are stored sequentially in a
data list in the order they are processed, from south to north for each data
type in turn.

ASAPOI then calls a quality control procedure that performs a "gross"
check and "buddy" check of the Z, u, v residuals. Residuals are sorted by
location into buddy check boxes that are 10° in latitude extent and
approximately equal in longitude extent, with the number of boxes for each
latitude band equal to NBOXES = 36* cos ϕ, where ϕ is the central
latitude of each band. For boxes whose central latitude lies poleward of
70° latitude, all wind component residuals are converted from
latitude-longitude (ϕ, λ) orientation to Cartesian (x, y) orientation
using

$$du_{x,y} = -du_{\phi,\lambda} \sin \lambda - I_H dv_{\phi,\lambda} \cos \lambda$$

$$dv_{x,y} = I_H du_{\phi,\lambda} \cos \lambda - dv_{\phi,\lambda} \sin \lambda$$

$$\left. \right\} \quad (6)$$

in which du, dv represent the wind component residuals, λ the observation
longitude, and I_H = 1 for Northern Hemisphere and -1 for Southern
Hemisphere. Next, the gross check is performed for each box by first
computing the forecast error standard deviation for each individual residual
at its respective level (Z) or layer (u, v) by vertically interpolating the
values in Table 1 to the σ pressure. If a residual exceeds three times
the size of the forecast error standard deviation value interpolated from

Table 1. NMC Forecast Error Standard Deviations Values (from Dey, 1983)

LATITUDE	90S-10S			10S-10N			10N-30N			30N-50N			50N-90N		
Pressure (mb)	Z (m)	u (m sec^{-1})	v	Z	u	v	Z	u	v	Z	u	v	Z	u	v
1000	25.4	4.2	4.1	14.7	3.5	3.3	19.4	4.1	3.9	19.7	4.6	4.9	21.6	4.4	4.3
850	25.4	3.9	3.7	15.5	3.2	2.8	16.7	3.7	3.4	19.6	4.1	4.3	19.4	3.6	3.6
700	26.8	4.2	4.1	19.3	3.6	3.3	18.7	4.1	3.6	19.7	4.2	3.8	20.8	3.6	3.6
500	33.5	4.8	4.6	25.4	4.3	3.5	25.6	4.8	4.2	23.2	4.8	4.6	25.8	4.4	4.4
400	39.2	5.5	5.7	29.6	4.1	4.0	32.4	5.3	4.9	27.2	5.6	5.3	29.9	5.3	5.0
300	47.0	6.6	6.8	40.1	5.8	5.3	42.3	6.5	6.1	34.1	7.1	6.4	36.5	5.7	5.5
250	50.6	9.5	7.3	49.4	5.8	5.2	47.3	7.3	6.9	37.4	6.6	6.6	39.2	5.4	5.3
200	53.5	7.3	7.0	55.3	7.8	5.8	56.3	7.6	7.6	41.6	6.7	6.2	42.0	4.4	4.3
150	57.3	6.5	6.7	61.4	8.2	5.7	67.4	7.3	7.1	46.7	5.9	4.9	48.3	3.7	3.7
100	69.8	7.0	6.4	78.0	8.8	7.1	80.1	7.7	6.2	55.2	5.1	4.1	59.4	3.7	3.6
70	77.7	6.6	5.5	93.2	7.7	4.8	100.0	5.7	5.3	64.2	7.1	4.9	71.8	5.5	5.1
50	90.1	8.3	8.0	108.0	9.9	8.3	101.0	8.7	8.6	78.3	8.2	6.7	88.1	7.6	7.4

7

Table 1 it is removed. If either wind component fails this gross check, both are removed.

The buddy check is then performed univariately within each box at each level by computing total autocorrelations for each respective residual, and determining if the criteria

$$|dZ_i - dZ_j| \leq (a - b\rho_{ij}^{ZZ})\delta_{Z_i}^f$$

$$|du_i - du_j| \leq (a - b\rho_{ij}^{uu})\delta_{u_i}^f \qquad (7)$$

$$|dv_i - dv_j| \leq (a - b\rho_{ij}^{vv})\delta_{v_i}^f$$

are met. In these expressions, i and j are the indices of two observations being compared, $\delta_{Z_i}^f$, $\delta_{u_i}^f$, $\delta_{v_i}^f$, are the forecast error standard deviation values computed from Table 1 for the respective variables at the location i, ρ_{ij} are the spatial autocorrelations and a = 3.0, b = 1.5. If the criteria are met for the comparison of residuals and i and j and $\rho_{ij} \geq$ 0.75, the observation considered to be of higher quality is assigned a keep flag; if they are of equal quality, both are assigned keep flags. For wind residuals, ρ_{ij} for u and v must be ≥ 0.75. If the criterion is not met, the lesser quality observation is assigned a toss flag, and both get a toss flag if they are of equal quality. Separate keep and toss flags for wind components are not maintained--a wind keep flag is assigned if ρ_{ij} for both u and v is ≥ 0.75, and a wind toss flag is assigned if either u or v fails the buddy check criterion. The 0.75 factor is used to insure that only more spatially correlated observations corroborate each other.

Quality level in the buddy check is defined by observation type and whether or not a vertical consistency check was conducted for that observation. Only FGGE II-B observations with quality control indices of 0 (no check made) and 1 (observation found correct in vertical consistency check) are used in the analysis, with the latter given the higher quality level. The quality control indicator (QCI) assigned to a residual for the purposes of determining comparative quality is set as follows: QC = 0 for vertically checked data and = 1 for vertically unchecked observations. Then

for Type 1 data, QCI = QC+1, while QCI for Types 2, 4, and 6 are given by QCI = 3(QC+3)+ITBI, where ITBI = 1 for Type 2, 2 for Type 4, and 3 for Type 6. For example, a QC value of 0 will correspond to QCI = 1 for Type 1, 10 for Type 2, 11 for Type 4, and 12 for Type 6. Thus, the higher the value of QCI, the poorer the quality assumed for the residual. In this way, the conventional upper air data (Type 1) will never be flagged by other observation types.

Once all of the observation intercomparisons are made in a particular box for a particular level, each observation is checked to see if it has two or more keep flags. If so, all toss flags are removed from the observation since it is to be retained regardless of how many toss flags it has received. Observation iterative rejection begins with summation of toss flags assigned to each residual, and the residual of each type (heights and winds separately) with the largest number of toss flags is identified. This residual, along with all others that have within four of that maximum number, is eliminated, and the toss flags that they imposed on the remaining residuals are removed. The remaining residual of each variable with the largest number of toss flags is identified; it and others within four toss flags of it are eliminated, the imposed toss flags on other residuals are removed, and so on. The four flag check is removed once the highest number of toss flags falls below four. This continues until all residuals of height and winds have at most one toss flag, or ten iterations have been carried out, whichever comes first. Remaining residuals are candidates for the OI analysis. The wind residuals in boxes whose central latitude is poleward of 70° are converted back to ϕ, λ orientation.

A number of points (PTS) is assigned to each observation, whether sounding or single level. For each σ level of a particular observation, if a height observation is present, PTS is added to the sum for the observation. For wind observations at each σ layer, one point is added to the sum, then if the wind observation is accompanied by a height observation at the sigma level just above it, an additional value of PTS is added. Here, PTS has a value of 1.0 for all observation types except Type 4, where PTS = 0.42. This lower factor represents the overall reliability (ratio of observation error standard deviation for rawinsonde heights to that computed for satellite sounding heights) of satellite soundings compared with conventional height observations. The total number in points for each

9

observation over all levels is stored and used later in the selection of
observations lying around an analysis point. It can be seen that the more
information contained in an observation, the larger its number of points--it
has more information to contribute to a particular location on the analysis
grid.

At this point, the set of observation-minus-first guess residuals
contains checked residuals of Z on σ levels and u, v on σ layers where
they exist in each observation, as well as unchecked residuals of r on σ
layers. Observations have been assigned points and are ordered within each
type by latitude. The analysis of the 61x62 grid points then begins with
the southern-most Gaussian latitude and the Greenwich Meridian, moving
eastward. For each analysis point, the following sequence of steps takes
place to determine the NSNDS (currently 8) observations that will be used to
update the first guess values at all σ layers. First, the Type 1
observations are considered, by computing the horizontal height
autocorrelation μ_{ig}^{ZZ} between each observation i and the grid point g. Before
NSNDS observations with $\mu_{ig}^{ZZ} \geq 0.1$ are collected, any observations failing this
criterion are no longer considered. When NSNDS such observations are found,
each successive observation's value of μ_{ig}^{ZZ} is multiplied by PTS, and this product
is compared with the same product for the NSNDS observation, where observations
1, 2, ..., NSNDS already collected are ordered from largest to smallest value
of this product. If a subsequent observation's value of μ_{ig}^{ZZ}*PTS is larger than
that for the last observation in the collection, the latter is excluded from
consideration. Making the test for inclusion on μ_{ig}^{ZZ} rather than on μ_{ig}^{ZZ} *PTS
for the first NSNDS observations avoids making the amount of information in
an observation a criterion for its inclusion for analysis points in data
sparse areas. However, in data rich areas the combination of nearness to
the grid point and amount of information influences an observation's chances
for participation in the analysis. This procedure continues until all Type
1 observations have been considered. If less than NSNDS observations have
been found from the complete set of Type 1 observations, the entire set of
Type 4 observations is compared against the accepted Type 1's in the same
manner. If NSNDS surrounding observation sets still have not been found,
the Type 2 and Type 6 sets are considered in order. Thus the search
continues through the four data types in this order, discontinuing after

10

considering in its entirety the first data type set in which the collection of NSNDS observations has been completed. The entire set of NSNDS observations is a candidate for participation in the procedure that corrects that grid point's first guess values at all model layers. In the present version of the analysis, NSNDS = 8, but a correction can take place even if only one observation has a $\mu_{ig}^{ZZ} \geq 0.1$. If no observations satisfy this condition, no correction is calculated for the analysis point at any layer.

The purpose for assigning points to the observations is to indicate how much that observation could contribute to correct the grid point values at all σ layers. For example, based on the current point system used, a complete rawinsonde observation for a 12 layer model structure would have 36 points, 5.04 points for a complete satellite sounding, and 1 point for an aircraft or single level satellite. This means that a complete rawinsonde observation located 7.14 times farther from the analysis point than a complete satellite sounding or 36 times farther than an aircraft or single level satellite wind observation would have equal likelihood of being chosen for that grid point in data rich regions. In data sparse regions where there are fewer than NSNDS of all types nearby, the observation types have equal opportunity. Types of data are processed in·the indicated order because of the perceived accuracy of the observations and the number of residuals generally present in each type. Conventional upper air sounding is seen as the most accurate and as having the most residuals. Satellite soundings are taken next because of the complete set of height residuals they provide, then aircraft winds which are more accurate than satellite winds.

Once the observations are collected for a particular analysis point, the OI procedure begins. For the first analysis in the assimilation sequence, the forecast error standard deviation relation $\delta_u = \delta_v = \delta_z [(2k_h)^{1/2} g/f_g]$, where k_h is the constant in the height autocorrelation function, g is acceleration due to gravity, and f_g is the coriolis parameter at the analysis point, is used to compute δ_u, δ_v poleward of 25° latitude using the δ_z values in Table 1. Within 25° of the equator, δ_u, δ_v values derived in this way are blended with tropical values following Dey and Morone (1985). Then mandatory level values are linearly interpolated in ln p (natural logarithm of pressure) to the sigma layer pressures. For subsequent analyses in an assimilation series, the analysis error values for Z (α_z) from all layers of that analysis point from the previous analysis are read into the code, having previously been

11

converted from spectral form. Values for the 6h height forecast error growth amount for each sigma layer, estimated from interpolating the corresponding mandatory pressure level values from Dey and Morone (1985) to the sigma layers, are added to α_z to form δ_z. However, before this addition takes place, the α_z values are checked to make sure that they are greater in magnitude than the 6h forecast error growth amount, yet less than the climatological limit for height forecast error interpolated to the sigma layers from the mandatory level Dey and Morone values. Therefore, the δ_z values are allowed to range between twice the 6h forecast error growth amount as a lower limit and the sum of the climatological limit and the 6h forecast growth amount as an upper limit. From these values, the expression $(2k_h)^{1/2}g/f_g$ was used poleward of 25° and blending with tropical values was used equatorward of 25° to obtain δ_u, δ_v values at all σ layers for the analysis point. The forecast error standard deviation values assigned to each residual i, δ_{z_i}, δ_{u_i}, δ_{v_i}, is the analysis σ layer value for the same variable at the location of the analysis point in the horizontal and at the σ layer pressure of the analysis point closest to the pressure of the observed residual in the vertical. Thus, local homogeneity of the forecast error standard deviation is assumed for the horizontal but not for the vertical.

Next, the NLRHS (presently 10) individual σ level height or σ layer wind (both components taken together) residuals to be used in the computation of a particular σ layer's values of corrections ΔZ, Δu, Δv are selected from the NSNDS set of observations. For each residual z_{o_i}, u_{o_i}, v_{o_i} in the complete set, all auto- and cross-correlations with the sigma layer analysis point are computed and divided by $1 + c_i^2$, where c (normalized observation error) is the ratio of the observation error standard deviation ξ_i for that residual to the forecast error standard deviation δ_i for that residual. These divided correlations ρ_{ig}^{zz}, ρ_{ig}^{zu}, and ρ_{ig}^{zv} for each height residual z_{o_i} and ρ_{ig}^{uz}, ρ_{ig}^{uu}, ρ_{ig}^{uv}, ρ_{ig}^{vz}, ρ_{ig}^{vu}, ρ_{ig}^{vv} for each wind residual pair u_{o_i}, v_{o_i} are used as a basis for the selection for the NLRHS height and wind residuals used to compute all three of ΔZ, Δu, Δv. It was noticed that by choosing the 10 closest residuals to the grid point (i.e., largest

12

values of ρ_{ig}^{ZZ} for all residuals) on the basis of distance alone, many times the closest observations had the lowest actual correlation with the grid point. By dividing the correlation by $1 + c_i^2$, the observation's reliability is used as a factor in its selection. Less reliable observations, with their larger value of c_i, will not have as much influence in the analysis. Since the NLRHS residuals selected will affect the computation of ΔZ, Δu, and Δv, it was thought to be important to consider the combined correlations of each residual with grid point Z, u, and v. Thus, the sum of the absolute values of $\rho_{ig}^{ZZ'}$, $\rho_{ig}^{Zu'}$, $\rho_{ig}^{Zv'}$ for each height residual and half the sum of the absolute values of $\rho_{ig}^{uZ'}$, $\rho_{ig}^{uu'}$, $\rho_{ig}^{uv'}$, $\rho_{ig}^{vZ'}$, $\rho_{ig}^{vu'}$, $\rho_{ig}^{vv'}$ for each pair of wind component residuals were compared against each other, and the NLRHS residuals with the highest values of these sums (all of which had to be ≥ 0.1) are those chosen for the analysis at the σ layer. If fewer than NLRHS residuals are found to have sums ≥ 0.1, only those that do are used. In this way, the number of individual residuals (Z, u, and v separately) can be as low as one (if only one Z residual is identified) and as large as $2 \times$ NLRHS (if NLRHS wind residuals have the largest sums, to the exclusion of any Z residuals). No limit is imposed on the number of height or wind residuals that may be selected from a particular observation. Because height residuals are carried at σ levels and wind residuals are at σ layers, correlations with σ layer analysis points favor wind residuals because of their larger value of the vertical correlation v_{ig}^{ZZ} that is used for all residuals. However, this is offset somewhat by the relative magnitudes of c_Z and $c_{u,v}$ at most levels. Values of the ratio $c_Z/c_{u,v}$ shown in Table 2 were computed for three latitudes and 12 mandatory levels using the relationship

$$c_Z/c_{u,v} = \frac{(2k_h)^{1/2} g \xi_Z}{f \xi_{u,v}} \tag{8}$$

where values of the observation error standard deviation for heights (ξ_Z) and winds ($\xi_{u,v}$) for rawinsondes from Table 5 of Dey and Morone (1985) as used in the ASAPOI, are used. For levels below 200 mb and latitudes poleward of $30°$, the lower value of c_Z reduces the correlations divided by $1 + c_i^2$ for heights less than the divided wind

13

Table 2. $c_Z/c_{u,v}$ for Rawinsonde Observations for Three Latitudes

MB	30°	45°	60°
1000	1.045	.7391	.6035
850	1.1946	.8447	.6897
700	1.1007	.7783	.6355
500	.9566	.6764	.5523
400	.9535	.6743	.5505
300	.9718	.6871	.5610
250	1.1571	.8182	.6681
200	1.2619	.8923	.7286
150	1.4760	1.0437	.8522
100	1.6675	1.1791	.9627
70	3.0022	2.1229	1.7333
50	2.8899	2.0434	1.6685

correlations with the larger value of $c_{u,v}$. The offsetting of these two factors led to a good overall blend of height and wind residuals used in the correction computations over the entire globe.

The coefficient of geostrophy G_i used in the horizontal height-wind cross-correlations equatorward of 70° latitude (see Dey and Morone's Eqs. B2-B5) for both observation-analysis point correlations and observation-observation correlations is a blend of the two proposed by Bergman (1979) and Dey and Morone (1985). It was seen that the diminishing of the coupling to zero between 25° and 10° was important, yet the sudden change of G_i vs. latitude in the vicinity of 25° was perceived as being too sharp, leading to artificially large differences between the height-wind cross-correlations between two residuals separated by just a few degrees of latitude. This sudden change was reduced by proposing the use of Bergman's expression (Eq. 3.20) poleward of 25°, then its value at 25° times the Dey-Morone expression (Eq. B10) value between 10° and 25°, with $G_i = 0$ equatorward of 10°. A curve of G_i is shown in Fig. 2 as a function of latitude, along with the curve of $(2k_h)^{1/2}g/f_i$ for $k_h = 2 \times 10^{-12}$ m^{-1} down to 25°. The latter curve is shown to illustrate how the ratio of $\delta_{u,v}$ to δ_z, used to convert normalized weights to actual weights in heights correcting winds, changes with latitude. Between 0° and 25° this curve varies with pressure level because of the tropical blending to form $\delta_{u,v}$; values of $\delta_{u,v}/\delta_z$ for 500 mb are plotted as a dashed curve on Fig. 2. Using these values of G_i, it is seen that the relationships between mass and wind are primarily geostrophic poleward of 25°, loosely geostrophic between 10° and 25°, and non-geostrophic (univariate) equatorward of 10°.

The correlations of each selected residual with itself and with all other selected residuals are computed and stored in a matrix. Using Bergman's symbols, the matrix elements are given by $\rho_{ij}^{kl} + n_{ij}^{kl}c_{ik}c_{jl}$, where ρ is the correlation of variables k and l's residuals at i and j, and η is the correlation of observation errors of the two residuals. For observation error correlation functions, Bergman's relations are used throughout. Observational errors of the same variable of different instruments are assumed uncorrelated, as are observational errors of different sensors within the same instrument package ($n_{ij}^{kl} = 0$ for $k \neq 1$). The observational error
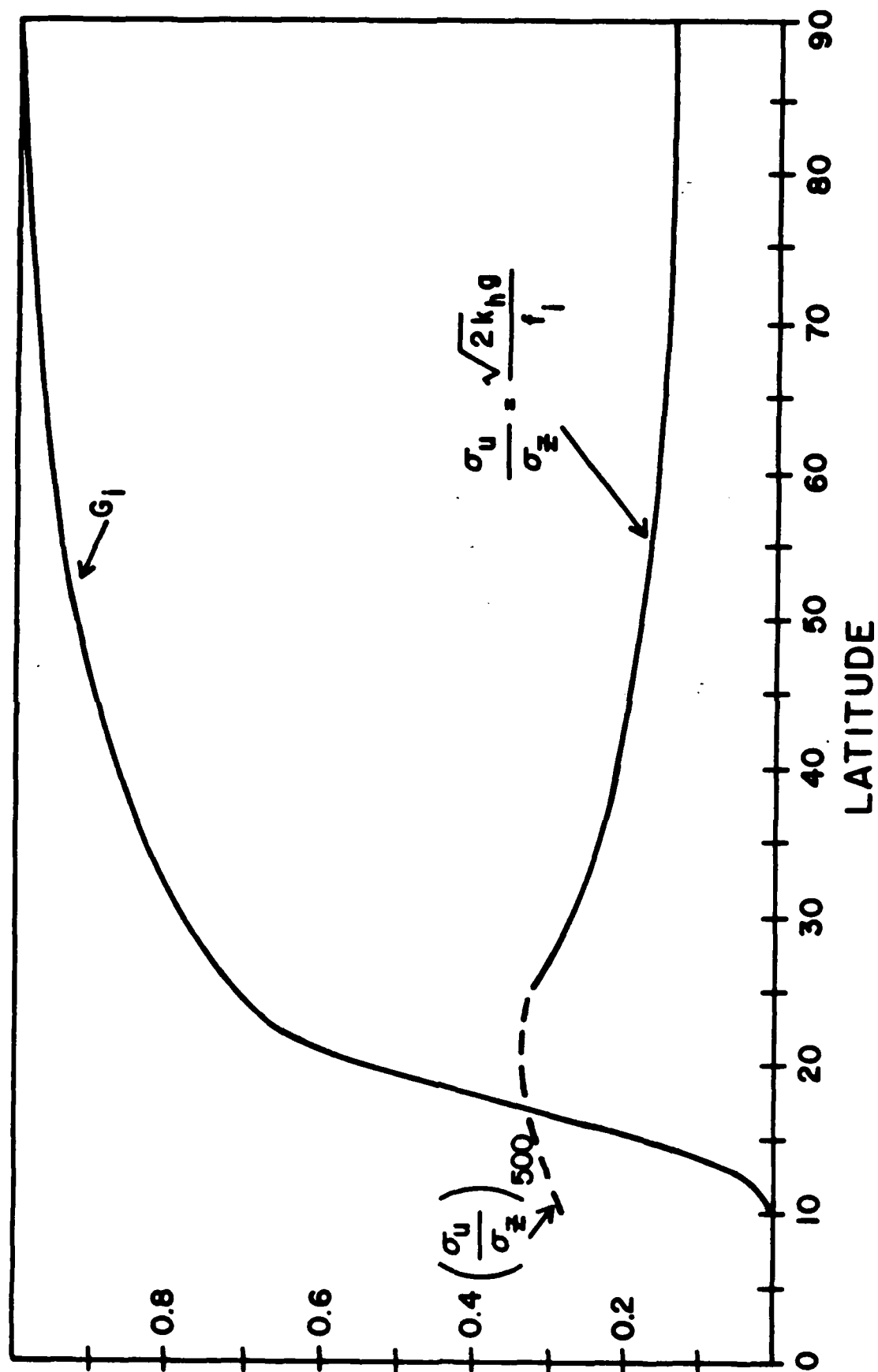
Fig. 2 Coefficient of Geostrophy and Ratio of Wind to Height Forecast Error Standard Deviation

16

correlation takes the general form $\eta^{kk} = \gamma_{ij}^{kk}\beta_{ij}^{kk}$, where γ and β represent the horizontal and vertical observational error correlations respectively. In general, they take the form of their counterparts μ and ν, that is,

$$\gamma_{ij}^{kk} = \exp(k_{h_o} s_{ij}^2) \tag{9}$$

$$\beta_{ij}^{kk} = \frac{1}{1 + k_{p_o} \ln^2(p_i/p_j)} . \tag{10}$$

Type 1 observations are assumed uncorrelated between instruments in the horizontal, but have a horizontal correlation of unity for the same observation and a vertical correlation for the same observation given by Eq. 10 using k_{p_o} = 8.3 for heights and 5.2 for winds (Morone, personal communication). Though winds measured by aircraft (Type 2) have several horizontally displaced observations taken by the same instrument, no measure of the horizontal spatial correlation was known at the time of this research, so they are assumed to be uncorrelated. Results from a recent NMC report (Morone, 1986) on the observational error correlations for aircraft winds could be incorporated into ASAPOI in the future to correct this shortcoming. Satellite height observational errors are assumed to be horizontally correlated using Eq. 9 and k_{h_o} = 1.13 x $10^{-11}m^{-2}$ and vertically correlated using the values in Table 3 (Morone, personal communication) where these values are vertically interpolated between values of X. Correlations for satellite cloud track wind observation errors were unknown, so they are assumed uncorrelated pending available information on this topic.

The right-hand side vectors, made up of the correlations ρ_{ig}^{kl} for analysis variable l = Z, u, and v in turn with all individual residuals,are used with the matrix to generate the solution vector elements a_{il} separately for l = Z, u, v. The Cholesky method (Stobie, 1984) is used to solve the three systems of linear equations. If a solution is not found for any reason, or if one of the normalized weights a_{il} from any of the three matrix problems is > 1.1, one residual from the most highly correlated pairs of residuals is removed, the matrix is reduced by one in rank and file, and the problem re-solved. At

17

Table 3. Vertical Error Correlation Function Values for Satellite T, z
(from Morone, personal communication)

X	$\nu^{tt} \eta_{ij}$
1	.99
2	.88
3	.61
4	.36
5	.18
6	.05
7	-.05
8	-.12
9	-.15
10	-.14
11	-.11
12	-.08
13	-.05
14	-.03
15	-.02
16	-.02
17	-.01
18	-.01
19	0.0
20	0.0

where $X = 20 \, [\ln (p_i/p_j)]^2 + 1$

p_i = pressure level of location i

p_j = pressure level of location j

this point, the actual weights a_{il} are computed from the normalized weights a_{il} for each of $l = Z$, u, v analysis variables using

$$a_{il} = \frac{\delta_{gl}}{\delta_{im}} a_{im}' \qquad (11)$$

where l represents the variable being corrected by variable type m. It should be noted again that δ_{im} is the forecast error standard deviation value for the variable m from the analysis level closest in pressure to the observation i, so that $\frac{\delta_{gl}}{\delta_{im}}$ may not always be unity for m = l. Also, in accordance with the use of G_i, G_g in the observation-analysis point correlation functions (G_i is used in a wind residual, height analysis point correlation, while G_g is used in a height residual, wind analysis point correlation), a_{il} is set to zero for l = Z when the wind observation is equatorward of 10°, and a_{il} is set to zero for l = u, v when the analysis point is equatorward of 10°. This insures that the analysis is strictly univariate in this region. Next, the normalized analysis error (square of the ratio of analysis error to forecast error standard deviation at the grid point, see Bergman's Eq. 2.13) is computed using the dot product of the normalized weight vector (for those elements that have non-zero values of actual weight a_{il} only) and its counterpart right-hand side correlation vector. Then the analysis error for the analyzed variable is obtained by multiplying the square root of the normalized analysis error by the forecast error standard deviation for that analysis variable at the grid point. This is done for Z, u, v, but only α_Z is carried into the next analysis. The correction for each of Z, u, v is calculated from the dot product of the vector of elements a_{il} and the vector of residuals, and its magnitude is checked against limits on the size of the corrections (250 m for Z, 25 m s^{-1} for u, v). If a computed correction exceeds its limit, the correction is set to zero and the normalized analysis error to unity.

Since temperature on the σ layers is the mass variable in the prognostic model, the height corrections on the layers have to be converted to temperature corrections on the layers. First, the OI analysis is used to compute a height correction for a σ layer value σ_u for a layer below $\sigma = 1.0$ whose $\Delta\sigma$ is equal to that of the lowest model layer. This is done

exactly the same way it is done for the computation of height corrections in all other layers, and is done to avoid extrapolation for the lowest $\Delta Z \rightarrow \Delta T$ conversion. Next, the layer height corrections ΔZ are converted to mean temperature corrections between the ML+1 (ML is the number of model layers) layer positions of height correction using

$$\overline{\Delta T}_k = -g(\Delta Z_{k+1} - \Delta Z_k)/[R \ln(\sigma_{k+1}/\sigma_k)] \quad . \tag{12}$$

The mean temperature corrections are assigned to the "layer-layer" pressures at the ML intermediate points between the ML+1 σ layer pressures. The σ values for these intermediate layer-layer positions are defined such that the natural logarithm of the layer-layer σ is the arithmetic average of the natural logarithm of the σ values of the surrounding layers. The layer-layer mean temperature corrections are then converted to σ layer temperature corrections using the Flattery algorithm (from NMC global spectral model preprocessing code) described in Appendix A. This algorithm has been used to convert interface temperatures to layer temperatures, and is presented this way in Appendix A. Application of this technique to the problem of converting layer-layer temperature corrections to layer temperature corrections is carried out analogously, and in our case K = ML+1, because of the use of a subsurface layer. By calculating a correction for the subsurface layer in the upper air OI analysis, the residuals are extrapolated to the pressure corresponding to σ_u using the vertical structure functions in the same way that extrapolations may occur at σ layers above the highest nearby residuals. A similar OI extrapolation to a layer above the highest σ layer was not done due to the sparsity of data at those altitudes. Uppermost layer extrapolation by the Flattery algorithm often produces unrealistic temperature corrections, so for these two reasons no temperature correction is made in the topmost layer.

Having earlier converted the wind residuals to Cartesian form for analysis points poleward of 70°, the computed wind component corrections based on these residuals are converted back to ϕ, λ form before being added to the first guess values to form the analyzed values. Temperature corrections from the Flattery routine are added to first guess temperatures at the analysis points, and analyzed T, u, v at all σ layers are written on an output file for the analysis point. This is done for all points on the 61 x 62 analysis grid.

20

C. The Humidity Analysis Program (MASAP)

Analysis of relative humidity is univariate and is performed in the lowest MLRH σ layers. The integer MLRH is the σ layer index for the lowest σ layer whose nominal pressure (i.e., assuming $p_* = 1000$ mb) is less than 300 mb. For the σ structure in this study, MLRH = 7. MASAP was designed to allow three options for processing of humidity information: (1) regular OI using measurements of humidity from rawinsondes and satellite soundings, (2) regular OI using rawinsonde and satellite humidity measurements, supplemented by relative humidity inferred from surface weather observations (SWO) and from AFGWC cloud analyses (3DN), and (3) replace first guess relative humidity with 3DN relative humidity at analysis points where the cloud analysis showed cloudiness, and regular OI using rawinsondes and satellite soundings elsewhere. The unchecked rawinsonde and satellite sounding relative humidity residuals were produced in ASAPOI. For option 2, MASAP performs similar processing to obtain SWO and 3DN residuals in turn. All four types are ordered from south to north with each observation containing as many as MLRH residuals.

After the full set of residuals containing all four types is formed, the gross and buddy checks are performed. Forecast error standard deviation values used for these checks (fixed in time) and to begin an assimilation sequence were derived from NMC statistics for March 1983 (Morone, personal communication) and are given in Table 4. As in the flagging procedure in the ASAPOI code, all observations are distributed into boxes of 10° latitude and of approximately equal area. Forecast error standard deviation (FESD) values are interpolated to pressures of residuals, and residuals exceeding three times the FESD are eliminated in the gross check. The buddy check criterion is exactly as it is in ASAPOI, where ρ_{ij}^{ZZ} is used as the correlation between two residuals, and the lower quality observation of a pair that fails it receives a toss flag. If the pair satisfies the criterion and $\rho_{ij}^{ZZ} \geq 0.75$, then if both observations in the pair are rawinsonde humidity residuals the higher quality observation receives two keep flags, and if both observations are not from rawinsondes the higher quality observation receives one keep flag. QCI values for the humidity buddy check are set as follows: vertically checked rawinsondes have QCI = 10, while SWO and 3DN humidities have QCI = 20. In this way, rawinsonde humidities cannot receive toss or

Table 4.   Forecast Error Standard Deviation for Relative Humidity
NMC Statistics, March 1983 (Morone, personal communication)

LATITUDE	90S-10S	10S-10N	10N-30N	30N-50N	50N-90N
Level (mb)	r (%)	r	r	r	r
1000	19	18	15	16	21
850	23	19	20	22	22
700	23	21	18	27	29
500	20	19	17	26	30
400	22	17	14	26	30
300	22	22	18	25	27

keep flags from other types, nor can they impose keep flags on other types.
Satellite sounding residuals can impose toss flags on and receive keep flags
from SWO and 3DN, while SWO and 3DN can receive keep flags from and impose
toss flags on other inferred residuals. After all toss and keep flags are
imposed, any residual having four or more keep flags is relieved of its toss
flags and is assured of being considered in the analysis. All residuals are
then subjected to the same type of iterative toss rejection procedure as
described for ASAPOI. When this is finished, observations with one or more
residuals remaining are assigned a number of points for each σ layer
residual: rawinsonde, four points each; satellite soundings, two points
each; SWO and 3DN, one point each.

In the OI analysis for each of the 61x62 analysis points, exactly the
same procedure is used to determine the NSNDS (presently 8) observations to
be used in the analysis of that point as in ASAPOI. However, the data types
in MASAP are considered in three groups: rawinsondes, satellite soundings,
and combined SWO and 3DN. Thus all satellite sounding humidities are only

considered if less than NSNDS rawinsonde observations had $\mu_{ig}^{zz} \geq 0.1$, and all
SWO and 3DN are considered only if fewer than NSNDS rawinsonde and satellite
observations have $\mu_{ig}^{zz} \geq 0.1$. Within each type, $\mu_{ig}^{zz} * $ PTS is used to
determine order of selection when more than NSNDS are found.

In preparation for the computation of the corrections in the univariate
OI, the forecast error standard deviation values to be used in the present
analysis are prepared. For the first analysis in a data assimilation
sequence, the values in Table 4 interpolated to the analysis point latitudes
and σ layer pressures are used. For subsequent analyses in that
assimilation sequence, the analysis errors from the previous analysis at
each of MLRH σ layers are read in, checked to be $\geq$ one times the forecast
error growth amount but $\leq$ 0.40, and augmented by a 6h prediction error
growth amount to form the FESD values for the analysis point. These growth
rates were estimated from early GSM runs and were set at .08, .08, .08, .08,
.09, .10, .12 respectively for the seven lowest NMC σ layers from bottom
to top. At this point, the relative humidity correction is set to zero and
the analysis error is equated to the just computed FESD for all MLRH layers
at the analysis point. These remain the values for σ layers where no
subsequent correction is computed for lack of nearby observations.

23

Processing for option 3 takes place at this point in the code, in
advance of the regular OI analysis. This section is avoided if option 1 or
2 is selected. The 850 mb–300 mb mandatory level values of $\cos[(\pi/100)*\%$
cloud amount] from the AFGWC cloud analysis at the analysis point are read
in. If there is at least one of the five mandatory levels with non-zero
cloud amount, the pressure level interfaces of the four computational cloud
layers (Tibaldi, 1982) given by

$p_1 = p_*$ (the first guess model surface pressure)

$p_2 = p_1 - 50$ mb

$p_3 = p_2 - (1/3)(p_2 - p_5)$　　　　　　　　　　　　(13)

$p_4 = p_3 - (1/3)(p_2 - p_5)$

$p_5 = 300$ mb

are determined for the analysis point. Then Tibaldi's Eq. 4, which in the
form used in MASAP is

$$r_k = M_L - A_L \cos[(\pi/100)*\% \text{ cloud amount}_k] ,\qquad (14)$$

is used to complete the inferred relative humidity for each of the five
mandatory levels indexed by k, where the values of A_L and M_L are
determined by which computational cloud layer L the kth pressure level
falls into, and the following table from Tibaldi:

L	Cloud Layer	M_L	A_L
1	PBL $(p_1 - p_2)$	.80	.20
2	LOW $(p_2 - p_3)$	.75	.15
3	MIDDLE $(p_3 - p_4)$	.60	.15
4	HIGH $(p_4 - p_5)$	.55	.10

Any time any of the levels falls below (greater in pressure than) p_1, it
is assigned the PBL value, and any time any level k lies above (less in
pressure than) p_5, it is assigned the HIGH value. Then all mandatory
levels that receive a value r_k in this way are used to assign the same
value as the σ layer 3DN by finding the mandatory level k that is closest
in pressure to the σ layer pressure. No value of r is assigned to a σ
layer whose pressure is closest to a mandatory level where r_k was not
calculated due to zero cloud amount. Then for each σ layer that receives
an r value in this way, a value of observation error standard deviation for
3DN (see Section IV) is interpolated to the σ pressure and assigned as the

"analysis error" for that analysis point σ layer position. This direct substitution of 3DN-inferred humidity for first guess humidity constitutes the "analysis" for each cloudy σ layer at the analysis point. Thus, if all MLRH σ layers receive values of r and analysis error in this manner, processing for that analysis point is finished. If any σ layer was not assigned an r by replacement, it is afforded an opportunity to receive a Δr correction through the conventional OI which follows. When at least one observation has a $\mu_{ig}^{zz} \geq 0.1$, with a maximum of NSNDS such observations, corrections can be computed for each of the σ layer positions at the analysis point. The horizontal and vertical structure functions μ_{ij}^{rr} and ν_{ij}^{rr} are identical in every way to those specified by Dey and Morone (1985). Thus,

$$\rho_{ij}^{rr} = \mu_{ij}^{rr} \, \nu_{ij}^{rr} \tag{15}$$

in which

$$\mu_{ij}^{rr} = \exp \{-k_h [P_{ij}^2/B_g + N_{ij}^2]\} \tag{16}$$

where P_{ij} and N_{ij}, the component of distance between locations i and j parallel and normal respectively to the analyzed wind vector at the analysis point and σ layer, are given by

$$P_{ij} = \frac{2}{m_i + m_j} \{\pm(y_i - y_j)[(u_g/|\tilde{V}_g|)\cos \lambda_g - (\pm v_g/|\tilde{V}_g|)\sin \lambda_g]$$

$$-(x_i - x_j)[(\pm v_g/|\tilde{V}_g|)\cos \lambda_g + (u_g/|\tilde{V}_g|)\sin \lambda_g]\}$$

$$\tag{17}$$

$$N_{ij} = \frac{2}{m_i + m_j} \{(x_i - x_j)[(u_g/|\tilde{V}_g|)\cos \lambda_g - (\pm v_g/|\tilde{V}_g|)\sin \lambda_g]$$

$$\pm(y_i - y_j)[\pm v_g/|\tilde{V}_g|)\cos \lambda_g + (u_g/|\tilde{V}_g|)\sin \lambda_g]\}$$

for $|\phi_g| \geq 70°$ where m_i, m_j are the map factors, x_i, x_j, y_i, y_j are the x, y locations with respect to the poles on a Cartesian polar stereographic projection, u_g, v_g, $|\tilde{V}_g|$ are the components and speed of the analyzed wind at the analysis point g, $k_h = 2 \times 10^{-12} m^{-2}$, $B_g = 1 + 0.004(u_g^2 + v_g^2)$, and λ_g is the longitude of the analysis point. The top and bottom signs apply to the Northern and Southern Hemispheres respectively. Then

$$P_{ij} = (\lambda_i - \lambda_j)\cos[(\phi_i + \phi_j)/2](u_g/|\tilde{V}_g|) + (\phi_i + \phi_j)(v_g/|\tilde{V}_g|)$$

(18)

$$N_{ij} = -(\lambda_i - \lambda_j)\cos[(\phi_i + \phi_j)/2](v_g/|\tilde{V}_g|) + (\phi_i + \phi_j)(u_g/|\tilde{V}_g|)$$

for $|\phi_g| < 70°$. Also,

$$v_{ij}^{rr} = [1 + (k_p + C)\ln^2(p_i/p_j)]^{-1}$$ (19)

where $k_p = 5$ and

$$C = \begin{cases} -75 \frac{\partial T}{\partial p} \; ; & \frac{\partial T}{\partial p} \leq 0 \; (°K \; mb^1) \\ 0 \; ; & \frac{\partial T}{\partial p} > 0 \end{cases}$$

(20)

$$\frac{\partial T}{\partial p} = \frac{1}{2}[(T_{k+1} - T_k)/(p_{k+1} - p_k) + (T_k - T_{k-1})/(p_k - p_{k-1})]; \; k=2, \; MLRH-1,$$

$$= (T_2 - T_1)/(p_2 - p_1); \; k = 1$$ (21)

$$= (T_k - T_{k-1})/(p_k - p_{k-1}); \; k = MLRH$$

where T_k is analyzed σ layer temperature. The correlation ρ_{ig}^{rr} of each residual of relative humidity at observation point i with the analysis σ level g are calculated using the above equations. Then the quantities $\rho_{ig}^{rr}/(1+\epsilon_i^2)$, where ϵ_i is the normalized observation error, are sorted by size and the NLRHS (presently 10) individual residuals with the largest values are selected for the correction computation. Here, observation error standard deviation [OESD] is interpolated from mandatory levels to observation pressure,

but FESD used is analysis level value. Then the correlation matrix elements $\rho_{ij}^{rr} + \eta_{ij}^{rr} c_i c_j$ are computed for all pairs of the NLRHS (or fewer) residuals, and the matrix equation involving these elements and the right-hand side correlations $\rho_{ij}^{rr}/(1+c_i^2)$ is solved for the weights a_i. The Cholesky scheme is also used here, with the same provision made in the case of a singular matrix as in ASAPOI. Then the normalized analysis error is computed using the weights and the right-hand side correlations, and the correction is computed using the weights and the residuals. Note that since local homogeneity is assumed in FESD, $a'_i = a_i$ since the ratio of observation site FESD to analysis point FESD is unity. Computed corrections must not exceed 0.40, and the resulting analyzed value is adjusted (if necessary) to lie between 0.1 and 1. The analysis error passed to the next analysis is the product of the FESD for the analysis point and the square root of the normalized analysis error. Finally, analyzed r is converted to q using Eqs. 1-4 in reverse form using analyzed T and first guess σ layer pressures.

Observation error correlations η_{ij}^{rr} in the humidity analysis are again the product of horizontal (isobaric) and vertical error correlations. First, it is assumed that observation errors from two different types of observations (here, inferred relative humidities are included as "observations") are uncorrelated. It is further assumed that all individual rawinsonde observations are uncorrelated. No attempt was made to compute observation error correlations for satellite observations since their OESD values computed from the FGGE II-B data set used were found to be excessive. Values for the horizontal and vertical observation error correlations for SWO and 3DM are given in Tables 5-8, having been calculated following the procedure described in Section IV. A SWO or 3DM residual pair is assigned a horizontal correlation value according to which 50 km separation distance category it falls into and a vertical correlation according to the closest mandatory pressure level to each residual in the pair.

D. The Post-Analysis Program (POASAP)

POASAP converts the 61x62 analysis fields of T, u, v, q at their respective σ layers into 30 wave rhomboidal spectral coefficients of temperature, vorticity, divergence, and specific humidity. This is done

Table 5. Horizontal Observation Error Correlations for SWO Inferred R.H.

Distance (km)	1000-850	700-500	400-300
0-50*	1.0	1.0	1.0
50-100	.2039	.7030	.9033
100-150	.3755	.5835	.7196
150-200	.4041	.5828	.6305
200-250	.3899	.5363	.6134
250-300	.3620	.5078	.5683
300-350	.3035	.4621	.5118
350-400	.3122	.4515	.4609
400-450	.2912	.4461	.4887
450-500	.2698	.3613	.4395
500-550	.2486	.3596	.4113
550-600	.2334	.3235	.3223
600-650	.2099	.2879	.3558
650-700	.1702	.2714	.3600
700-750	.1859	.2530	.3556
750-800	.1675	.2319	.2789
800-850	.1380	.2053	.2499
850-900	.1421	.2451	.3172
900-950	.1139	.1764	.2583
950-1000	.1217	.1984	.2751
1000-1050	0	.1629	.2422
1050-1100		.1209	.2407
1100-1150		.1432	.2301
1150-1200		.1440	.2143
1200-1250		.1357	.1879
1250-1300		.1284	.2162
1300-1350		.1004	.1734
1350-1400		.1247	.2075
1400-1450		0	.1588
1450-1500			.1792
1500-1550			.2117
1550-1600			.1233
1600-1650			.1369
1650-1700			.1059
1700-1750			.1490

* values in this category were reset to 0.9 for use in relative
  humidity analysis

Table 6. Vertical Observation Error Correlations for SWO Inferred R.H.

$P_i - P_j$	ν_{ij}^{rr}
1000–850	.2867
1000–700	.1435
1000–500	.0852
1000–400	.0843
1000–300	.0950
850–700	.4727
850–500	.3575
850–400	.3621
850–300	.3496
700–500	.5434
700–400	.5157
700–300	.5084
500–400	.8137
500–300	.7767
400–300	.8895

Table 7. Horizontal Observation Error Correlations for 3DN Inferred R.H.

Distance (km)	850	700-500	400-300
0-50*	1.0	1.0	1.0
50-100	.2795	.4967	.5832
100-150	.2121	.4715	.5074
150-200	.3004	.4303	.4917
200-250	.2534	.3941	.4416
250-300	.2604	.3414	.4924
300-350	.2282	.3197	.4055
350-400	.1951	.2752	.3822
400-450	.1928	.2732	.4153
450-500	.1701	.2174	.3814
500-550	.1720	.1892	.3167
550-600	.1586	.1801	.3160
600-650	.0880	.1663	.2908
650-700	.1185	.1152	.2749
700-750	.1167	.1428	.3191
750-800	0	.1138	.2601
800-850		0	.2604
850-900			.3270
900-950			.2471
950-1000			.2744
1000-1050			.2712
1050-1100			.2378
1100-1150			.2270
1150-1200			.2277
1200-1250			.2499
1250-1300			.2043
1300-1350			.2333
1350-1400			.2453
1400-1450			.2431
1450-1500			.2303
1500-1550 (1750-1800)			.2112 (.1665)
1550-1600 (1800-1850)			.2444 (.2541)
1600-1650 (1850-1900)			.2091 (.2109)
1650-1700 (1900-1950)			.2405 (.2126)
1700-1750 (1950-2000)			.2199 (.1559)

* values in this category were reset to 0.9 for use in relative humidity analysis

30

Table 8. Vertical Observation Error Correlations for SWO Inferred R.H.

$P_i - P_j$	v_{ij}^{rr}
850–700	.3833
850–500	.1609
850–400	.1498
850–300	.1346
700–500	.4638
700–400	.3892
700–300	.3863
500–400	.7131
500–300	.6437
400–300	.8026

using a Fast Fourier transform on the 61 grid values on each of the 62
Gaussian latitudes, then a Gaussian quadrature integration for each Fourier
component over the latitudes using the appropriate Gaussian weights. The
analysis errors α_z, α_r on the 61x62 grid are similarly transformed
to spectral form. Finally, the 61x62 first guess values of surface pressure
are updated at each analysis point by extrapolating analyzed heights on the
upper interfaces of the lowest three σ layers (from analyzed layer
temperatures) down to the terrain height Z_*. The method used is described
in Appendix B. Then these updated surface pressures are converted to
spectral form (ln p) and included in the set of spectral coefficients passed
on to the NMI.

III. METHODS FOR OBTAINING REPRESENTATIONS OF OBSERVATIONS ON
     SIGMA LAYERS/LEVELS

Much discussion among analysts of global observations has focused on
the relative advantages and disadvantages of performing the analysis on
model σ layers vs. isobaric levels. Certainly, the former method has the
advantage of avoiding the necessity of vertically interpolating first guess
(model forecast) fields to isobaric levels, and then interpolating the
computed corrections to the σ layers. It does require an interpolation of
observational data to the model σ layers (or for Z, levels). The
motivating factors for using this approach were (1) to avoid the smoothing
of the first guess fields and computed corrections resulting from the
vertical interpolation, and (2) to make use of all observations (including
significant level data) in a sounding to minimize the error in interpolating
observations to σ layers/levels. The following paragraphs describe the
steps taken in performing these interpolations.

A. Type 1 Observations (Rawinsondes, Pibals, Dropsondes, TWOS Navaids)

Once the values for p, Z, T, DPD, $|\tilde{V}|$, and θ (wind direction) are
read in for FGGE II-B quality levels 0 or 1 (unchecked, or found valid
vertical consistency check) for all levels in a sounding, the observation is
checked to be within three hours of the analysis time and is assigned a
buddy check box. If the observation is found to lie within 0.01 degrees
latitude and longitude of a previously accepted observation, the observation
with the higher value of data source index (DSI) is rejected. DSI values
for various instruments in Type 1 are: 11, rawinsonde; 12, pibal; 14, TWOS
(tropical wind observing ship) Navaid; 15, aircraft dropwinsonde. Dew point

32

depression (DPD) given in the observation data is converted to specific humidity using the expressions

$$TD = T-DPD$$
$$e = 6.11 \cdot \exp(19.9274-5443.3619/TD) \qquad (22)$$
$$w = .622 \cdot e/(p-e)$$
$$q = w/(1+w).$$

Wind components u, v are computed from $|\tilde{V}|$, θ using

$$u = -|\tilde{V}|\sin \theta \qquad (23)$$

$$v = -|\tilde{V}|\cos \theta .$$

After checking for duplicate levels or levels out of order (according to decreasing pressure), the bilinear interpolation of first guess T, u, v, r, and p_* to the observation site is performed, σ layer (p) and σ level $(\hat{p})$ pressures are computed and σ level heights are derived from Z_* and the bilinearly interpolated T on σ layers using Eq. 5. If more than one level of sounding data exists in the observations, the algorithm PTOSIG is invoked. The method of computation of σ level Z, and σ layer u, v, T, and q is described in Appendix C. For Z, the observation levels immediately surrounding each σ level having valid values of both T and Z are identified, and if they are within 300 mb of each other they are used to compute the σ level Z. Layer T is then computed from each pair of σ level Z's except when one or both is missing: then layer T is missing. Then the σ level Z values are recomputed by means of Eq. 5 for comparison with their first guess counterparts using Z_* and these layer T estimates. If a σ layer T is missing in the computation of level Z, the Z value at the top of that level is declared missing and the first guess Z at that level is used as the new anchor in the computations for Z above. The quality control value assigned to each level Z is the higher (poorer in quality) of the two values for the original level Z's that led to the layer T, each of which in turn was the highest of the four pieces of information (Z_1, Z_2, T_1, T_2) used from the sounding to compute the original level Z value. The 300 mb difference limit is also used for observation levels surrounding σ layers in the vertical interpolation of u, v, and ln q. Specific humidity

33

interpolation in ln q vs. ln p was performed to avoid the bias introduced in a q vs. ln p interpolation (Mitchell, 1985). Vertically interpolated q and T values on σ layers are used to compute r on σ layers using Eqs. 1-4. Observation-minus-first guess residuals for Z (levels), and u, v, r (layers, with just the lowest MLRH layers for r) are computed to finish the processing.

B. Type 2 Observations (Aircraft Winds)

Aircraft observations consist of single point observations of temperature and wind at a known flight altitude. In the FGGE II-B data set, several wind observations may be included in the report, each with its own latitude and longitude location. It was assumed that the altitude applies to all wind observations in the report.

The aircraft reports, although allowing space for it in the record, do not contain a pressure value at flight altitude. Because pressure is the vertical coordinate in the system, this makes it difficult to locate where the observation should be placed with respect to the model atmosphere. NMC (Morone, personal communication) has provided formulas to assign a pressure to an aircraft flight altitude, as follows:

$$p(Z) = 226.3 \exp[1.576106 \times 10^{-4} (11000-Z)]; \quad Z > 11 \text{ km}$$

$$\tag{24}$$

$$p(Z) = 1013.5 \ [(288-0.0065Z)/288]^{5.256}; \quad Z \leq 11 \text{ km}.$$

These formulas are apparently based on standard atmosphere formulations. A pressure is assigned to the flight altitude Z in the following way. First, the heights of the model levels surrounding the observation Z are obtained, and the one to which Z is closest is identified (call this Z_{σ_k}). Then pressures are obtained for both Z and Z_{σ_k} using the same formula above (the larger of Z and Z_{σ_k} is compared with 11,000 m and the appropriate equation is used for both). Then $p(Z_{\sigma_k})$ is compared with the model level pressure $p_{\sigma_k}(Z_{\sigma_k})$, and the difference is applied as a correction to $p(Z)$.

At this point, the model layer pressures surrounding $p(Z)$ are identified, and the first guess temperatures and winds at these layers are linearly interpolated in ln p to $p(Z)$. The observation-minus-first guess

34

residuals individually for temperature and wind components are calculated at this level, and these residuals are added to the model layer first guess values whose pressure is closest to p(Z). The respective sums constitute an estimate of the observation value in that model layer for temperature and winds. A value for height at the top of that layer is calculated from first guess height at the bottom of that layer and this temperature using Eq. 5. However, the values of σ level heights derived from aircraft observations are not currently used in the ASAP analysis. Any other wind observations given in the same report are processed as above using the same flight altitude.

C. Type 4 Observations (Satellite Soundings)

Satellite sounding data in the FGGE II-B data set come in four different forms:

ITYP=1: layer thickness between reference pressure level and standard pressure level

ITYP=2: layer precipitable water between a reference pressure level and a standard pressure level

ITYP=3: layer mean temperature between two non-standard pressure surfaces

ITYP=4: layer precipitable water between two non-standard pressure surfaces.

Satellite soundings over land are not used in the analysis. The discrimination between land and ocean soundings is made by bilinear interpolation of the FGGE Fixed Field 2.5° x 2.5° terrain field to the latitude-longitude position of the satellite sounding. If the resulting height value is greater than 0.5 meters, that observation is excluded from the analysis. After the ±3h time check and assignment to a buddy check box, the observation location is checked against previously accepted observations (accepted Type 1 and Type 4 obs before the present one). If it is located within 0.01 degree latitude and longitude of an accepted observation, it is rejected. The quality control indicators for Type 4 data are set according to two criteria: quality control not made (QCI=1), and report found correct during quality control (QCI=0). Other levels of quality control are included in the data set, but any observations not included in one of these two categories are rejected. Bilinear interpolation of first guess values to the observation site occurs next. Then the report is checked to see if

it contains ITYP=1 or ITYP=3 for thickness information (not both), and
ITYP=2 or ITYP=4 for moisture information (not both). The following
paragraphs describe the processing of the four types of data.

For ITYP=1 and ITYP=3, the following procedure is used to obtain
representations of observed geopotential height on σ level surfaces.
First, determine the observation layer mean temperature. For ITYP=3, this
is given directly. For ITYP=1, the observation layer mean temperature is
given by

$$\bar{T}_k = g\Delta Z/[R \ln (p_k/p_{k+1})]; \quad k = 1, K_s-1 \qquad (25)$$

where ΔZ is the (positive) thickness in geopotential meters between the
lower (in altitude) pressure surface p_k and the upper pressure surface
p_{k+1}. Then for both ITYP=1 and ITYP=3, the next step is to use the
Flattery algorithm to estimate the satellite level temperatures $\hat{T}_\ell$ at all K_s
layer interfaces from the layer temperatures $\bar{T}_k$. One of the resulting $\hat{T}_\ell$'s
near the middle of the sounding (usually 400 mb) is chosen as an anchor
(T_{ANCH}) to recalculate the other $\hat{T}_\ell$'s. This is done because it was found
that the errors introduced by the Flattery algorithm are the smallest in the
middle of a sounding, with larger biases at top and bottom. Then the other level
interface temperatures $\hat{T}_\ell$ are computed from $\hat{T}_{ANCH}$ and the $\bar{T}_k$ using the method
described in Appendix D. Once the $\hat{T}_k$ are known for all k, they are used to
interpolate linearly in ln p to obtain the σ layer temperatures T_{σ_k}:

$$T_{\sigma_k} = \frac{1}{2} (\hat{T}_\ell+\hat{T}_u)+\{(\hat{T}_\ell-\hat{T}_u)/[\ln(p_\ell/p_u)]\}\{\ln p_{\sigma_k} -\frac{1}{2}[\ln(p_\ell p_u)]\} \qquad (26)$$

where $\hat{T}_\ell$, $\hat{T}_u$ are the derived satellite level temperatures at levels p_ℓ, p_u
immediately below and above the σ layer pressure p_{σ_k}. Then Eq. 5 is used
to obtain the estimates of σ level Z from the T_{σ_k} using Z_* [or, at top of
any layer where T_{σ_k} may be missing, $Z_{f.g.}(\sigma_k)$] as an anchor.

36

When this method was being developed it was tested along with the straight Flattery method using a single rawinsonde sounding so that temperature could be used as an input and output heights could be verified against rawinsonde height. This test is described in Appendix D. The method was also used to compute RMS differences and biases in height against collocated rawinsondes for the periods 2/3/79 12Z – 2/22/79 00Z and 6/13/79 12Z – 7/1/79 06Z using FGGE II-B data for both. In this data set, the levels typically included in the satellite layer mean temperature soundings were 1000, 850, 700, 500, 400, 300, 200, 100, 70, 50, 30, 10, 5, 2, 0.4 mb. Using the lowest available mandatory level rawinsonde height as an anchor, the satellite layer temperatures themselves were used to estimate values of satellite height at all mandatory levels above the anchor level up to 50 mb. The RMS differences and bias between these and mandatory level rawinsonde heights (except 1000 mb, the usual anchor level, and 250 and 150 mb) are given in the left side of Table 9. Values on the right side result from using reported satellite layer temperatures to get level temperatures according to the method in Appendix D. Next, the values are linearly interpolated to the mandatory layer pressures where the same relationship between σ level and layer pressures is used to define mandatory layer pressures in terms of mandatory level pressures. Finally, Eq. 5 and the anchor rawinsonde height are used to estimate height on upper mandatory levels. The difference between the two sets is due to the synthesis of the layer temperatures, which is done in obtaining σ level heights from satellite layer temperatures in the analysis. The RMS differences for the synthesized results were used to estimate observation error standard deviation values for the satellite heights. According to

Bergman (1978), if the RMS differences $[\overline{(\hat{F}_a - \hat{F}_b)^2}]^{\frac{1}{2}}$ between observation sets $\hat{F}_a$ and $\hat{F}_b$ (with uncorrelated observation errors) are known, and estimates of OESD $= (\overline{e_a^2})^{\frac{1}{2}}$ for type a are known, the same for type b can be evaluated from

$$(\overline{e_b^2})^{\frac{1}{2}} = \sqrt{\{[\overline{(\hat{F}_a - \hat{F}_b)^2}]^{\frac{1}{2}}\}^2 - [(\overline{e_a^2})^{\frac{1}{2}}]^2} \quad . \qquad (27)$$

Table 9. Geopotential Height RMS and Bias for All Collocated
Satellite Soundings and Rawinsonde Soundings

Using Reported Satellite Layer T				Using Synthesized Satellite Layer T			
Level (mb)	RMS (m)	Bias(m)	#OBS	Level (mb)	RMS (m)	Bias(m)	#OBS
				02/03/79 12Z – 02/22/79 00Z			
850	27.13	-1.55	293	850	24.99	-2.91	399
700	33.75	- .21	533	700	36.23	-1.11	481
500	48.72	5.70	561	500	50.73	5.63	498
400	68.55	10.30	568	400	71.64	10.83	501
300	95.26	15.72	559	300	99.66	16.96	492
250	–	–	–	250	98.42	25.52	475
200	108.68	33.82	521	200	102.15	31.00	460
150	–	–	–	150	96.43	24.80	455
100	87.61	38.11	490	100	85.56	34.89	433
70	81.25	36.70	411	70	79.31	33.22	355
50	91.19	36.33	403	50	90.16	31.34	351
				06/13/79 12Z – 07/01/79 06Z			
850	30.55	-2.61	328	850	26.62	-3.36	502
700	31.13	.99	699	700	34.02	- .13	645
500	30.95	.81	746	500	33.39	.26	678
400	52.97	1.58	748	400	55.64	1.07	679
300	68.14	1.65	726	300	71.19	1.72	660
250	–	–	–	250	70.22	2.41	652
200	61.83	7.27	692	200	63.68	3.94	632
150	–	–	–	150	58.28	-4.36	620
100	66.47	6.42	657	100	67.07	.50	597
70	69.30	2.15	585	70	73.51	-3.03	490
50	82.77	3.19	565	50	87.80	-1.08	466

Values from Dey and Morone (1985) of $(\overline{e_a^2})^{\frac{1}{2}}$ are used for rawinsonde heights, and RMS values from the right side of Table 9 are used to produce estimates of OESD for satellite synthesized heights in Table 10.

For ITYP=2 and ITYP=4, the following procedure is used to obtain representations of observed specific humidity on σ layers. First, determine the layer precipitable water for each observation layer. For ITYP=4, this is given directly. For ITYP=2, we use the integral nature of the definition of layer precipitable water,

$$W = \frac{1}{g\rho_o} \int_{P_u}^{P_\ell} q\,dp, \qquad (28)$$

where ρ_o is the density of water and p_ℓ, p_u represent the lower and upper interface pressures for the layer over which q is integrated to compute the layer precipitable water. The integral over the entire series of layers is equal to the sum of the individual layer precipitable water values. Thus we may assume that the W for a particular layer is the difference between the W between the top of that layer and the reference level (1000 mb) and the W between the bottom of that layer and the reference level. Now knowing the W value for each layer included in the report, Eq. 28 may be solved approximately for the value of q at the bottom of each layer when an anchor value at the top of the uppermost layer is specified. In the ASAPOI module for satellite data processing, a value for $q(p_u)$ at the top of the highest layer in a given observation is obtained by linear interpolation in ln p on the first guess q values to p_u. Since this work was accomplished before it was discovered that ln q varies more linearly with ln p than does q (see Mitchell, 1985), the specific humidity and not its natural logarithm was used as the dependent variable in the interpolation relationship. As satellite moisture was not included in the present assimilation experiments, the bias was not introduced into the analysis; however, future processing of satellite data will involve the assumption of linearity of ln q in ln p. To obtain the value of $q(p_\ell)$ at the bottom of each successive layer, we assume linearity of q in ln p between p_ℓ and p_u:

39

Table 10. Computation of Observation Error Standard Deviation for Satellite Height*

Level	$(e_r^2)^{\frac{1}{2}}$(NMC)	$[\overline{(\hat{F}_r-\hat{F}_s)^2}]^{\frac{1}{2}}$(FEB)	$(\overline{e_s^2})^{\frac{1}{2}}$(FEB)	$[\overline{(\hat{F}_r-\hat{F}_s)^2}]^{\frac{1}{2}}$(JUN)	$(\overline{e_s^2})^{\frac{1}{2}}$(JUN)
1000	7.0	(12)	9.75	(18)	16.58
850	8.0	24.99	23.67	26.62	25.39
700	8.6	36.23	35.19	34.02	32.92
500	12.1	50.73	49.27	33.39	31.12
400	14.9	71.64	70.07	55.64	53.61
300	18.8	99.66	97.87	71.19	68.66
250	25.4	98.42	95.09	70.22	65.47
200	27.7	102.15	98.32	63.68	57.34
150	32.4	96.43	90.82	58.28	48.44
100	39.4	85.56	75.95	67.07	54.28
70	50.3	79.31	61.32	73.51	53.61
50	59.3	90.16	67.91	87.80	64.75

* Here, subscripts r = radiosonde, s = satellite

40

$$q(p) = \frac{q(p_\ell) + q(p_u)}{2} + \frac{q(p_\ell) - q(p_u)}{\ln p_\ell - \ln p_u} [\ln p - \frac{\ln p_\ell + \ln p_u}{2}]. \quad (29)$$

If we substitute this expression into the integral definition of W above, we obtain the following expression for $q(p_\ell)$, the specific humidity at the bottom of the layer:

$$q(p_\ell) = \frac{Wg\rho_0 - q(p_u)[\frac{1}{2}(p_\ell - p_u) + A]}{\frac{1}{2}(p_\ell - p_u) - A} \quad (30)$$

where

$$A(p_\ell, p_u) = \frac{p_\ell - p_u}{\ln p_\ell - \ln p_u} - \frac{1}{2}(p_\ell + p_u).$$

Using the layer precipitable water W (in 10^{-1} m) and the top and bottom pressures of the layer (in mb), and using $g = 9.8$ ms^{-2} and $\rho_0 = 1g$ cm^{-3}, $q(p_\ell)$ will have units of grams of water vapor per gram of air. If in any lower layer the observed W value is not available, the computed q value for the bottom of that layer is not available. A first guess q value is found for that pressure level using surrounding $q_{f.g.}$ values and a linear interpolation in ln p to provide a new anchor value for the computation of q from W in layers below.

In the ASAPOI code, values of q at the bottom of each report layer are linearly interpolated to the σ layer pressures. Then they are converted to r using Eqs. 1-4 and the satellite σ layer temperatures computed for the same sounding. First guess σ level height and σ layer relative humidity are subtracted from their computed satellite counterparts to form the residuals used in the OI analysis.

A collocation study between satellite soundings and rawinsondes was conducted to determine values of OESD for relative humidity values obtained using the method described above. FGGE II-B observations for the same two periods used in the satellite-rawinsonde height study were included in the study, with the typical soundings including values of W for the 1000-700, 700-500, and 500-300 mb layers. The rawinsonde value of q at the top of the

41

uppermost satellite observation reporting layer (usually 500-300 mb) was used to anchor the q calculation. In this way, a satellite observation value for q was derived for 500 mb and 700 mb. Satellite sounding temperature values reported with the layer precipitable water values were used to convert q to relative humidity. At the time of this processing, the reported satellite layer temperatures were interpolated from mean layer pressures to the 500, 700, and 1000 mb levels to perform this conversion. Since no extrapolation was allowed, no temperature value for 1000 mb was computed, and thus no value of satellite relative humidity was computed at 1000 mb. RMS differences for 700 mb and 500 mb for the February period were calculated to be 34 percent and 53 percent in relative humidity respectively, while the same calculations for the June period resulted in values of 22 percent and 25 percent respectively. As the February values were thought to be excessive, scatter plots of collocated satellite r vs. rawinsonde r were constructed to determine if a correction relationship between the two could be derived empirically. Because of the significant scatter observed, no attempt was made to try to develop a correction function for satellite r. Comparisons of rawinsonde r converted to W with satellite W were just as disappointing, with RMS differences in W ranging from 50 to 70 percent of the averaged rawinsonde values. It was decided not to use the Final FGGE II-B satellite W observations in the assimilation experiments described in this report because of their large, rather random differences with rawinsonde values. It is recommended that the satellite-rawinsonde humidity collocation study be repeated at some later date using the FGGE II-B reprocessed data set, because of the encouraging results obtained in such a study conducted recently at ECMWF (Lönnberg, private communication).

D. Type 6 Observations (Single-Level Satellite Cloud Motion Winds)

Satellite temperature and cloud motion wind data are single level observations like the aircraft data. In this case, the pressure of the observation $p(Z)$ is reported instead of the altitude. Therefore, the surrounding σ layer pressures can be found immediately, and as in the case of the aircraft data, first guess temperature and wind components are linearly interpolated in ln p to $p(Z)$. Observation-minus-first guess residuals are calculated at this level, and these residuals are added to the first guess values whose pressure is closest to $p(Z)$ to form the estimate of

42

the observation values at this σ layer pressure. First guess height at the bottom of the layer is used with the computed layer temperature to estimate height at the top of the layer hydrostatically; however, these estimated heights were not used in the present assimilation study. First guess height and wind component values are subtracted from their estimated observation counterpart to form the residuals.

IV. METHODS FOR OBTAINING REPRESENTATIONS OF INFERRED HUMIDITIES ON SIGMA LAYERS

A. Surface Weather Observations

An algorithm described by Tibaldi (1982), modified slightly from a method first described by Chu and Parrish (1977), was used to estimate upper air relative humidity from surface weather observations (SWO). The SWO is used to obtain an estimate of the average relative humidity in four layers approximating the planetary boundary layer and the layers used for the classification of low, medium, and high clouds (see Eqs. 13, 14). Once this is done, the humidity at any pressure level is set equal to the layer average humidity of whichever of these four computational layers the pressure level falls into. This is true both for the estimation of relative humidity at σ layers for the analysis and for the values at mandatory pressure levels in the collocation study to be described later. The following paragraphs describe how the four layer average relative humidities were deduced from the FGGE II-B surface weather observations.

After checking each SWO to be within three hours of the analysis time (the SWO with the time closest to the analysis time is used), and making sure that it is not collocated with a previously accepted humidity observation (rawinsonde or satellite sounding), the observation is checked to see that both the pressure/height entry and temperature entry in the report have valid values. The pressure/height variable pZ can be given in the FGGE II-B data set in the form of sea level pressure, station pressure, pressure at altitudes ranging from 1000-4000 m, or geopotential height at 850, 700, or 500 mb. All observations which have pZ in any form other than station pressure are converted to station pressure using the given values P_{ob}, Z_{ob} from the pZ variable and the inverse of the NMC "Shuell" method

43

that is normally used to reduce station pressure to sea level pressure. It is then this given or computed value of station pressure that forms the basis for the definition of the four computational layers whose bounding pressures are computed from Eq. 13.

For the boundary layer, 60 percent relative humidity is assigned as the estimate from clouds (RHPBL) if either there were no low clouds (C_L) present, or low clouds had a base height greater than or equal to 600m. If low clouds were present, the value of RHPBL was set using the expression $RHPBL=M_{PBL}-A_{PBL}\cos[(\pi/8)OKTAS_{PBL}]$ in which $OKTAS_{PBL}$ had one of two values: (1) if in the significant cloud record, significant cloud types 6 through 9 are present (cloud types Sc, St, Cu, Cb), the $OKTAS_{PBL}$ is set to the significant cloud amount for that cloud type, or (2) if significant cloud data are not available, but amount of low or middle clouds (N_h) is nonzero and reported low cloud type is identified and the cloud base height is less than or equal to 600m, the amount of low or middle clouds in the report is used for $OKTAS_{PBL}$. Then the simple average of RHPBL, RHTD (relative humidity from observed temperature and dew point temperature), and RHWW (relative humidity estimated from present weather table) is used to estimate relative humidity for the planetary boundary layer. In this case, QCI=0 is set for the PBL. If one of the three is missing, the average of the other two is used and QCI=1.

A default value of 60 percent relative humidity is also used for RHLC for the low cloud layer if no clouds are present. If low clouds are present, the value of RHLC was set using $RHLC=M_{LC}-A_{LC}\cos[(\pi/8)OKTAS_{LC}]$ where $OKTAS_{LC}$ is set in the same way as for $OKTAS_{PBL}$ except the condition for cloud base height is removed in circumstance (2) above. Then the simple average of RHLC and RHWW is used to give the relative humidity estimate for the low cloud layer, and QCI=0. If RHWW is missing, RHLC is used and QCI=1.

A value of 45 percent is assigned for the estimate of relative humidity in the middle layer if no middle layer (C_M) clouds (types Ac, As, Nc) are present. If such clouds are present, the significant cloud amount is assigned to $OKTAS_{MC}$ if the middle layer significant cloud information is available, and if not the amount of low or middle clouds (N_h) is used for $OKTAS_{MC}$. In either case, the estimate of relative humidity in the middle layer is obtained from $M_{MC}-A_{MC}\cos[(\pi/8)OKTAS_{MC}]$, and QCI=0.

A value of 45 percent is assigned for the estimate of relative humidity in the high layer if no high layer (C_H) clouds (types Ci, Cc, Cs) are present. If such clouds are present, the significant cloud amount is assigned to $OKTAS_{HC}$ if the high layer significant cloud information is available. If not, and if the total cloud amount is nonzero and there are no low or middle clouds (N_h) present, the total cloud amount (N) is assigned to $OKTAS_{HC}$. If the latter is not true, high layer relative humidity is assigned as missing. The value of $OKTAS_{HC}$ is then used in $M_{HC} - A_{HC} \cos[(\pi/8) OKTAS_{HC}]$ to estimate relative humidity for the high layer, and QCI=0.

Once the pressure level boundaries and the mean layer relative humidity for the four computational layers have been computed for each SWO, the σ layer relative humidities are assigned according to which computational layer each σ layer pressure at the observation site falls into. If any σ layer pressure is $\leq$ 50 mb greater than p (station pressure), it is assigned the lowest computational layer relative humidity. Any σ layer pressure $\leq$ 50mb less than p_s (300 mb) is assigned the highest computational layer relative humidity. The quality control index for each σ layer relative humidity is also the QCI of the computational layer that the σ layer pressure falls into.

A comparison of relative humidity inferred from SWO's at mandatory levels and collocated mandatory level rawinsonde relative humidities was conducted for both February and June periods using FGGE II-B observations. For each surface observation within 0.1° latitude and longitude of a rawinsonde, the observed surface pressure was used to define the boundaries of the four layers for which the mean relative humidity was to be calculated. Estimates of SWO inferred relative humidity for mandatory levels between 1000 and 300 mb inclusive were obtained by assigning the value from the computational layer that each mandatory level falls into. RMS differences and biases computed over all observation sites and all times are given in Table 11. Using a OESD of 5 percent relative humidity as suggested by Gustafsson (1981) for rawinsondes, Eq. 27 was used to estimate the OESD values for SWO inferred relative humidities based on this February study; these are included in Table 13 (below). A comparison of OESD for SWO relative humidities with the initial FESD values for relative humidity in Table 4 suggests that early in an assimilation series, the SWO relative

Table 11. Relative Humidity RMS and Bias for All Collocated SWO Inferred Values and Rawinsonde Soundings

Level (mb)	RMS (%)	Bias (%)	#OBS
	02/03/79 12Z – 02/22/79 00Z		
1000	12.8	-3.6	13554
850	21.9	5.1	23393
700	25.2	3.4	15986
500	24.1	6.0	12030
400	23.3	6.9	9536
300	21.6	5.6	8457
	06/13/79 12Z – 07/01/79 06Z		
1000	12.7	-3.1	11876
850	21.0	5.9	22975
700	24.1	1.6	14121
500	24.9	7.2	10870
400	24.6	10.2	9517
300	22.6	8.4	8183

humidities would have about the same influence on the correction as do the first guess relative humidities of the 6h forecast. However, as these forecast errors grow in magnitude in conventional data sparse regions, the SWO humidity residuals would have a greater effect vis-à-vis the first guess in computing the correction. Given the reasonable size of the bias of the SWO humidities with respect to the rawinsonde values, this could retard a drift of the analyzed relative humidity field toward "model climatology" in the assimilation sequence as would happen in these otherwise data void areas without these SWO inferred humidities.

The value of 5 percent for rawinsonde relative humidity observation error standard deviation is probably optimistic. Dey and Morone (1983) have suggested a value of 20 percent, whereas ECMWF (Illari, 1986) uses a value of 10 percent at low levels and 20 percent at upper levels. The use of 5 percent results in significantly greater modification to the first guess in the OI analysis than would these larger values. However, given the relative lack of global rawinsonde coverage and the tendency of the model to create its own humidity distribution over time in an assimilation sequence, the 5 percent value was used in the present experiments. Values closer to those used at ECMWF probably should be used in an operational environment. What is important here is the relative magnitude of the OESD for rawinsonde relative humidities to that for the inferred relative humidities. Since the emphasis in this study was to use inferred humidities only in rawinsonde void areas, the indicated differences in OESD's seemed appropriate.

The next step was to determine the spatial correlations between observation errors of relative humidity for SWO inferred values. In the case of inferred relative humidity values, the "observation error" would really be a measure of the error of estimate of the relative humidity inferred from the information given. It will be assumed observation errors of different observing systems are spatially uncorrelated, and that observational errors are uncorrelated with the true field values. Bergman (1978) showed that, if type "b" observations of a meteorological parameter are compared with collocated type "a" observations in which the latter are assumed to be spatially uncorrelated with each other, the observational error correlation between two type "b" observations at locations i and j is given by

47

$$n_{ij}^{b} = \frac{\overline{(e_{ib}\ e_{jb})}}{\overline{(e_{ib}^{2}\ e_{jb}^{2})^{\frac{1}{2}}}} = \frac{\overline{\Delta\hat{r}_{i}\ \Delta\hat{r}_{j}}}{\overline{(\Delta\hat{r}_{i}^{2}\ \Delta\hat{r}_{j}^{2})^{\frac{1}{2}}}} \qquad\qquad (31)$$

where $\Delta\hat{r}_{i} = \hat{r}_{ia} - \hat{r}_{ib}$, or the difference between observed values at each point in time and location, and the overbar represents an ensemble average over time. This means that for the above assumptions, the observational error correlations for observing system b is equal to the correlation of differences in observed values between observing system a and observing system b.

These correlations were computed for relative humidity values inferred from surface weather observations using collocated rawinsondes as the type "a" observation. Traditionally, rawinsonde relative humidity observational errors are assumed to be spatially uncorrelated, and the same assumption was made in this study to allow the correlation of difference to define the correlation of the alternative source estimation error. The above correlation was computed for each pair of relative humidity differences on separate mandatory levels over the time period 2/3/79 12Z - 2/22/79 00Z (6h intervals). Then for each mandatory level, all correlations were grouped by station pair separation distance categories (category 1: 0-49.99 km, category 2: 50-99.99 km, ..., category 40: 1950-1999.99 km) and were averaged within each category, each weighted in the average by the number of time periods included in each correlation. Results of the computation of isobaric correlations showed that the observation error correlations fell into three categories: observations at 1000 and 850 mb were appreciably less correlated than those at 700 mb and 500 mb, and even less well correlated than those for 400 and 300 mb. Thus, the correlation values in these three categories were vertically averaged (weighted by the number of pairs in all correlations over all times at the respective levels). These averages were presented previously in Table 5. Correlation values below 0.1 are neglected in the table, so that in the case of SWO's distance categories are included only out to 1750 km.

Besides the computation of lateral correlations, vertical correlation observational errors were computed for SWO inferred relative humidity at each

station for all categories of mandatory pressure level pairs. These were then averaged (each correlation in the average weighted by the number of time periods included in the correlation) over all stations to arrive at an averaged correlation for each level pair representing all stations. These averages were presented previously in Table 6.

B. 3DNEPH Analysis of Cloud Amount

A global analysis of percentage cloud amounts, generated by the Air Force Global Weather Central (AFGWC) 3DNEPH analysis model and available in magnetic tape form, was the source of the cloud analyses used in this study to infer relative humidity estimates on regular grids. Cloud amounts are available at 3h intervals on 15 levels in the atmosphere on one-eighth mesh (~25 nm) polar stereographic grids (Fye, 1978). Four steps taken to get estimates of relative humidity on mandatory levels at desired locations were: (1) determine cloud amounts at mandatory levels (vertical compaction), (2) horizontally average these to get averages on one-quarter mesh, (3) convert these cloud amounts to relative humidity, and (4) interpolate bilinearly to desired locations. In order to perform a collocation comparison of 3DNEPH inferred relative humidity with rawinsonde relative humidity, these four steps were first applied toward creating files of 3DNEPH relative humidity estimates at all rawinsonde locations for the period 2/3/79 12Z - 2/22/79 00Z at 6h intervals. Each step is described in detail in the following paragraphs.

In each of the 64x64 boxes of points in the 512x512 3DNEPH grid, vertical compaction was applied at each eighth-mesh location. This was done by using only the nine uppermost 3DNEPH cloud layers in computing a weighted average (by approximate pressure thickness of the layers) of layer pairs to form estimates of cloud amount for the layers centered on the mandatory levels 850 through 300 mb. In particular, 3DNEPH layers 7 and 8 are averaged and assigned to 850 mb, 9 and 10 to 700 mb, 11 and 12 to 500 mb, 13 to 400 mb, and 14 and 15 to 300 mb. In each case, percentage cloud amount in the range 0-100 percent was included in the averaging. An averaging was done rather than using the maximum since it was important to represent cloud amount through the layer to estimate the layer relative humidity rather than maximum cloud cover at any point in the layer. For example, if 3DNEPH layers 7 and 8 were clear and overcast respectively, a compacted cloud

amount of 50 percent cloud coverage would probably be more representative of average relative humidity through the layer centered on 850 mb than would the choice of either the minimum (0 percent) or the maximum (100 percent). From this point on in the processing, mandatory layers assigned zero cloud amount were considered missing information for estimating relative humidity.

The horizontal averaging is then performed on the five compacted mandatory layer cloud amount values at each eighth-mesh point, separately by layer. The 3x3 arrays of 3DNEPH points, each centered on every other eighth-mesh grid point in both the x and y directions, are averaged to compute a value of cloud amount for the central grid point. This results in a quarter-mesh grid of averaged cloud amount. If all nine points have cloud percent amounts between 1 and 100 percent (no clear points), a simple average of all nine points is completed. If some of the grid points have clear (no cloud) values, the eight outer grid points of the 3x3 array are divided into four sets of triangles, one in each corner of the 3x3 square. If at least one of the three grid points in each triangle indicates the presence of clouds, an average for the center of the 3x3 array is determined by computing a simple average of the cloud points. Unlike the vertical compaction in which a layer average is desired, clear values are not used in the horizontal averaging. In the case of the horizontal average assigned to the center point of each 3x3 array, the desire is to represent a cloud amount for that point as an average of the cloud amount of the nine contiguous points, rather than a cloud amount to represent an average of all of the area included in the 3x3 array. It was felt that a cloud free 3DNEPH point has no useful information to contribute to estimating humidity. If no horizontal averaging were performed, there would be no way to estimate relative humidity for a cloud free grid point distinct from a neighboring cloud free point. Even if a threshold humidity were assigned as is done in the Tibaldi SWO procedure at upper layers, all clear points would receive the same threshold value. In a comparison with rawinsonde humidities, it was felt that this would increase the error of estimation of relative humidity from the 3DNEPH fields on the whole, although this was not confirmed computationally. It is conceded that this is just one method of horizontally averaging the 3DNEPH cloud amount information; it is recommended that others be tried by comparing resulting estimated humidities

with rawinsonde humidities to determine if cloud free regions can supply any useful information to the estimates. For example, it may be argued that at the resolution of the global analysis, it may be sufficient to average all nine values of any 3x3 array that has at least one cloudy 3DNEPH point, and think of this as an average over the area of the 3x3 array and assign the corresponding humidity inferred from this area to any point that lies within it (i.e., the exactness of a spatial interpolation may be unwarranted). This would be more in keeping with what is done in the vertical compaction.

The next step was to convert the horizontally averaged (quarter-mesh grid) and vertically compacted (layers centered at 850-300 mb mandatory levels) cloud amounts to some humidity or functional cloud amount form before bilinearly interpolating them to the desired locations. This was done in three ways: (1) conversion of cloud amount to condensation pressure spread (CPS) following the AFGWC procedure (Fye, 1978), (2) conversion of cloud amount to square root of the cloud fraction for use in the ECMWF procedure (Slingo and Ritter, 1985), and (3) conversion of cloud amount to cosine of (π/100 times the percentage cloud amount) for use in the Tibaldi (1981) procedure. All three of these procedures are described in Appendix E. After these conversions, the converted quantities were bilinearly interpolated to desired locations; for the rawinsonde collocation study, to rawinsonde observation sites reporting at the corresponding synoptic time. Finally, the procedures described in Appendix E were used to estimate relative humidity from the humidity or functional cloud amount forms, with rawinsonde temperatures being used to convert dew point depression to relative humidity in the AFGWC procedure in the collocation study.

RMS differences and biases for the collocated rawinsonde relative humidities and 3DNEPH inferred relative humidities are included for the three procedures in Table 12. Results are presented for five mandatory levels 850-300 mb based on all observation sites over all 6h time periods. As in the SWO procedure, the Tibaldi procedure assigns the relative humidity value to each mandatory level using the coefficients M_L and A_L of Eq. 14 according to which computational layer the mandatory level falls into. Here, the observed surface pressure is used in the computation of the computational layer boundary pressures. It is clear from the values in Table 12 that the Tibaldi method results in the smallest differences from rawinsondes both in terms of RMS and bias. Unfortunately, it was not possible

51

Table 12. Statistics of Differences Between Relative Humidity Inferred
from Cloud Amount and That Measured with Radiosondes (in %)

02/03/79 12Z - 02/22/79 00Z

Level (mb)	#OBS	AFGWC		ECMWF		Tibaldi (from Chu-Parrish)	
		RMS	Bias	RMS	Bias	RMS	Bias
850	8251	20.9	0.6	22.2	9.8	20.3	-1.7
700	13570	26.0	2.2	29.1	15.1	25.3	-4.5
500	10837	26.3	-6.8	32.0	21.7	24.1	-4.7
400	4907	30.0	-11.6	34.3	26.0	22.7	-5.4
300	7342	36.8	-26.5	37.3	31.2	21.3	-4.7

to compute the comparable statistics for the June period at the time of this study, but it is recommended that this be done to verify that these results are not seasonally dependent (because of the greater number of rawinsonde observations in the Northern Hemisphere). However, since the present assimilation experiments were conducted for the February period, the RMS values in Table 12 from the Tibaldi procedure were used to compute the observation error standard deviation values for 3DN in Table 13 using Eq. 17. Horizontal and vertical observation error correlations for 3DN in Tables 7 and 8 were computed using Eq. 31 in a manner directly analogous to that for SWO's.

The horizontally averaged and vertically compacted cloud amounts, converted to cosine of (π/100 times the percentage cloud amount), were also bilinearly interpolated to two regular grids for use in the OI analysis. For moisture option 2 (described in Section V), values were interpolated to a regular grid, 3° latitude x 120*cos ϕ points in longitude, to act as observations in the moisture OI subroutine. For moisture option 3, values were interpolated to the 61x62 analysis grid for direct replacement of the first guess relative humidity at cloudy analysis points. In both cases, first guess surface pressure (at the "observation" site and analysis point respectively) defined the computational layers which dictated the choice of M_L and A_L in Eq. 14 to convert cos[(π/100)*% cloud amount] to relative humidity for each of the five mandatory level values according to which computational layer each mandatory level fell into. Then these five relative humidities were used to assign relative humidities to the sigma layer pressures according to the mandatory level pressure lying closest to each sigma layer pressure.

V. DESCRIPTION OF DATA ASSIMILATION EXPERIMENTS

In an attempt to determine what effect each of the three humidity options has on the humidity analyses and forecasts initiated from them, three five-day data assimilation experiments were conducted. While it was our original intent to use satellite observations of moisture along with rawinsondes for all OI phases of these experiments, the results of the collocation study precluded their use, although the software was created to include them. The three humidity options are: (1) using rawinsonde observations of moisture only, (2) using rawinsonde moisture, supplemented by relative humidity inferred from surface weather observations and 3DNEPH

53

Table 13. RH Observation Error Standard Deviation Values Used in
2/15/79 12Z - 2/20/79 00Z Experiments

Level (mb)	Rawinsonde (%)	SWO Inferred (%)	3DN Inferred (%)
1000	5	12	20*
850	5	21	20
700	5	24	25
500	5	23	24
400	5	22	22
300	5	22	21

* Assigned value not based on collocation study

cloud amounts, and (3) replace first guess relative humidity with 3DNEPH
inferred relative humidity. at cloudy analysis points, and perform OI using
rawinsonde moisture at clear analysis points. The five day period from
2/15/79 00Z - 2/20/79 00Z was chosen because of the considerable amount of
literature published on comparison of analyses and forecasts during this
period [e.g., Hollingsworth et al., (1983)].

The starting analysis for all three experiments was extracted from the
FGGE III-A global analysis set for 2/15/79 at 00Z. Analysis values of Z, T,
u, v, on a 144x73 (2.5°x2.5° longitude-latitude) grid on mandatory levels
1000-50 mb and r on mandatory levels 1000-300 mb were linearly interpolated to
the 62 Gaussian latitudes of the analysis grid, with every other point in
longitude being used. Resulting 72x62 values of Z, T were used in the GETPS
routine described in Appendix F to obtain corresponding grid values of p_*,
using the corresponding 72x62 FGGE Fixed Field values of Z_*. Sigma layer
values of T, u, v and q (lowest MLRH layers for q) are obtained using the
routine PTOSIG, where here the data reside strictly on mandatory levels. The
previously determined values of p_* are used to define the σ layer
pressures at each point. Finally, the 72x62 σ layer fields of T, u, v, q,
and the 72x62 values of p_*, Z_* are converted to 30 wave rhomboidal
spectral forms of η, D, T, q, p_*, Z_* using the Fast Fourier transform
and Gaussian quadrature integration techniques. Spectral versions of FGGE
III-A fields were formulated in like manner at all 00Z, 12Z times in the
experimental period to act as a basis of comparison for the data assimilation
analyses.

The Machenauer non-linear normal mode analysis was then performed on the
spectral FGGE III-A fields for 2/15/79 00Z, using two iterations and four
vertical modes. Then the AFGL global spectral model took these initialized
data as input and provided a 6h forecast valid at 06Z. This was the starting
first guess for all three data assimilation experiments. For the first cycle
in all three experiments, the forecast error standard deviation values for Z
in Table 1 and r in Table 4 were used in the respective analyses. In
subsequent analyses, FESD values were obtained by augmenting the analysis
error from the previous analysis by the forecast error growth rate. Each
cycle consists of the sequence of four analysis steps (pre-analysis,
mass-motion analysis, humidity analysis, post analysis), the normal mode

55

initialization, and the 6h global forecast. All computing was performed on a
CDC CYBER 860 with 367K octal words of core memory and 1720K octal words of
extended core memory. A typical run of the six programs in each cycle for
moisture option 1 during 00, 12Z times took about 5500 sec of central
processing time, of which 45 percent consisted of the mass-motion analysis,
and 39 percent was attributed to the 6h forecast.

VI. EXPERIMENTAL RESULTS

A. Mass-Motion Analyses

Because this series of experiments represents the first test of the ASAP
data assimilation system in its current complete, updated form, it was of
interest to examine its ability to perform the basic assimilation of height
and winds. While in the meteorological community there is no definite
consensus on how to assess the accuracy of the analyses produced in a data
assimilation system, it is agreed that the analysis should fit the
observations fairly well and that this fit should not change significantly
in time. Also, in a good analysis most of the information introduced into
the analysis from the observations should be retained in the initialization
of the analyzed fields. Finally, the longer-term forecasts initialized from
such fields should verify with observations and later analyses in a manner
that shows a relatively constant growth of the forecast error with
simulation time. In the following paragraphs, results of the height-wind
analyses will be demonstrated to show how well the ASAP data assimilation
system results conform to these standards. In this section, results from
Experiment 1 only will be shown since the mass-motion analysis was carried
out in the same way in all three experiments.

Figs. 3 and 4 show the RMS differences between each of the three fields
produced at each analysis time - 6h forecast (GSM), ASAP analysis (ANL), and
the initialized analyses (INT) - for Z and $\vec{V}$. Here $\vec{V} = \{\frac{1}{N} \sum_{i=1}^{N} [(u_{f_i} - u_{o_i})^2 +$
$(v_{f_i} - v_{o_i})^2]\}^{1/2}$ for N observation values u_o, v_o and field values u_f, v_f.
Corresponding RMS differences for the FGGE III-A fields, truncated to
rhomboidal 30 waves and interpolated to σ levels/layers, are shown (F3A)
for comparison. In fact, the F3A and ANL fields were used to select the set
of basis observations used in the RMS and bias computations. After
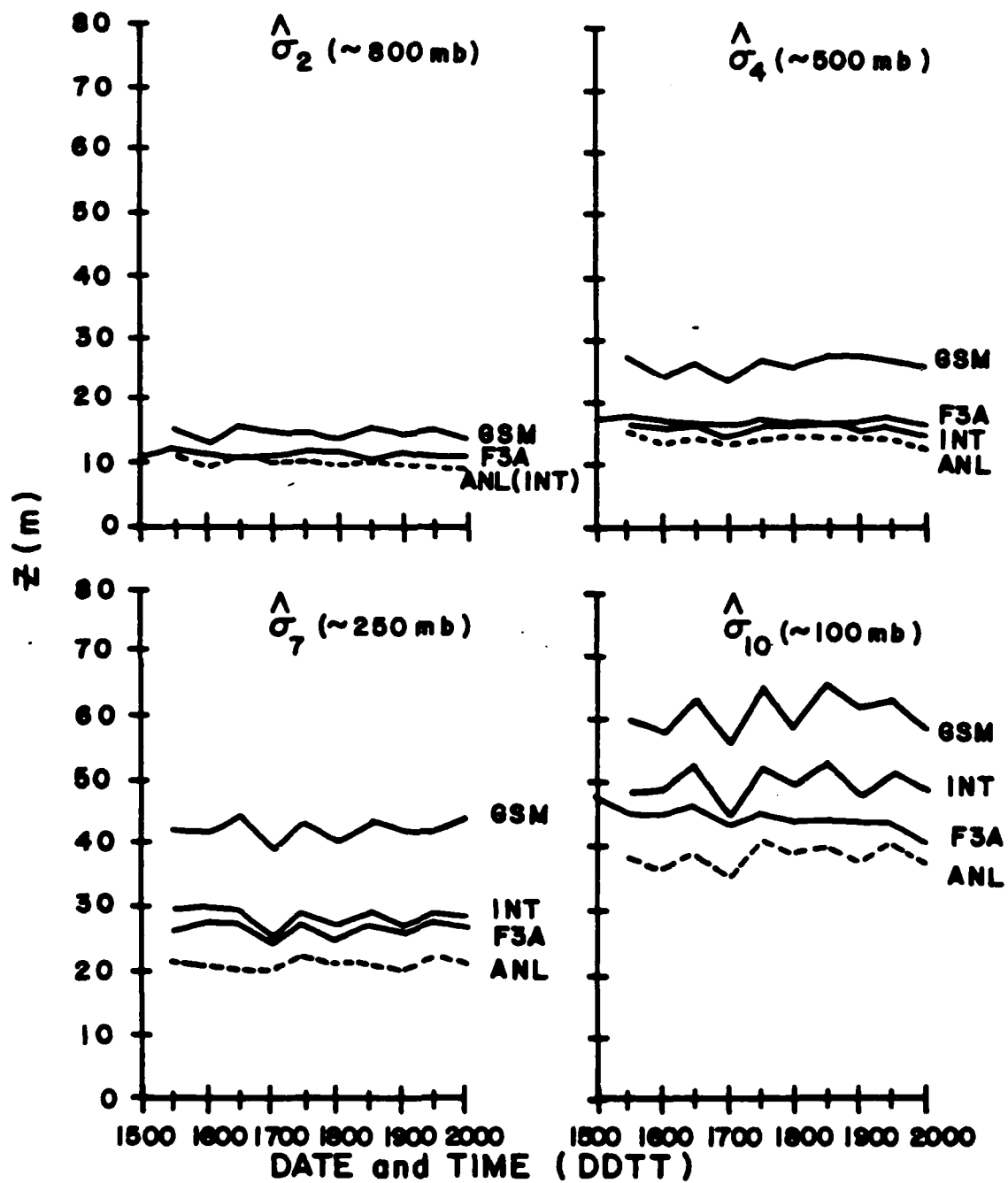
Fig. 3 RMS Differences on σ Levels between Height Fields and Basis
Observations
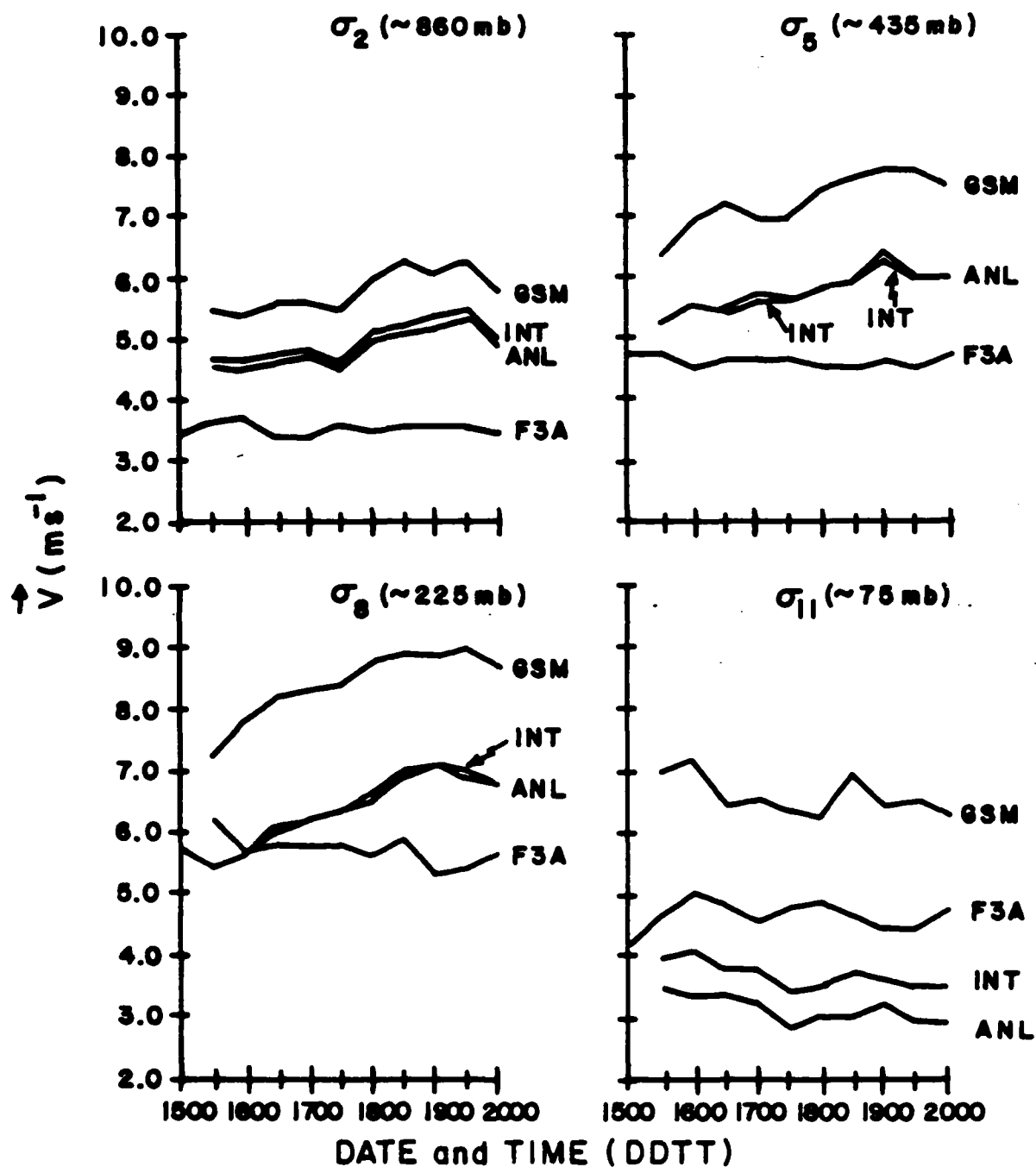
Fig. 4   RMS Differences on σ Layers between Vector Wind Fields and
         Basis Observations

computing observation-minus-field residuals for both F3A and ANL, both sets of residuals were individually gross checked and buddy checked. Then only those residuals that survived the checks in both sets were included as basis observations. All other fields had residuals computed in the same way, but only their residuals for the same locations as the basis observations were used in the computations. The intent of this procedure was to arrive at a more neutral set of observations against which to compare the field-observation differences that would not favor one analysis over the other.

Immediately noticeable from the figures is the fact that the ANL values for Z show a better fit with observations than do the F3A values at all levels shown, while the F3A RMS differences for $\vec{V}$ are smaller than those for ANL at all levels shown except σ_{11}. Furthermore, there seems to be no perceptible increase of RMS difference with time in the ANL Z curves, yet with the exception of the σ_{11} ANL curve all ANL curves for $\vec{V}$ show somewhat of an increase of RMS difference up to a certain point and then appear to level off. An explanation for the relatively good fit with observations for Z and upper level $\vec{V}$ and poorer fit for lower level $\vec{V}$ lies in the fact that these RMS differences reflect a univariate comparison. They are very much dependent upon how much influence Z observations have in correcting Z first guess values, and that u, v observations have in correcting u, v first guess values. Since both height and wind observations are used to correct both height and wind first guess, the fit of the resulting analysis with observations will be best in those areas where observations of the variable being corrected hold more influence than their geostrophic counterpart. Ratios of the normalized observation error for height to those for winds, shown in Table 2, play the most important role in determining the relative influence of height and wind observations surrounding an analysis point. Since normalized observation error affects the magnitude of the correlation $\rho' = \rho/(1 + \epsilon^2)$ of the observation with the analysis point, observations with lower values of ϵ are both more likely to be chosen in the analysis and will have more weight in the computation of the correction. Values of $\epsilon_z/\epsilon_{u,v}$ in Table 2 show a clear preference for height observations over wind observations in levels below 200 mb for extratropical latitudes. This agrees with the relative goodness of fit of the height analysis over the wind analysis at the lower levels. Notice that

at the uppermost levels, where rawinsonde height errors are set much higher, the $\epsilon_Z/\epsilon_{u,v}$ ratio becomes much greater than unity and the analysis is more favorable toward the wind observations. This explains the considerable better fit of the winds analysis to observations, which occurred at σ_{10}, σ_{11} and σ_{12} (~ 124, 74, and 21 mb). More support for this explanation was provided when the RMS fit with observations was separated into tropical ($|\theta| \leq 25°$) and extratropical regimes. In the tropical latitudes where the analysis is much more univariate in nature, the RMS differences between ANL and observations for $\vec{V}$ were lower at all σ layers than they were for F3A, whereas in the higher latitudes the F3A - ANL curves retained their indicated relationship. Also, it should be pointed out that Bergman (1979) used a constant $\epsilon_T/\epsilon_{u,v}$ ratio of 1.20 for rawinsondes in his analysis, and it was the Bergman analysis procedure that was used to generate the FGGE III-A analyses. This explains the generally better fit of the $\vec{V}$ F3A analyses and poorer fit of the Z F3A analyses as compared with their ANL counterparts. These results point out the danger in basing a determination of quality of an analysis, especially one to be used to initialize a forecast model, solely on the basis of goodness of fit with observations. It is better to use goodness of fit as a trouble shooter criterion in analyses for initializing forecast models, indicating problems as they may exist by showing significantly large RMS errors or large error drifts in time in a data assimilation mode. Finally, a comparison of the $Z(\hat{\sigma}_4)$ RMS curves with the 500 mb RMS curves for the NMC GDAS (Dey and Morone, 1985) shown in their Fig. 4 shows good agreement between the RMS levels, both in the 15-20 m range for the analysis and 25-30 m for 6h forecasts. A comparison of the $\vec{V}(\sigma_8)$ RMS curves with the 250 mb RMS curves in Fig. 5 of Dey and Morone shows that the ANL, GSM curves appear to be leveling off at levels (6.5 - 7.0 ms^{-1} and 8.5 - 9.0 ms^{-1} respectively) in fairly close agreement with the level of the NMC curves. Note that since the 2/15/79 00Z starting analysis was the FGGE III-A, the difference grows from its lower level throughout the five day period to its apparent equilibrium level in the lower σ layers, while it appears to decrease from its FGGE III-A level in the upper σ layers. This good agreement between NMC and the present AGDAS results no doubt stems from the close similarity between the forecast models and analysis methods used for both, and especially from the use of the same observational errors for both studies.

In order to verify that the wind RMS differences are in fact leveling off at the end of the five day period, the ASAP option 1 assimilation experiment should (but could not) be carried out two more days.

Bias for height and wind AGDAS fields against basis rawinsonde observations was also diagnosed as a potential trouble indicator; however, only bias for Z at four selected times in the five day period is illustrated here (Fig. 5). The outstanding feature in the time evolution of the height bias is the apparently unabated growth of positive bias at the $\hat{\sigma} = .050$ level in the ANL, INT, and GSM fields. At all other levels, the growth of positive bias occurs, but appears to remain relatively constant after 2/17/79 00Z. In all levels, the ANL appears to represent a significant correction to the GSM bias, but the ensuing initialization tends to increase the positive bias again. At levels .925 - .100, the fact that the bias has appeared to reach a steady value would suggest that the analysis was effective in compensating for the positive bias being introduced in the 6h forecast at these levels. This is evidently not the case for $\hat{\sigma} = .050$, and a possible explanation for this could be the relatively large observation error assigned at this level (59.3) resulting in relatively larger normalized observation errors and poorer fits to the data. Another possible explanation is the use of the smaller radial influence factor ($k_h = 1.0$ x $10^{-12} m^{-2}$) resulting in larger correlations assigned to more distant observations and thus a lessened fit with nearby observations. Kistler and Parrish (1983), in a similar comparison of the GDAS with the NMC hemispheric nine layer model assimilation, showed much larger positive bias at 100 mb in their GDAS in tropical regimes, but were more comparable in extratropical regimes. They attributed this difference to the GSM system's inability to resolve the tropopause temperature profile in the tropics near 100 mb. However, when the bias in the ANL, INT, and GSM fields for 2/17/79 00Z was computed separately for latitudes poleward and equatorward of 25° latitude, the large positive bias was evident in both regimes at $\hat{\sigma} = .050$; in fact, the positive bias was somewhat larger in the extratropics. The source of this bias should be studied further before any really profitable analysis fields can be produced at the uppermost levels. Notice that the FGGE III-A fields reveal a somewhat more modest negative bias at the $\hat{\sigma} = .050$ level.

As for the bias in the wind components, results of the five day assimilation experiment showed a moderate growth of positive bias in the u
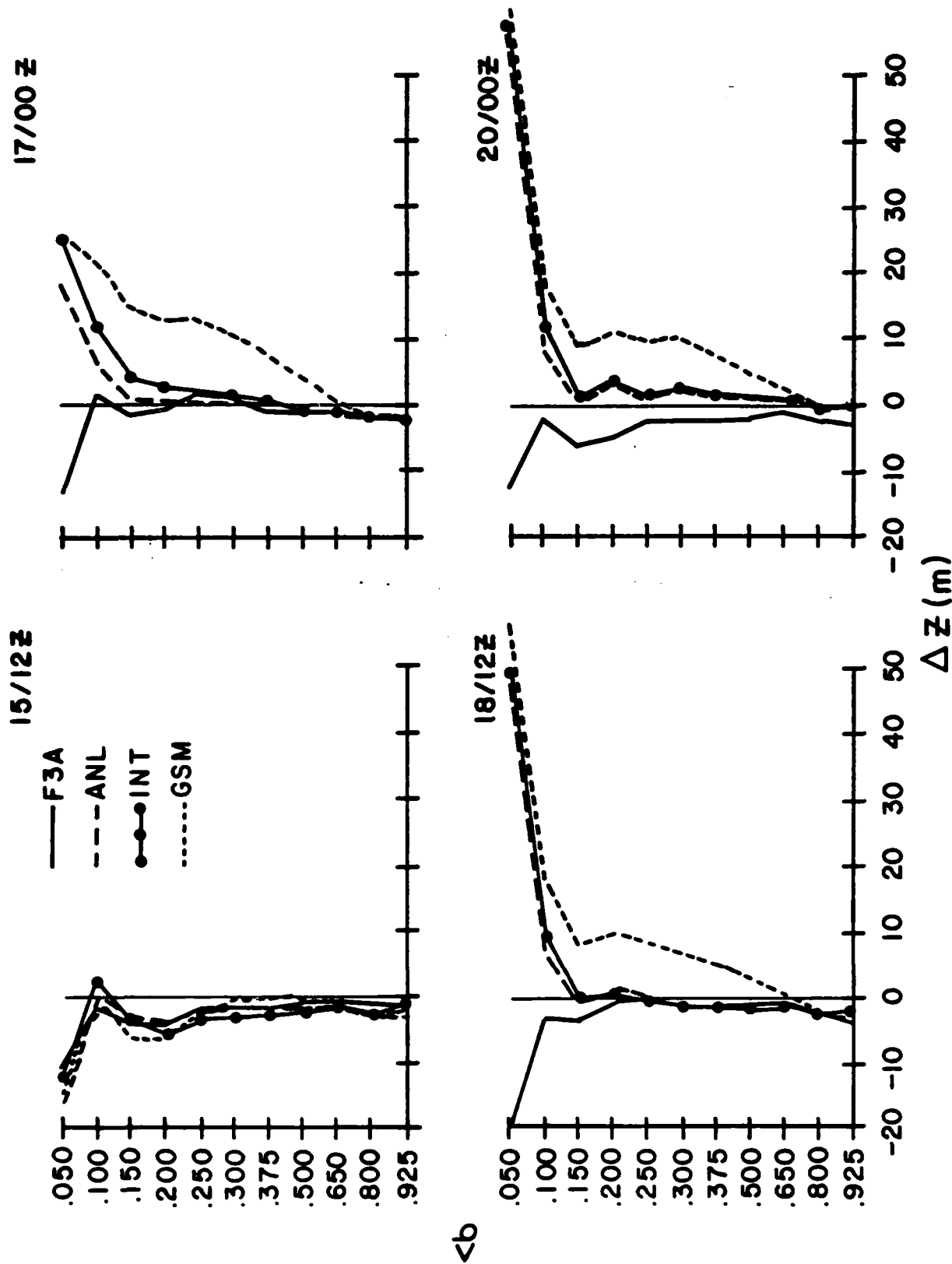
Fig. 5 Field-Observation Bias for σ Level Heights (Basis Observations)

component at σ_2 and σ_5 and of negative bias of v component in wind at σ_8, both of which appear to level off at about the 1.0 ms^{-1} level about mid-way through the period. Also of interest was a decrease in a positive bias in u at σ_{11} in the GSM, INT fields only from about 1.8 m s^{-1} at the beginning to 1.2 m s^{-1} at the end of the period. Interestingly, no significant bias was apparent in the corresponding ANL fields. Thus it appears that the wind biases suggest no apparent trouble areas in the wind data assimilation.

Time evolution of the global average of the analyzed fields was examined as an additional indicator of meteorological realism of the analyses. Figs. 6-8 illustrate the change of global average of temperature, kinetic energy, and surface pressure through the five day period. Global averages of the FGGE III-A fields are shown for comparison. While no clear trends are evident in the temperature curves for σ_4 and σ_7, both σ_2 and σ_{11} curves show a clear growth of the globally averaged σ layer temperature with time. At the lower level, there appears to be a leveling off of the growth after an increase of about 0.8°K at 2/18/79 00Z; however, this should be confirmed through following analyses. No such indication of leveling off is evident in the σ_{11} curve, and in fact the warming indicated at that layer is consistent with the growth of positive bias of Z at $\sigma = .050$ (the level at the top of σ layer 11) as shown in Fig. 5. The σ_{11} global mean temperature grows so fast in time, as compared to the slight trend toward cooling at σ_{10}, the σ_{10} layer becomes the layer of minimum global mean temperature (labelled "TROP") at 2/18/79 00Z. The F3A σ_{10}, σ_{11} curves maintain the relative global average layer temperature relationship for these two layers. This gives additional support to the idea that the anomalous warming in the data assimilation period is confined to the layer above $\sigma = .100$. Fig. 7 does not reveal any similar troubling features in the evolution of the global average kinetic energy. There appear to be similarities between the trends reflected in the F3A and ANL curves. For example, both σ_8 curves show a growth of kinetic energy through 2/17/79 12Z, then a relative leveling off of the trends beyond that point. The surface pressure curves in Fig. 8 reveal no untoward growth or decline through the period. F3A curve indicates a small trend toward an increase in the global average surface pressure, while the ANL curve suggests an even smaller tendency toward
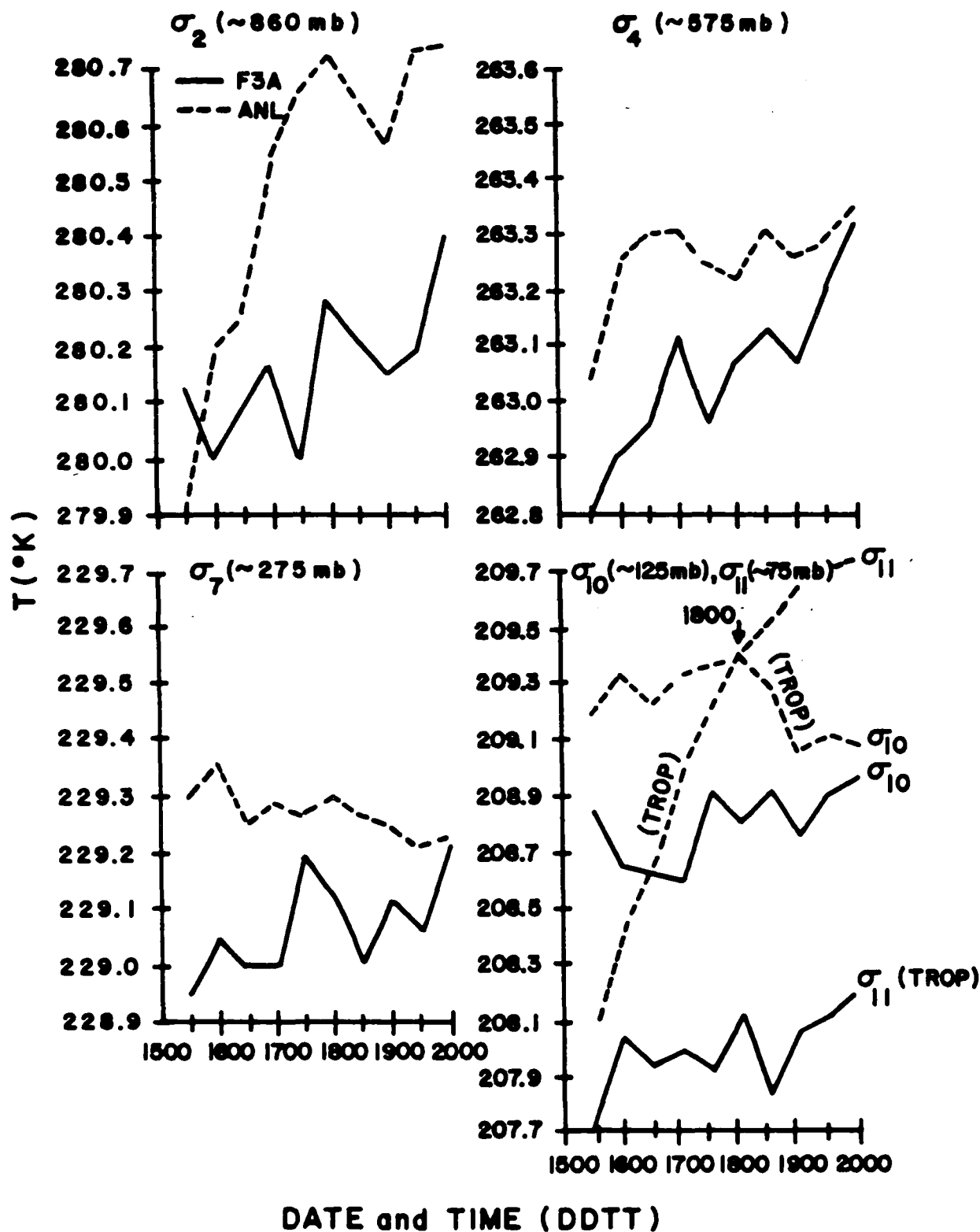
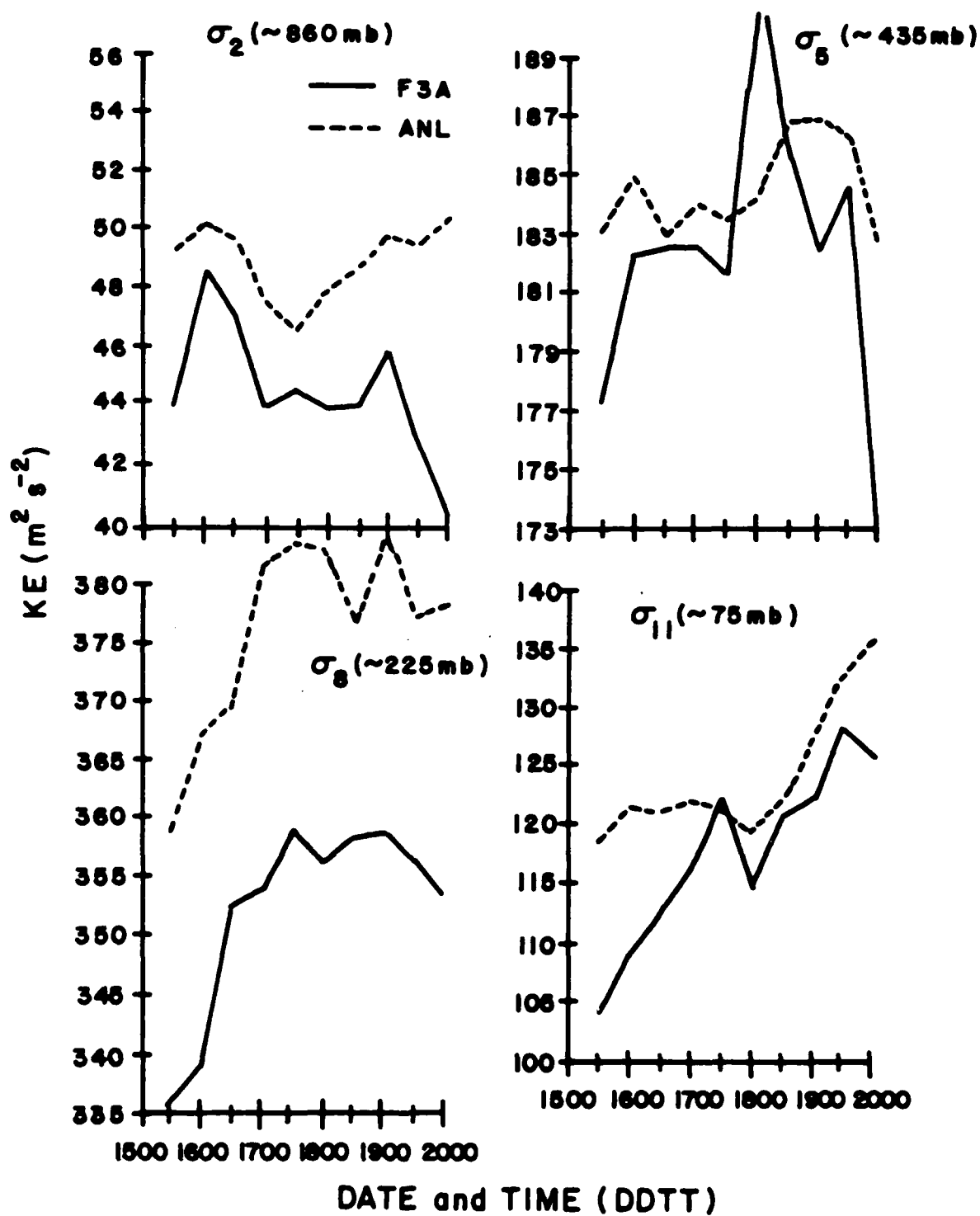Fig. 6 Global Average σ Layer Temperatures for Analysis Fields

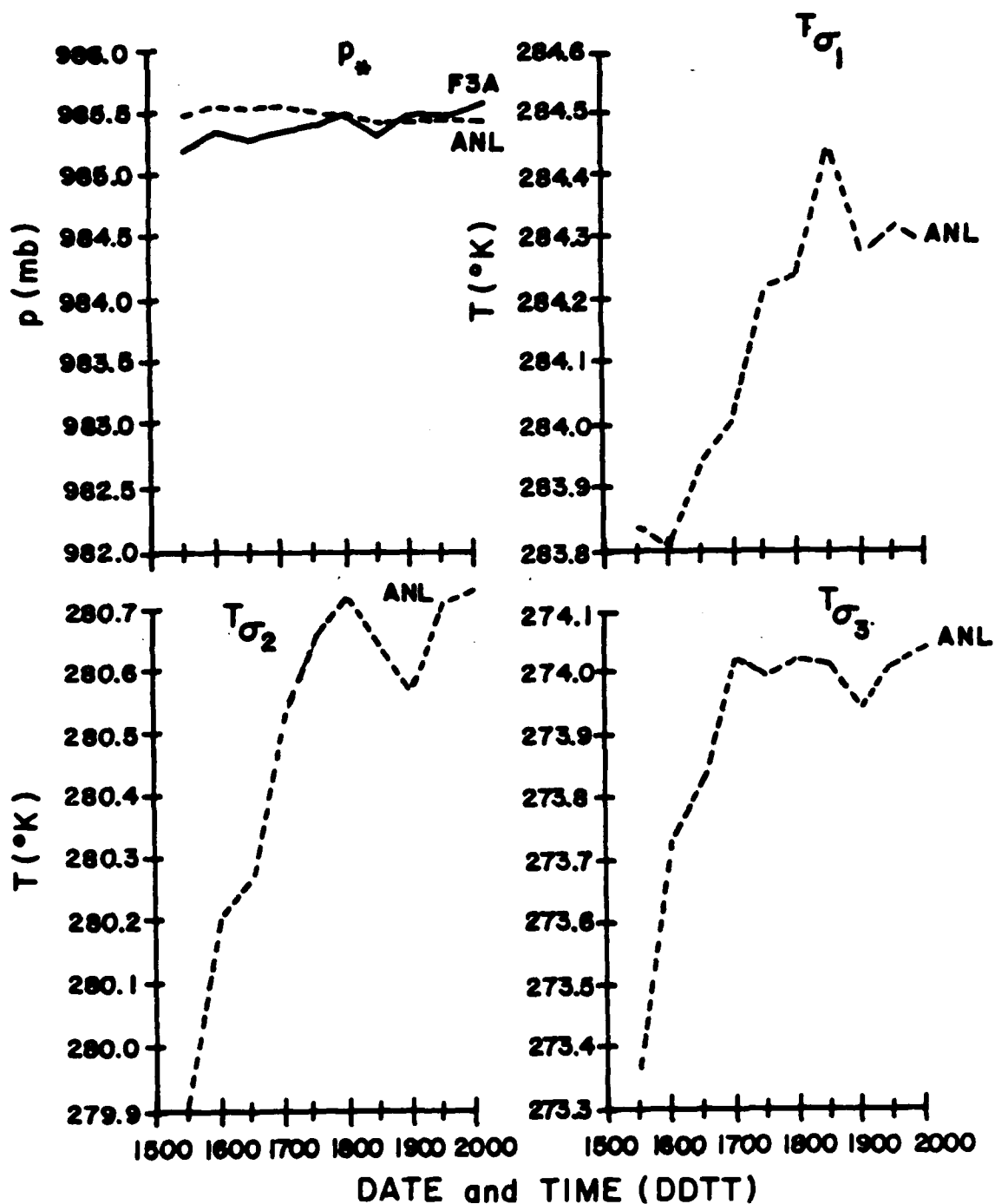Fig. 7   Global Average σ Layer Kinetic Energy for Analyzed Fields

Fig. 8   Global Average Surface Pressures and σ Layer Temperatures of
Analyzed Fields

decrease, though probably statistically insignificant. The accompanying σ
layer temperature curves in Fig. 8 are shown because of the fact that these
are used with surface geopotential to obtain σ level geopotential at the
lowest three σ levels, from which analyzed surface pressure is diagnosed
(see Appendix B). It is interesting that the layer temperature increases
seen in the first half of the assimilation period are not reflected in any
perceivable way in the diagnosed surface pressure. Further study of the
surface pressure–analyzed geopotential relationship should be conducted to
better understand the effect of change of geopotential on change of surface
pressure.

Another measure of the effectiveness of an analysis method in imparting
useful observational information to the correction of the forecast first
guess is the amount of observational information retained in the analysis
after it has been initialized. In removing the fast gravity mode tendencies
in the analysis field, the initialization procedure produces a field which
contains only the slow modes (lower frequency oscillations), which are the
only ones useful to the model. It is then of interest to determine how much
observational information imparted by the analysis consists of slow
modes—that is, how much is left behind after the analysis. The RMS
difference between the analyzed and initialized fields is a measure of the
fast mode information in the analysis that was removed due to the
initialization. Similarly, the RMS difference between the forecast and
initialized forecast is a measure of the fast mode information introduced by
the forecast model. The difference between the second difference (fast mode
in forecast) and the first difference (fast mode in analysis) would then be
the fast mode information resulting from the update to the forecast field by
the analysis. Then if the initialized analysis contains only slow modes in
the analysis field, and the initialized forecast contains only slow modes in
the forecast field, the RMS difference between the two would be a measure of
the slow modes due to the analysis. Values for the analysis fast mode/slow
mode ratio based on RMS differences averaged over the ten time periods along
with the RMS differences between the fields themselves are given in Tables
14 and 15. Lower values of this ratio indicate a greater effectiveness of
the analysis method in imparting the useful slow mode information into the
corrected first guess. Results show a clear increase of this ratio with
altitude for heights but a relatively steady value with altitude for winds.

67

Table 14. RMS Differences Between Fields and Fast Mode/Slow Mode Ratio for the 10 Time Period Averages for Heights

		1512	1600	1612	1700	1712	1800	1812	1900	1912	2000	AVE	$\frac{(A-I)-(G-GI)}{I-GI}$
$Z(\hat{\sigma}_2)$ (m)	G-A	6.20	6.20	6.85	6.40	6.16	6.59	7.46	7.38	7.52	7.15		
	A-I	0.65	0.81	0.85	0.80	0.74	0.82	0.88	0.85	0.88	0.84	0.81	
	G-I	6.06	6.00	6.67	6.20	5.98	6.42	7.28	7.26	7.26	6.92		0.10
	G-GI	0.16	0.16	0.14	0.14	0.14	0.15	0.16	0.20	0.16	0.15	0.16	
	I-GI	6.05	6.00	6.66	6.19	5.98	6.42	7.28	7.26	7.25	6.91	6.60	
$Z(\hat{\sigma}_4)$ (m)	G-A	13.94	13.84	14.86	14.09	14.02	14.25	15.61	16.08	16.43	15.88		
	A-I	4.59	5.71	5.60	4.98	4.92	5.14	5.66	5.59	5.61	5.61	5.34	
	G-I	12.84	12.02	12.93	12.55	12.75	12.96	14.16	14.69	14.67	14.03		0.28
	G-GI	1.57	1.58	1.45	1.39	1.39	1.36	1.56	1.98	1.66	1.56	1.55	
	I-GI	12.74	11.90	12.91	12.46	12.65	13.02	14.19	14.63	14.56	14.01	13.31	
$Z(\hat{\sigma}_7)$ (m)	G-A	22.16	24.99	25.74	23.26	23.85	23.80	25.50	25.21	25.42	26.77		
	A-I	13.32	15.90	15.93	13.52	13.55	13.96	15.50	15.62	15.35	15.71	14.84	
	G-I	17.45	17.71	18.62	18.83	18.45	18.62	20.25	19.90	19.26	19.88		0.57
	G-GI	4.11	4.13	3.84	3.61	3.60	3.46	4.05	5.26	4.38	4.14	4.06	
	I-GI	17.43	17.46	18.59	18.63	18.44	18.59	20.26	19.61	18.86	20.10	18.80	
$Z(\hat{\sigma}_{10})$ (m)	G-A	31.48	34.51	32.79	28.30	26.92	26.94	30.25	34.30	32.61	31.78		
	A-I	18.99	22.33	20.96	18.35	17.26	18.37	18.56	19.71	19.67	20.47	19.47	
	G-I	21.65	21.96	21.08	18.92	18.06	17.13	21.32	24.55	21.62	20.25		0.81
	G-GI	3.10	2.74	2.74	2.75	2.76	2.45	2.87	3.42	2.94	2.87	2.86	
	I-GI	21.30	21.79	20.86	18.73	18.05	17.17	21.28	24.31	21.52	29.23	20.52	

G: GSM   A: AML   I: INT   GI: INT GSM

68

Table 15. RMS Differences Between Fields and Fast Mode/Slow Mode Ratio for the 10 Time Period Averages for Vector Winds

		1512	1600	1612	1700	1712	1800	1812	1900	1912	2000	AVE	$\overline{\dfrac{(A-I)-(G-GI)}{I-GI}}$
$\vec{V}(\sigma_2)$	G-A	2.03	2.04	2.19	2.18	2.16	2.26	2.57	2.35	2.23	2.16		
(m s^{-1})	A-I	0.80	0.80	0.92	0.90	0.94	0.94	1.06	1.02	1.00	0.91	0.93	
	G-I	1.94	1.95	2.09	2.09	2.04	2.17	2.43	2.24	2.14	2.09		0.32
	G-GI	0.25	0.25	0.23	0.23	0.23	0.23	0.26	0.27	0.29	0.24	0.25	
	I-GI	1.91	1.94	2.08	2.07	2.03	2.16	2.41	2.22	2.11	2.08	2.10	
$\vec{V}(\sigma_5)$	G-A	3.04	3.30	2.92	3.38	3.63	3.78	4.04	3.83	3.92	3.83		
	A-I	0.81	0.86	0.87	1.04	0.99	1.09	1.20	1.09	1.04	0.99	1.00	
	G-I	2.96	3.21	2.78	3.24	3.51	3.65	3.86	3.71	3.79	3.70		0.25
	G-GI	0.16	0.17	0.07	0.16	0.16	0.15	0.18	0.18	0.18	0.16	0.16	
	I-GI	2.95	3.21	2.78	3.24	3.50	3.64	3.85	3.71	3.03	3.70	3.36	
$\vec{V}(\sigma_8)$	G-A	4.40	5.07	5.21	5.30	5.37	5.60	5.95	5.78	5.26	5.37		
	A-I	1.17	1.26	1.36	1.47	1.40	1.55	1.63	1.56	1.39	1.38	1.42	
	G-I	4.31	4.95	5.05	5.00	5.18	5.31	5.64	5.00	5.06	5.24		0.19
	G-GI	0.43	0.44	0.42	0.42	0.41	0.41	0.46	0.49	0.51	0.42	0.44	
	I-GI	4.27	4.92	5.01	4.98	5.16	5.30	5.62	4.97	5.05	5.22	5.05	
$\vec{V}(\sigma_{11})$	G-A	4.47	4.70	4.21	4.09	4.07	3.90	4.33	4.23	4.28	4.41		
	A-I	1.31	1.42	1.37	1.46	1.35	1.34	1.38	1.36	1.43	1.39	1.38	
	G-I	4.10	4.35	3.95	3.78	3.78	3.62	4.03	4.06	4.00	4.16		0.24
	G-GI	0.43	0.43	0.39	0.41	0.41	0.38	0.45	0.46	0.47	0.42	0.43	
	I-GI	4.10	4.33	3.93	3.76	3.75	3.59	4.00	4.03	3.98	4.14	3.96	

G: GSM A: AML I: INT GI: INT GSM

Unfortunately, it was not possible to obtain this ratio for FGGE III-A as a comparison as all four assimilation fields are necessary for this computation. It is apparent that at upper levels for heights, the initialization makes a significantly larger change in the analysis (over 90 percent of the G-I difference at $\hat{\sigma}_{10}$) than at lower levels (approximately 10 percent of the G-I difference at $\hat{\sigma}_2$). Apparently the analysis provides a considerably lesser amount of useful observational height information to the forecast correction at upper levels than at lower levels.

To the weather forecaster, the best measure of an analysis is the accuracy of the forecast produced from it. The closeness of fit of the analysis or the initial conditions is of secondary importance to the fit of the forecast field to observations at the valid forecast time. As a test of the conformity of the ASAP analyses to this standard, a 48h forecast using the GSM was conducted using the initialized FGGE III-A and ASAP analyses at 2/17/79 12Z, exactly half-way through the five day assimilation experiments. Resulting spectral forecast fields at 12h intervals were evaluated at 1° x 1° grid intervals, and bilinearly interpolated to the locations of the basis observations for each verification time. Meanwhile, the observations were interpolated to the σ level/layer pressures of the forecast fields and the observation-minus-forecast field residuals were computed. The basis observation subset of these residuals was used to construct the RMS and bias curves shown in Figs. 9-13. The RMS and bias curves for the 2/17/79 12Z analyses are included in the first plot as a reference. The RMS curves reveal an interesting relationship between the importance of the fit of the initial height fields to observations and the initial fit of winds in the fit of the forecast field. The better fit of the ANL (ASAP) analysis initially is soon lost in the forecast, especially at the upper levels. The gap between the height forecast RMS for FGGE III-A and ASAP widens gradually with time at those levels, to become about 12 m at $\hat{\sigma}$ = .100 for 48h. However, by this time differences below about 500 mb are slight. By contrast, the gaps between the $\vec{V}$ RMS curves remain essentially constant in time, widening only slightly from 12h to 48h. It appears that the initial fit played a more significant role in the forecast verification for the winds than for the heights. All eight sets of curves move constantly toward higher RMS values with time, but the wind curves
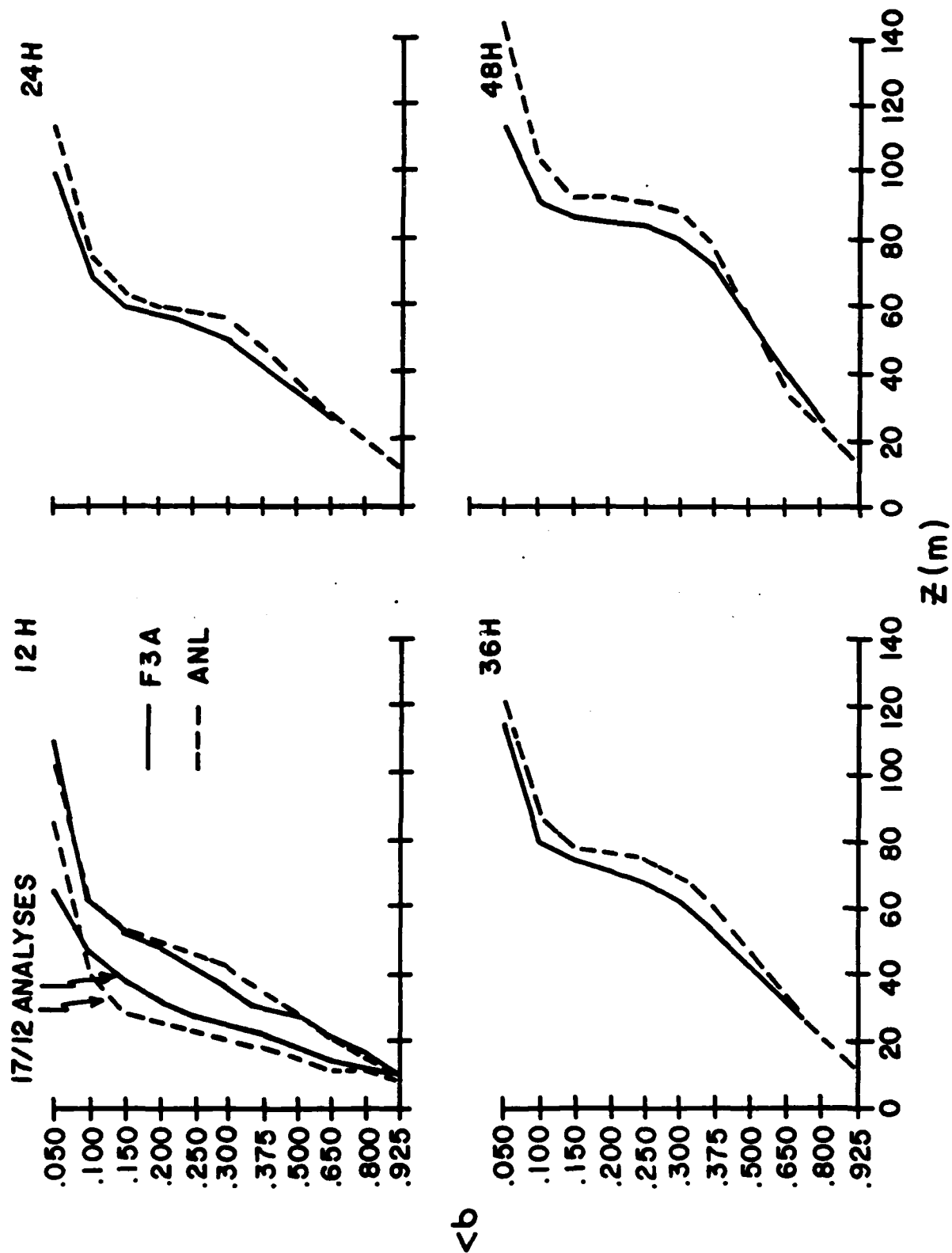
Fig. 9   RMS Differences on σ Levels between Forecast Height Fields and Basis Observations

71
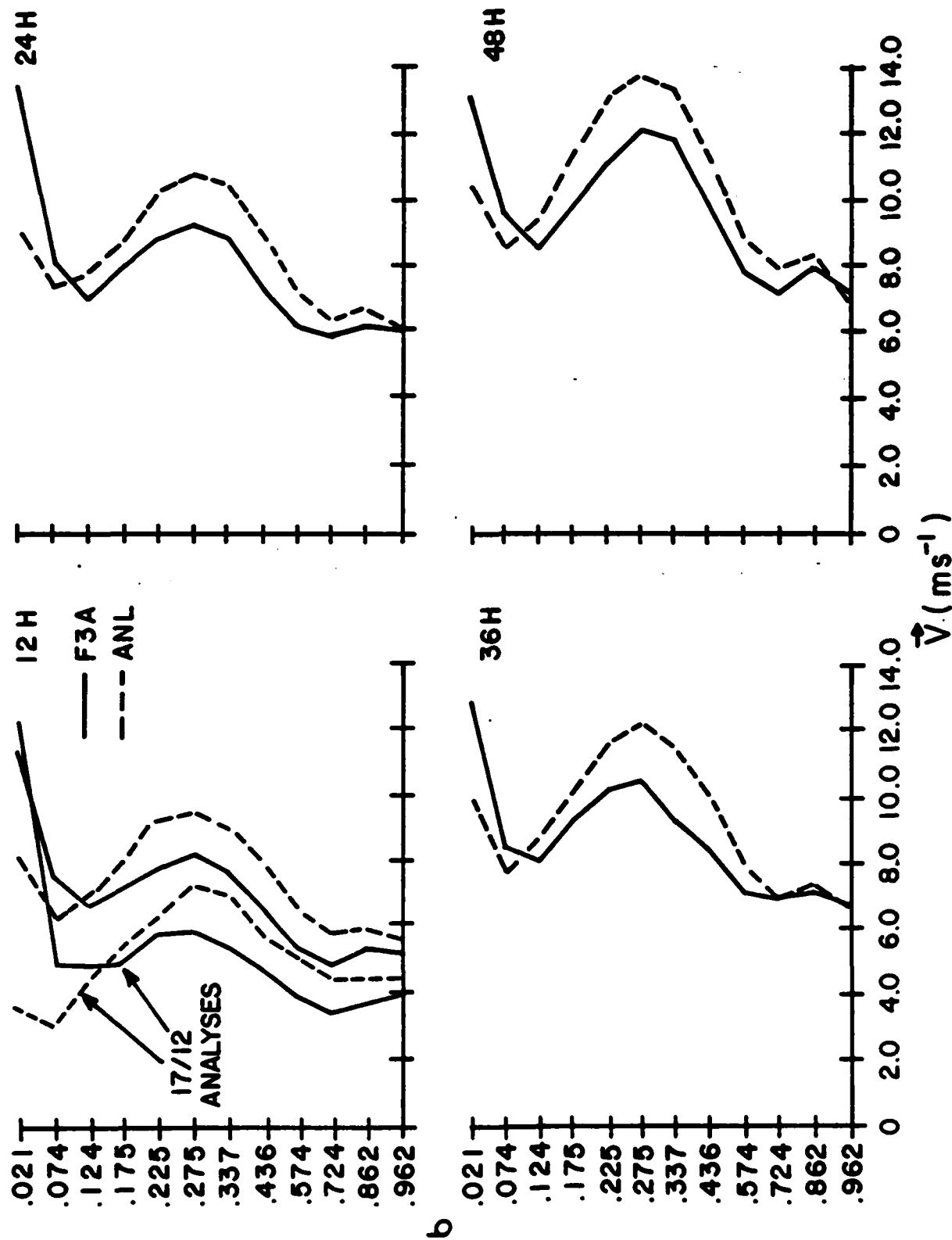
Fig. 10 RMS Differences on σ Layers between Forecast Vector Wind Fields and Basis Observations

72
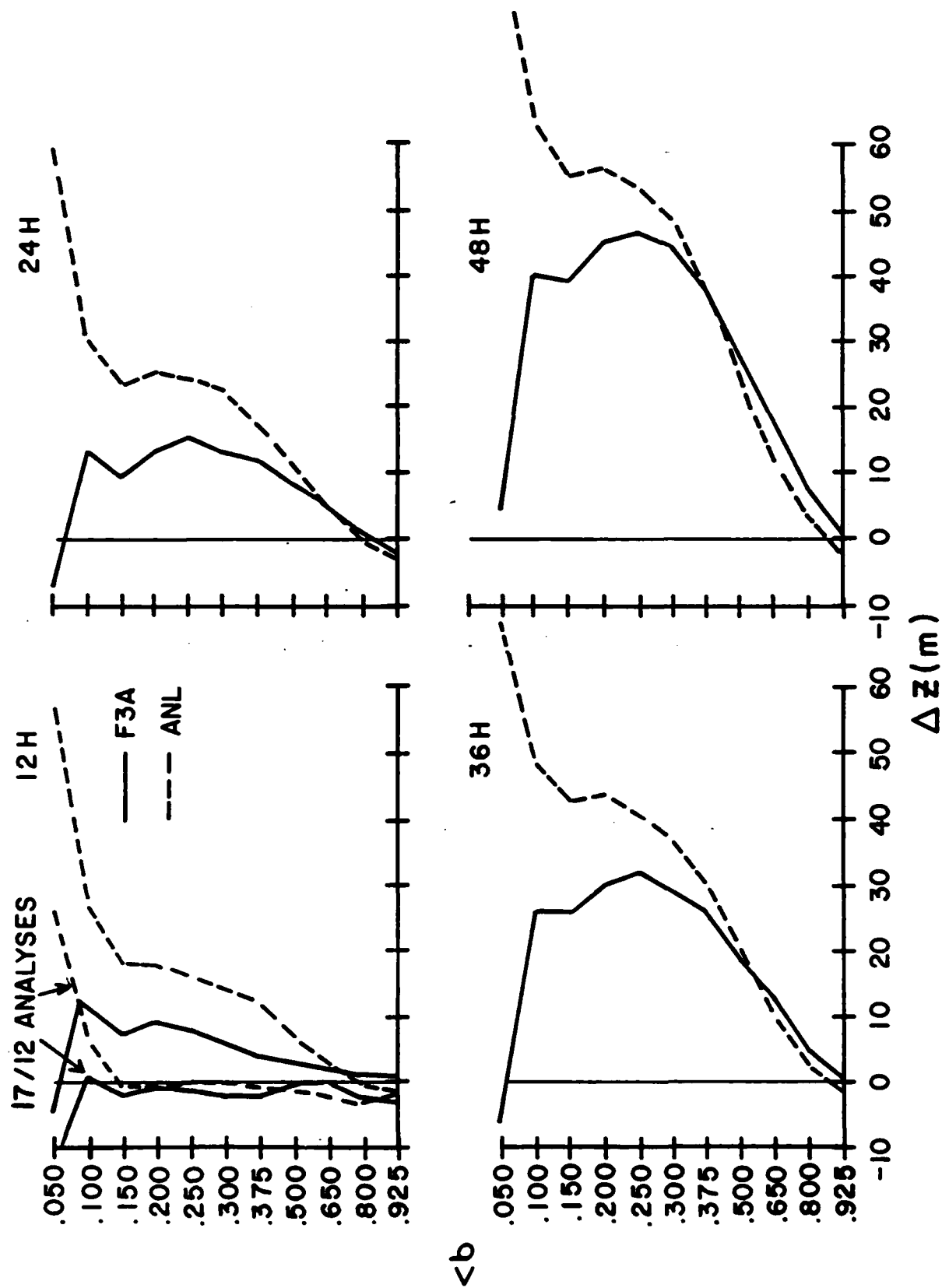
Fig. 11 Forecast Field - Observation Bias for σ Level Heights (Basis Observations)
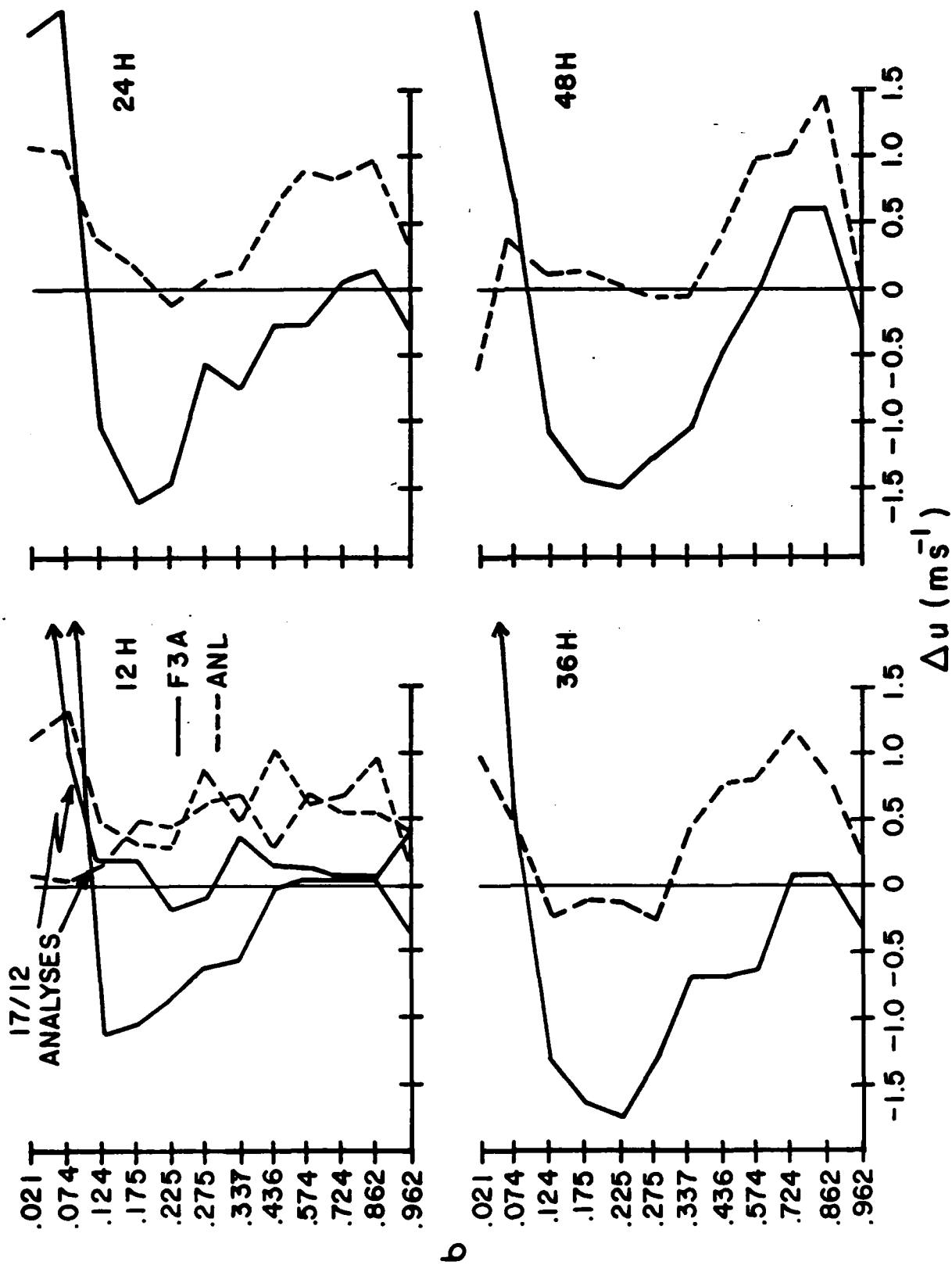
Fig. 12 Forecast Field – Observation Bias for σ Layer Zonal Component of Wind (Basis Observations)

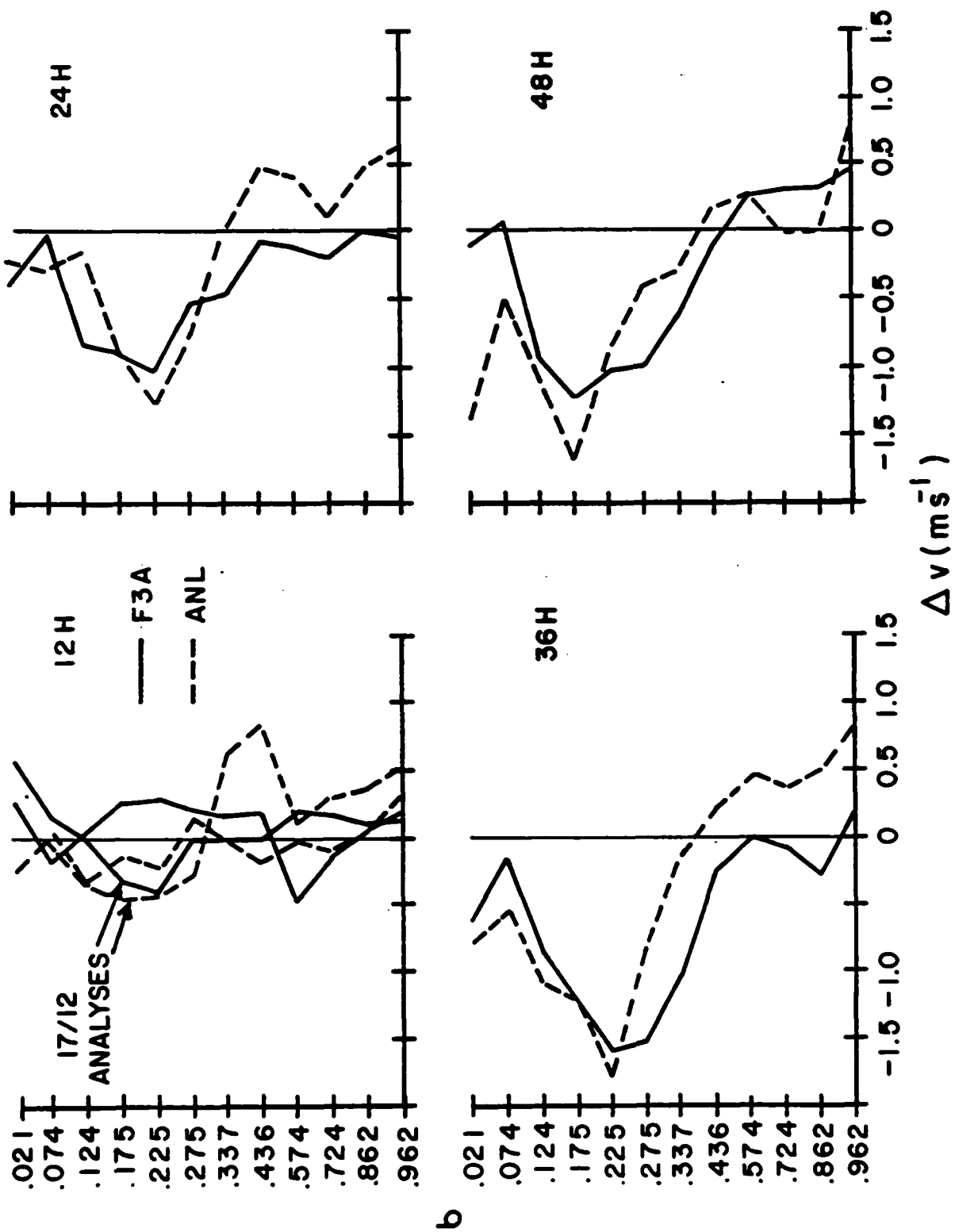Fig. 13 Forecast Field - Observation Bias for σ Layer Meridional Component of Wind (Bias Observations)

essentially retain their relationship whereas the gap between the height curves widens. Caution must be taken in attempting to draw too many conclusions from a single forecast experiment. A series of forecast comparisons should be conducted, especially for later initial times when the analyzed wind fields have attained their steady values of RMS fit with observations (say, not before 2/20/79, 00Z).

The height bias curves in Fig. 11 reveal two major trends in the forecast for FGGE III-A and ASAP initial fields: (1) a positive bias increasing steadily in time at all levels, and (2) a faster growth of positive bias in the ASAP initialized forecast at level $\hat{\sigma}$ = .150 and above, and a faster growth of the positive bias in the FGGE III-A initialized forecast at level $\hat{\sigma}$ = .375 and below after 12h and at level $\hat{\sigma}$ = .250 and below after 24h. Particularly striking is the widening of the gap between the two curves at $\hat{\sigma}$ = .100 and .050. This is primarily due to the original significantly large positive biases at these levels in the initial analysis for ASAP, and the large negative bias in the FGGE III-A initial analysis at $\hat{\sigma}$ = .050. The forecast model appears to take these large initial differences and increase them even more during the course of the forecast. This widening at these uppermost levels is due primarily to the extreme growth of the ASAP initialized positive bias. A comparison of Figs. 5 and 11 for the ANL (ASAP) curves would indicate that much of the growth of the positive bias at the $\hat{\sigma}$ = .050 level in the assimilated analyses (Fig. 5) must be due to the characteristic of the GSM to create a strong positive bias at this level, as opposed to the model used to assimilate the FGGE III-A analysis which left a modest, fairly constant negative bias at this level.

The wind component bias curves (Figs. 12 and 13) are similar to the vector wind RMS curves (Fig. 10) in that they retain their relationship with each other quite well, especially after 12h. Looking first at the u component bias, we see in both curves a tendency toward positive bias in the lower layers (with ASAP based forecast being more positive) and toward negative bias in the tropospheric extratropical jet and levels immediately above it (with FGGE III-A based forecast being more negative). The extremely high positive bias at the uppermost layer for FGGE III-A based forecast is present in the initial analysis and is continued in the model forecast. It is due to assigning the FGGE III-A analysis 50mb winds to the σ = 0.21 (~21mb) level, which in the case of the zonal wind would lead

to an overestimate as is evidenced by the positive bias. This direct
assignment was used in lieu of extrapolation, because 50mb is the highest
level carried in the FGGE III-A analysis fields. Interestingly, the low
layer positive bias, high layer negative bias is also present in the
meridional component forecast (Fig. 13). Here, however, the values of bias
between the forecasts are more similar, especially at 48h. The FGGE III-A
based forecast does exhibit a tendency toward larger negative bias just
below the tropospheric extratropical jet level (in σ layers .436 - .275).

B. Humidity Analyses

For the univariate relative humidity analysis, fit of analyses to
observations becomes somewhat more important since only humidity data are
involved. In this case, the RMS fits are very sensitive to the observation
error levels assigned to each observation type. This is illustrated in
Figs. 14 and 15, which show the fit of the ASAP analysis and forecast fields
to the basis observations for moisture option 1 (rawinsonde humidity only
used in the analysis). Not surprisingly, the use of 5 percent OESD for
rawinsonde humidity observations results in a closer fit with those
observations than does the use of 20 percent as in the F3A for all layers.
The ANL curves show lower RMS differences and biases and indicate no
apparent drift away from observations. The sawtooth configuration of the
GSM bias plot for σ_1 appears to have a diurnal character to it, while
the highly irregular bias curves at σ_7 are probably due primarily to
fewer comparison observations for that layer.

Fig. 16 shows the distribution of checked rawinsonde observations
summed over 10° latitude bands and over the ten 00Z, 12Z observation times
during the five day period. Clearly, the first guess remains relatively
uncorrected south of about 50° south latitude, with the maximum corrections
in conventional OI relative humidity analyses occurring in lower
tropospheric levels in Northern Hemisphere midlatitudes. Fig. 17(a-c) shows
the zonal, time average cross section of (a) observed relative humidity
using the checked observations whose distribution is depicted in Fig. 16,
(b) the analyzed (moisture option 1) relative humidity resulting from the ASAP
analyses averaged over all 00Z, 12Z times during the five day assimilation,
and (c) the results of subtracting plot (a) from plot (b); i.e., the
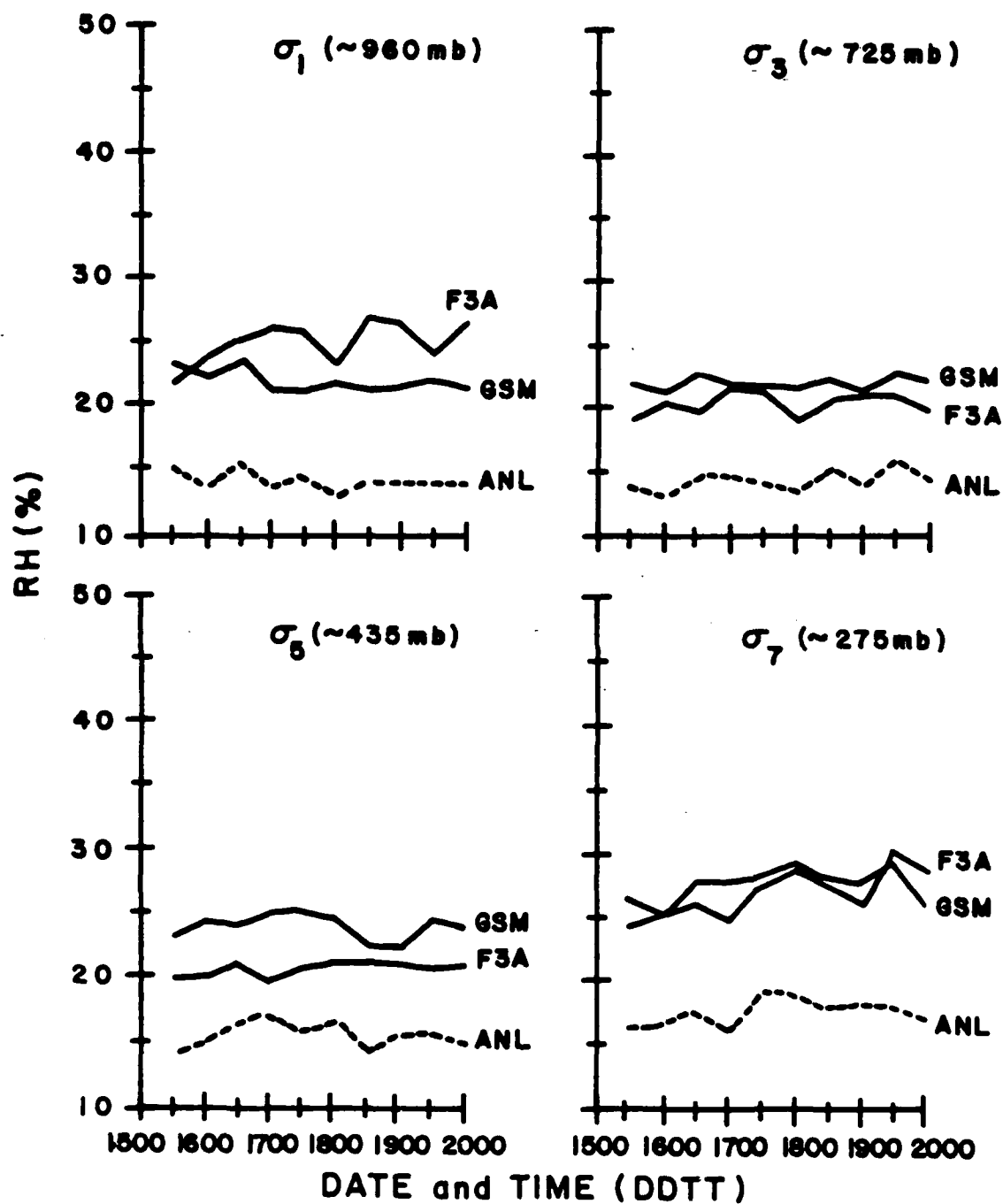
Fig. 14 RMS Differences on σ Layers between Relative Humidity Fields and Basis Observations
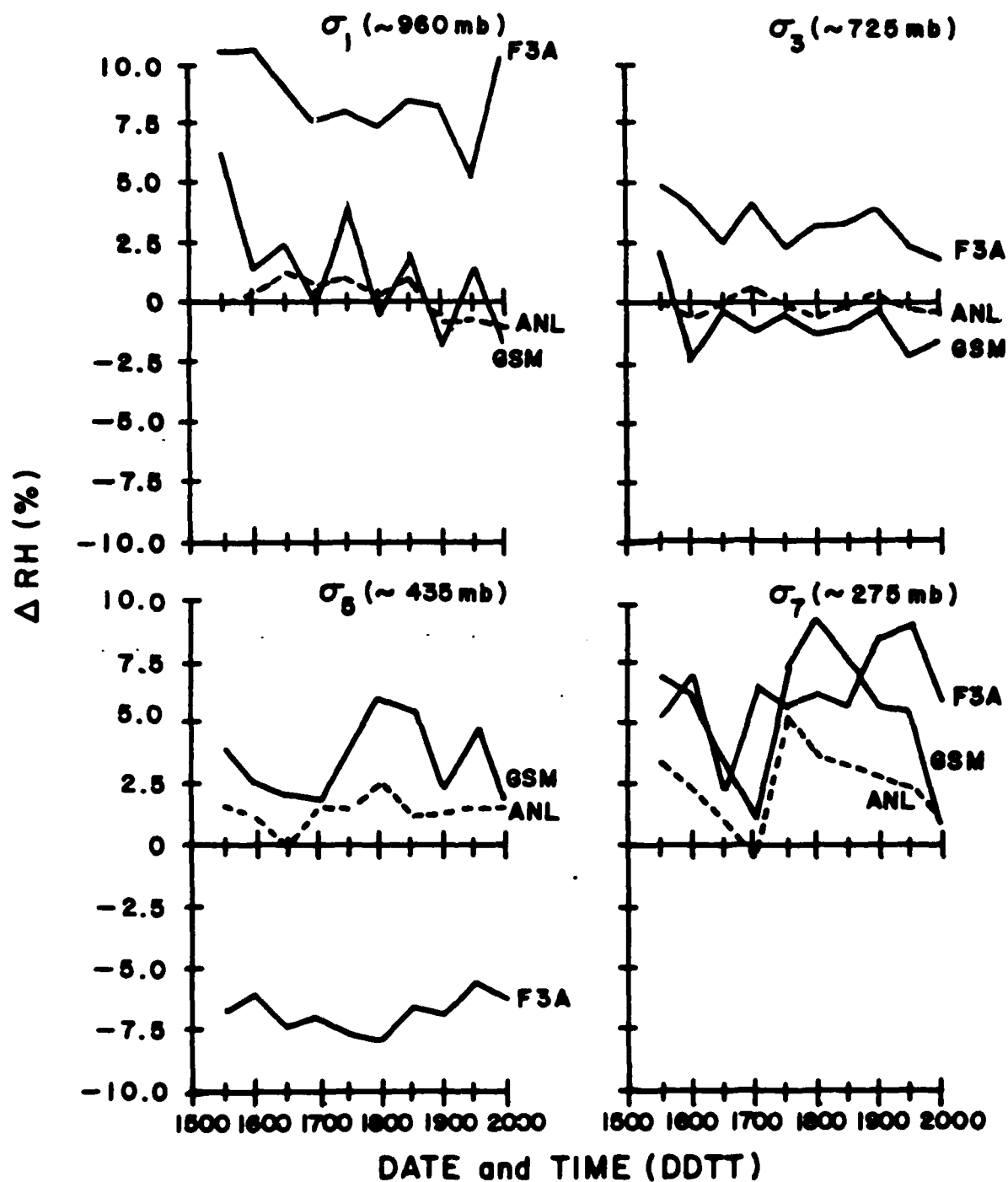
Fig. 15 Field-Observation Bias for σ Layer Relative Humidity (Basis Observations)
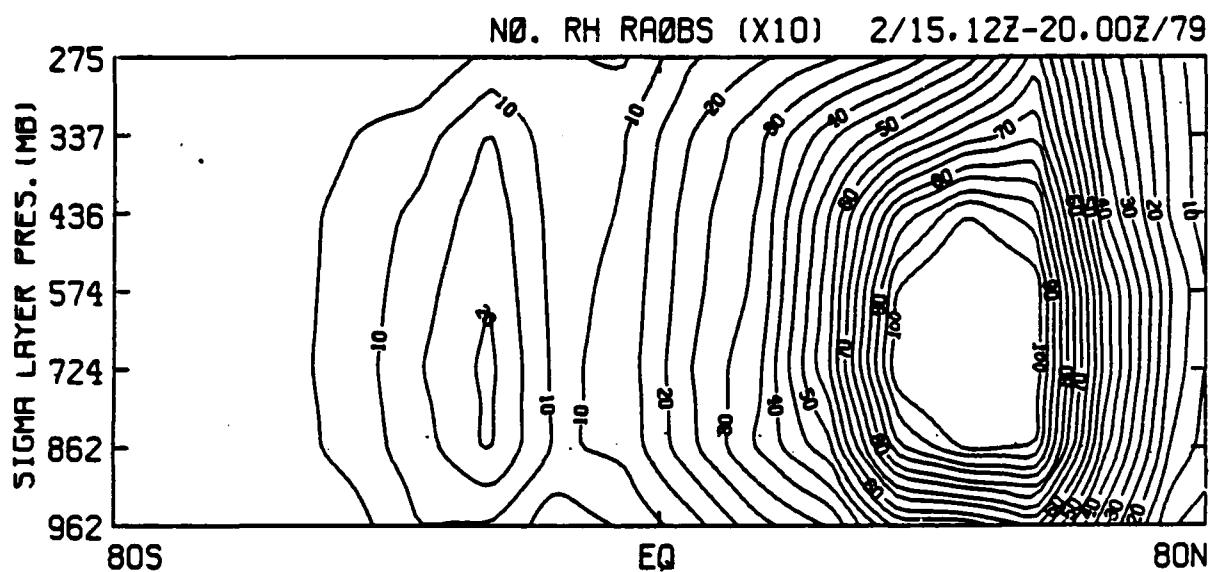
Fig. 16   Total Number (X10) of σ Layer Rawinsonde Values of Relative
          Humidity Summed Over 10° Latitude Bands and the Ten 00,12Z Time
          Periods of the Data Assimilation Experiment. These Are the
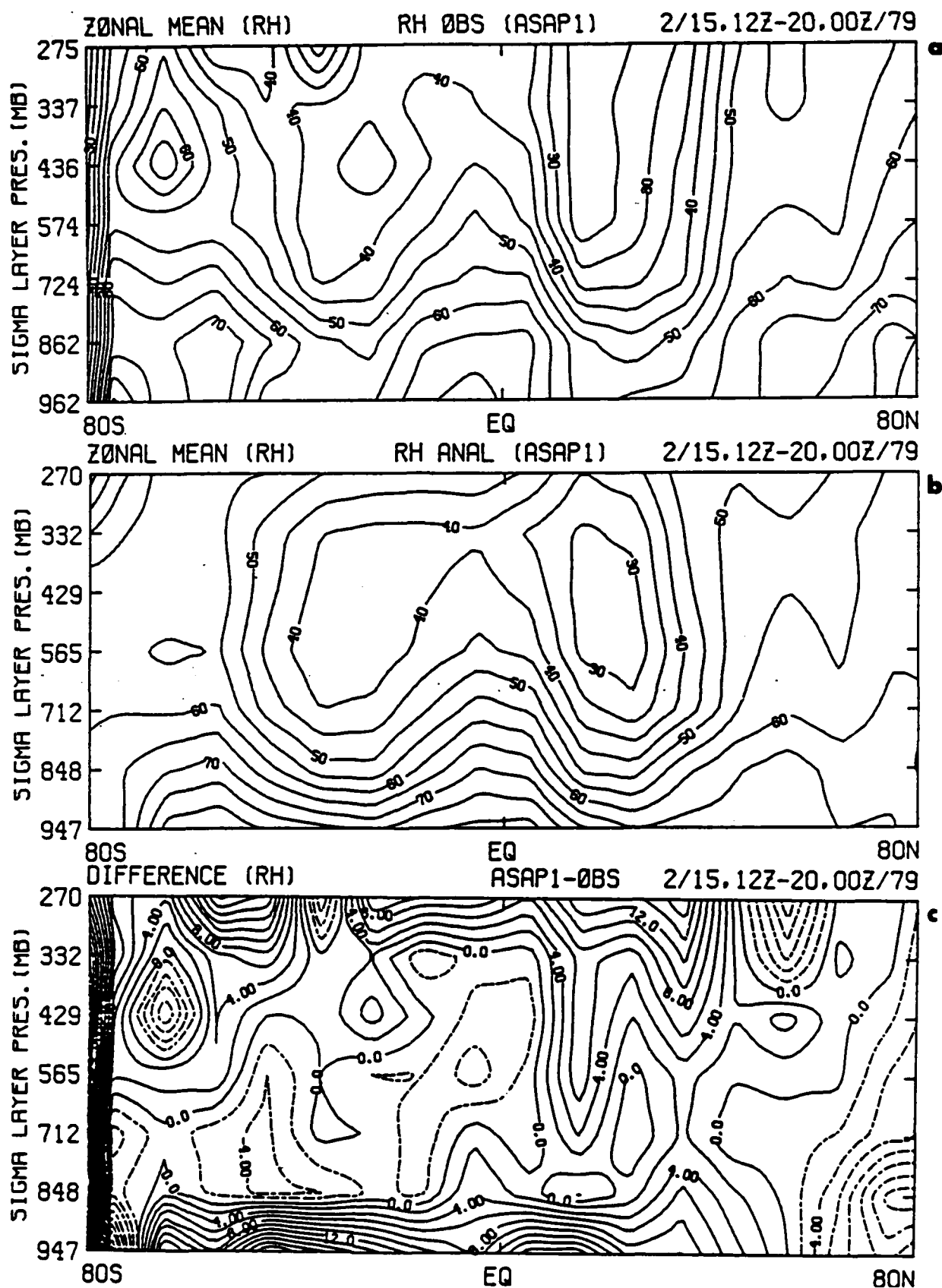   Checked Observations Making Up the Set of Basis Observations.

Fig. 17(a-c)   Zonal, Time Average Relative Humidity for (a) Basis
Observations, (b) ASAP (Opt. 1) Analyses, and (c) Difference
between (b) and (a). Contour Interval for (a), (b) is 5%,
for (c), 2%. Dashed Contours Indicate Negative Values.

differences in the zonal, time averages of observed and analyzed σ layer relative humidities. The σ layer pressures indicated on plot (a) are the nominal ($p_* = 1000$) layer pressures, whereas those shown in plots (b) and (c) are based on the ASAP weekly averaged surface pressure. The dense contour intervals on plots (a) and (c) are the result of very few observations lying in the latitude band 90°S - 80°S. The difference plot (c) reveals, in a zonal, time average sense (ignoring the left-most quarter of the plot), a generally good fit of the observations especially between the 848 mb and 332 mb levels. There is a tendency for the analyses to be too moist at the lowest layer for most latitudes, especially those dominated by oceans. This is probably a result of the forecast model in that moisture fluxes from the ocean surfaces are not being mixed into upper levels by the rather simplistic boundary layer parameterization. The moist bias also appears at most latitudes for the highest (270 mb) layer, though the reason for this is not as clear. However, with the exception of under-analyzing the dryness of the descending branch of the Hadley circulation at about 15°N, the fit at other layers is quite satisfactory. A comparison of Fig. 17(c) with the corresponding difference cross section for FGGE III-A analyses-minus-observations (Fig. 18) reveals once again the effect of lowering the OESD value on the analysis fit to observations. Part of the increased moist bias in the FGGE III-A difference cross section is due to the necessity of extrapolating humidity from the highest analysis level (300 mb) to the σ_7 layer pressure (usually less than 300 mb). However, through the lower layers a pronounced moist bias is evident, whereas at σ layer pressures 565, 430, and 332 mb a definite dry bias in the analysis is indicated. These results confirm in a zonal, time average sense what Fig. 15 showed in a synoptic, point-by-point verification. The F3A biases are not present in the ASAP analyses, probably largely due to the lower error assigned to the observations.

It is in the data sparse regions as indicated in Fig. 16 that the use of alternative forms of moisture information would be expected to have their greatest effect. This can be illustrated in one way by comparing the plots of observation locations for moisture option 2 (rawinsonde, SWO, and 3DN relative humidities used in the analysis) as shown in Fig. 19(a-c). These figures show the distribution of (a) unchecked observations, (b) checked observations, and (c) observations actually used at least once in the

82
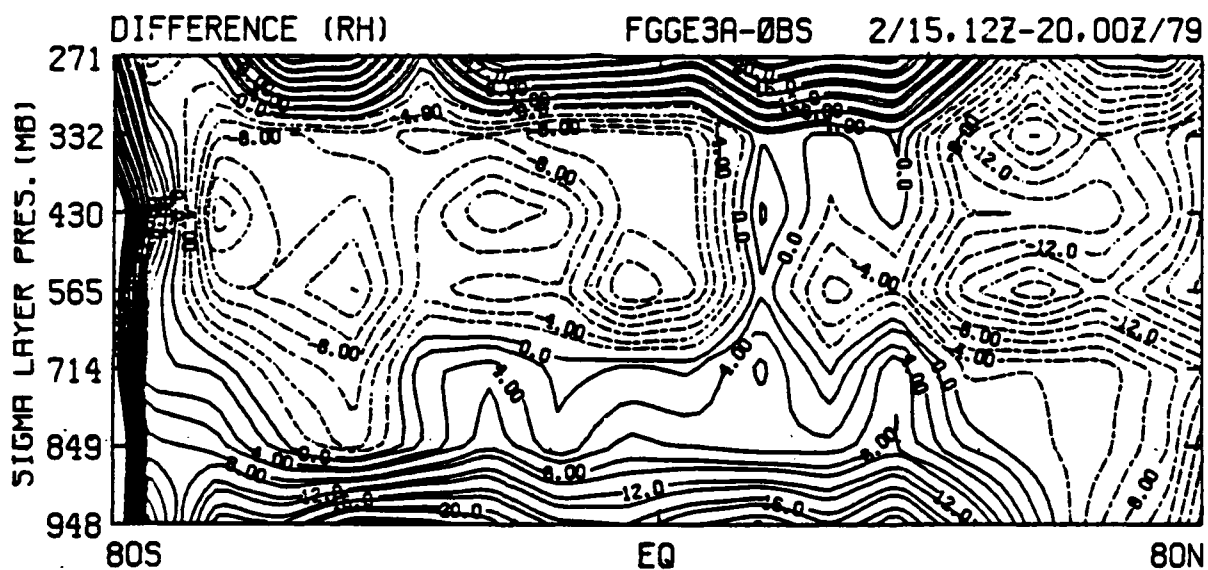
Fig. 18 Difference between Zonal, Time Average FGGE III-A Relative Humidity
Analyses and Zonal, Time Average Relative Humidity Basis
Observations. Contour Interval is 2%, and Dashed Contours
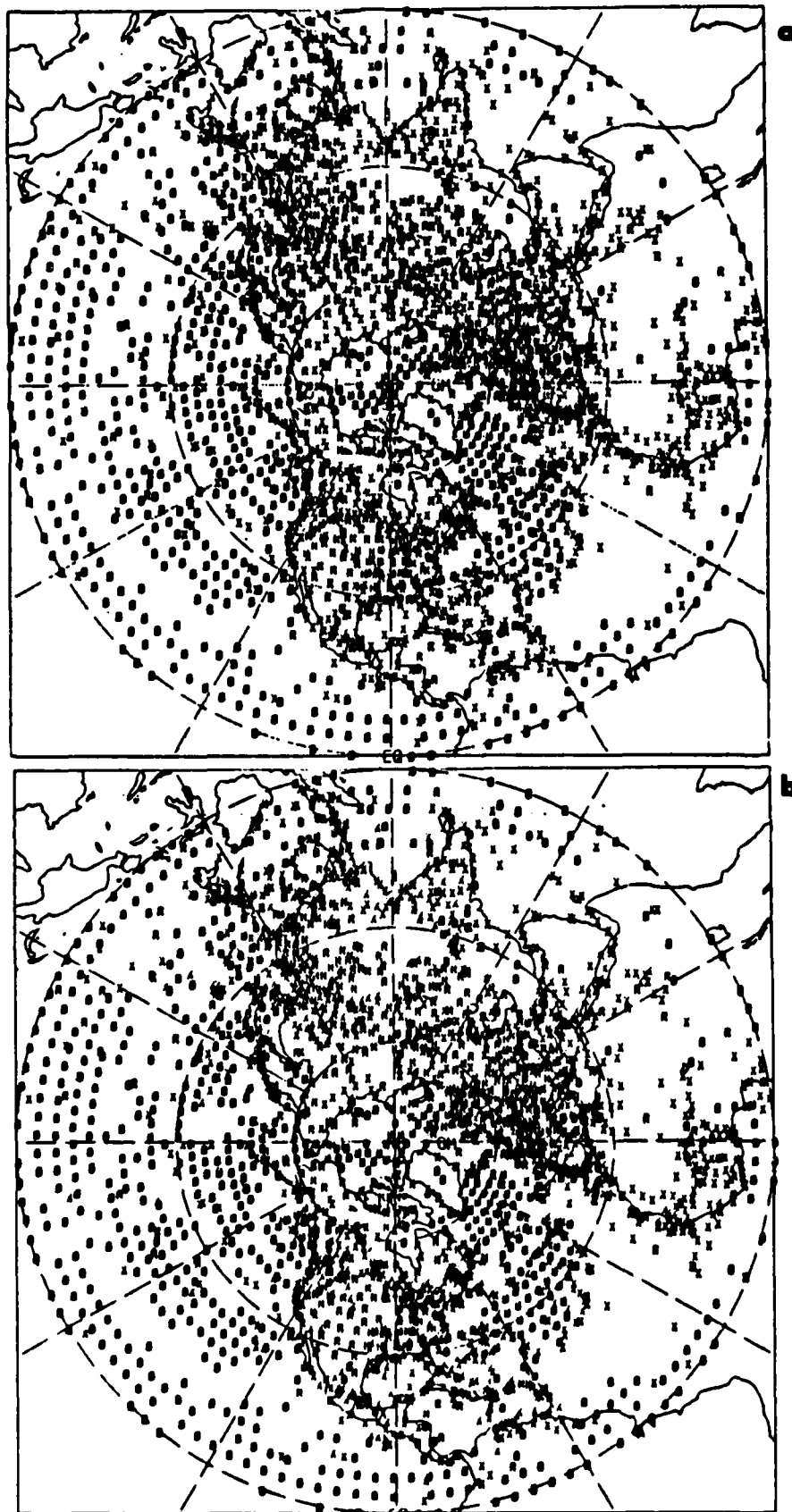Indicate Negative Values.

Fig. 19(a,b) Location of (a) Unchecked and (b) Checked Relative Humidity
Observations for ASAP (Opt. 2) Analysis of 2/15/79, 12Z at
σ_2 (~860 mb). R = Rawinsonde, X = Surface Weather
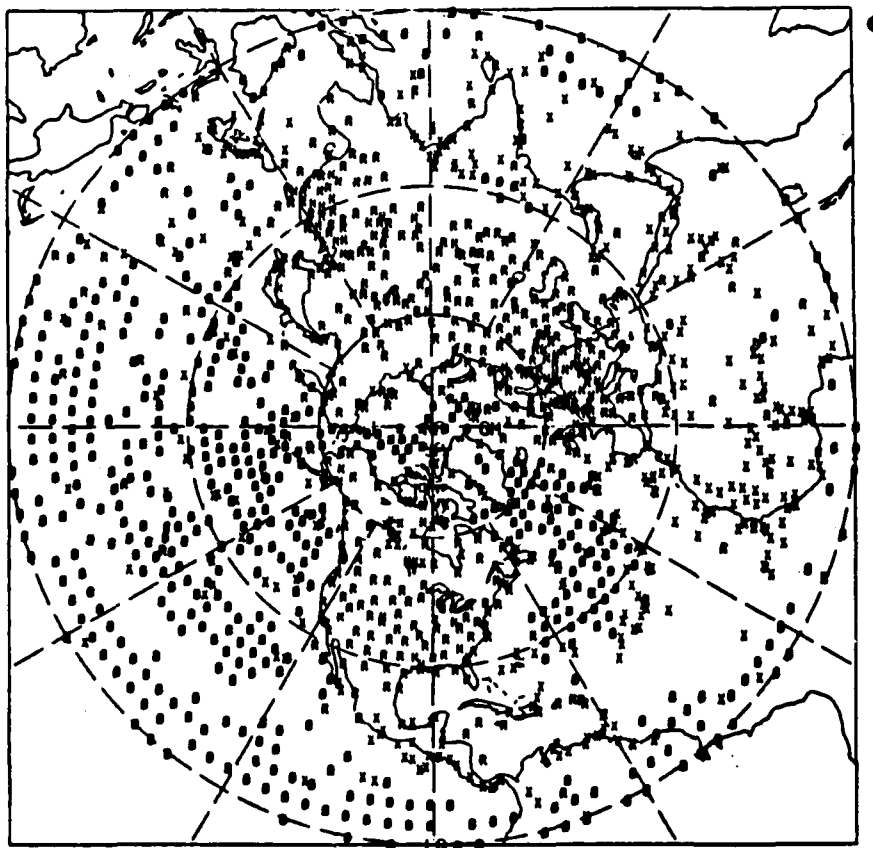Observation Inferred, ● = 3DNEPH Inferred.

Fig. 19c Location of Relative Humidity Observations Actually Used in
2/15/79, 12Z ASAP Analysis. Symbols Are Same As in Fig. 17(a,b).

analysis for 2/15/79 12Z at σ_2 (~860 mb). Observations present in (a) but missing from (b) were removed by the buddy and gross checks. By comparing plots (b) and (c), one can see the dominance of the rawinsonde observations being selected over alternative types, even though the rawinsonde observations may be many fewer in number and more scattered in an area. For example, over India a predominance of SWO humidities (and to a lesser extent, 3DN humidities) exists in the checked data, but the analysis preferred to use the fewer and more scattered rawinsonde observations for analysis points in that region. Alternative sources are all but excluded from use over rawinsonde dense regions. This is due to the much lower observational error for rawinsondes which favored their selection and resulted in higher weights. Thus, major differences between option 1 and option 2 humidity analyses should exist only in the rawinsonde-sparse regions, such as 0°-30°N and 60°-90°N. It was thought that by comparing analyses against zonal, time averages of observations that the data scarcity in those regions could be overcome to allow for reasonable comparisons. Plots of zonal, time average option 2 analyses and their difference from zonal, time average basis observations (i.e., rawinsondes) are given in Fig. 20(a-b). Indeed, we see the greatest differences between Figs. 17(c) and 20(b) south of 30°N, where in the mid-layers (848 mb - 429 mb) the prominent differences are two locations of greater moist bias in the Hadley branch (around 15°N) and centered at the 712 mb layer at 20°-30° S. The option 2 analyses appear to be significantly more moist at these layers and levels, and because of the conventional data sparsity in these regions the differences must be due to the use of the alternative moisture sources. However, note that a positive effect of using the alternative moisture sources is that the moist bias is lessened at the lowest and highest layers at most latitudes. It appears that the use of the alternative data in the OI analyses resulted in better overall analyses at the lowest and highest layers and somewhat poorer analyses in the mid-layers. Since the differences are most evident in conventional data sparse regions, the additional moisture information appears to be an improvement to the first guess at the bottom and top layers, and leads to a worsening of the first guess in the mid-layers. These conclusions must be tempered somewhat by the availabilty of rawinsonde comparison data as shown in Fig. 16, and by the limited sample (10 cycles) of the assimilation period.
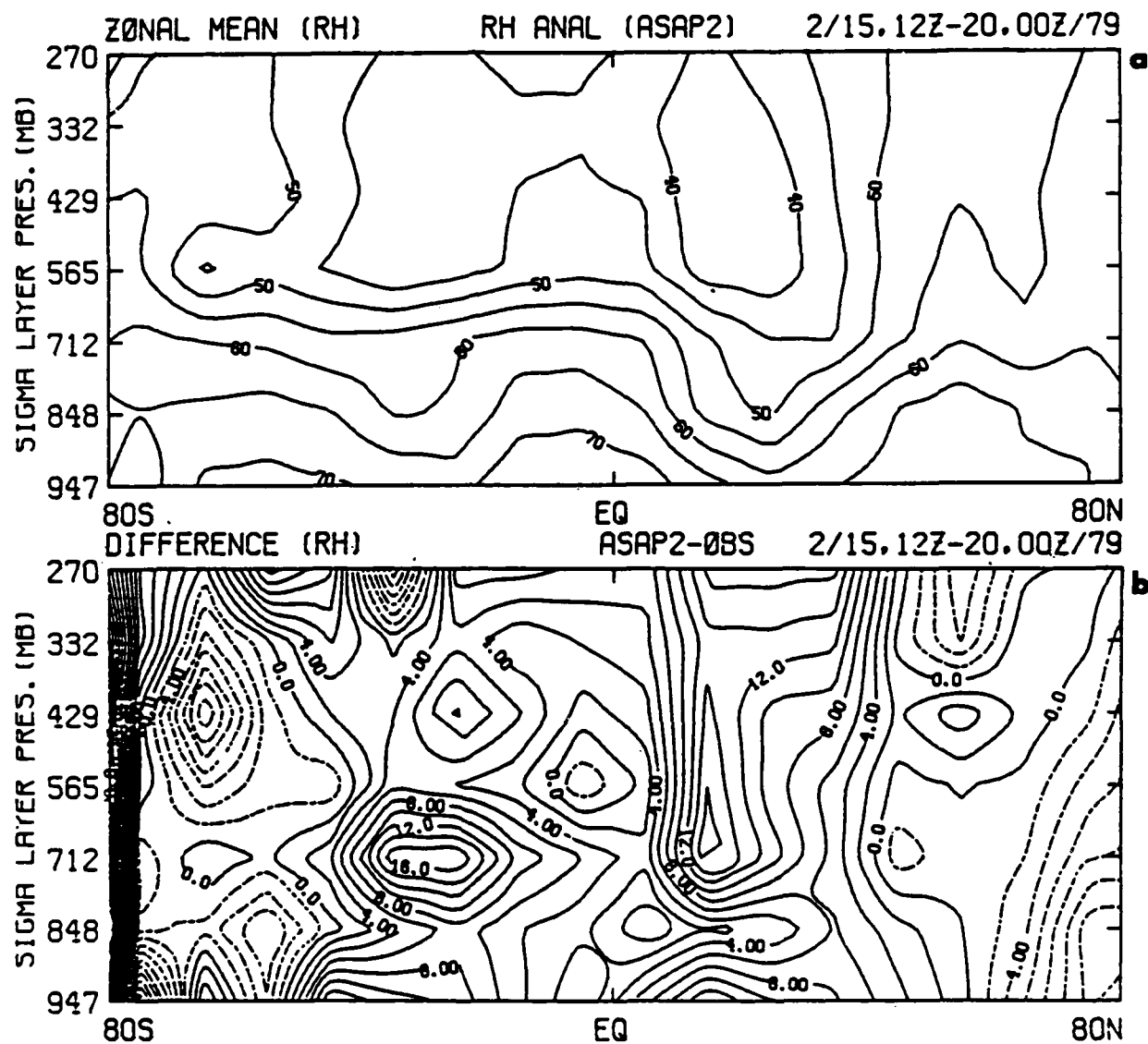
Fig. 20(a,b)   Zonal, Time Average Relative Humidity for (a) ASAP (Opt. 2)
Analyses and (b) Difference between (a) and Basis
Observations (Fig. 17(a)).   Contour Interval for (a) is 5%,
for (b) is 2%.   Dashed Contours Indicate Negative Values.

In an attempt to assess the effect of the alternative relative humidity information on an individual analysis, Figs. 21-23 were prepared. Fig. 21 shows the locations for the Northern Hemisphere of the observations (a) which survived the gross and buddy checks, and (b) which are actually used in the analysis for 2/17/79 12Z for σ_2 (~860 mb). Notice once again the distinct preference for the use of rawinsonde information in the analysis. This results in rawinsonde rich regions, such as North America, Europe, and northern Asia, which are left exclusively with rawinsonde relative humidities with which to perform the analysis. Therefore, we would expect the effect of the corrections on the first guess from moisture options 1 and 2 to look quite similar over these regions. This is confirmed by comparing Fig. 22(a) (analysis corrections for option 1) with Fig. 22(b) (analysis corrections for option 2). Note the relatively similar analysis corrections over the three aforementioned rawinsonde rich areas. Fig. 23(a,b), which shows the corresponding analysis errors for the two moisture options, indicates by their similarly low values of around 8 percent in these regions that the low OESD values for rawinsondes have led to low analysis errors throughout the assimilation period for both moisture options. As expected, the primary differences between the two sets of analysis corrections should occur in the rawinsonde sparse areas. For example, consider the region bounded by latitudes 30°N and 60°N and longitudes 180°E and 240°E. This region of the northern Pacific had primarily rawinsondes used in the analysis on its northern and eastern edges, but predominantly SWO and 3DN pseudo-observations in the rest of the area [see Fig. 21(b)]. Notice that in Fig. 22(b) (moisture option 2) the analysis corrections are smaller for the predominantly SWO, 3DN part of the region than for the nearby rawinsonde rich regions. Because of the complete lack of information in this area for moisture option 1, the analysis corrections are essentially zero in Fig. 22(a). As expected by the difference in assigned OESD's for the rawinsonde and alternative relative humidity values, the corrections to the first guess in regions dominated by the rawinsonde are significantly different from the corrections in alternative data rich regions, with the corrections in the rawinsonde dominated areas being generally larger. A better measure of the relative effect is depicted in Fig. 23 (a,b). Here it is seen that whereas in rawinsonde rich areas the analysis error is similar for the two analyses, in
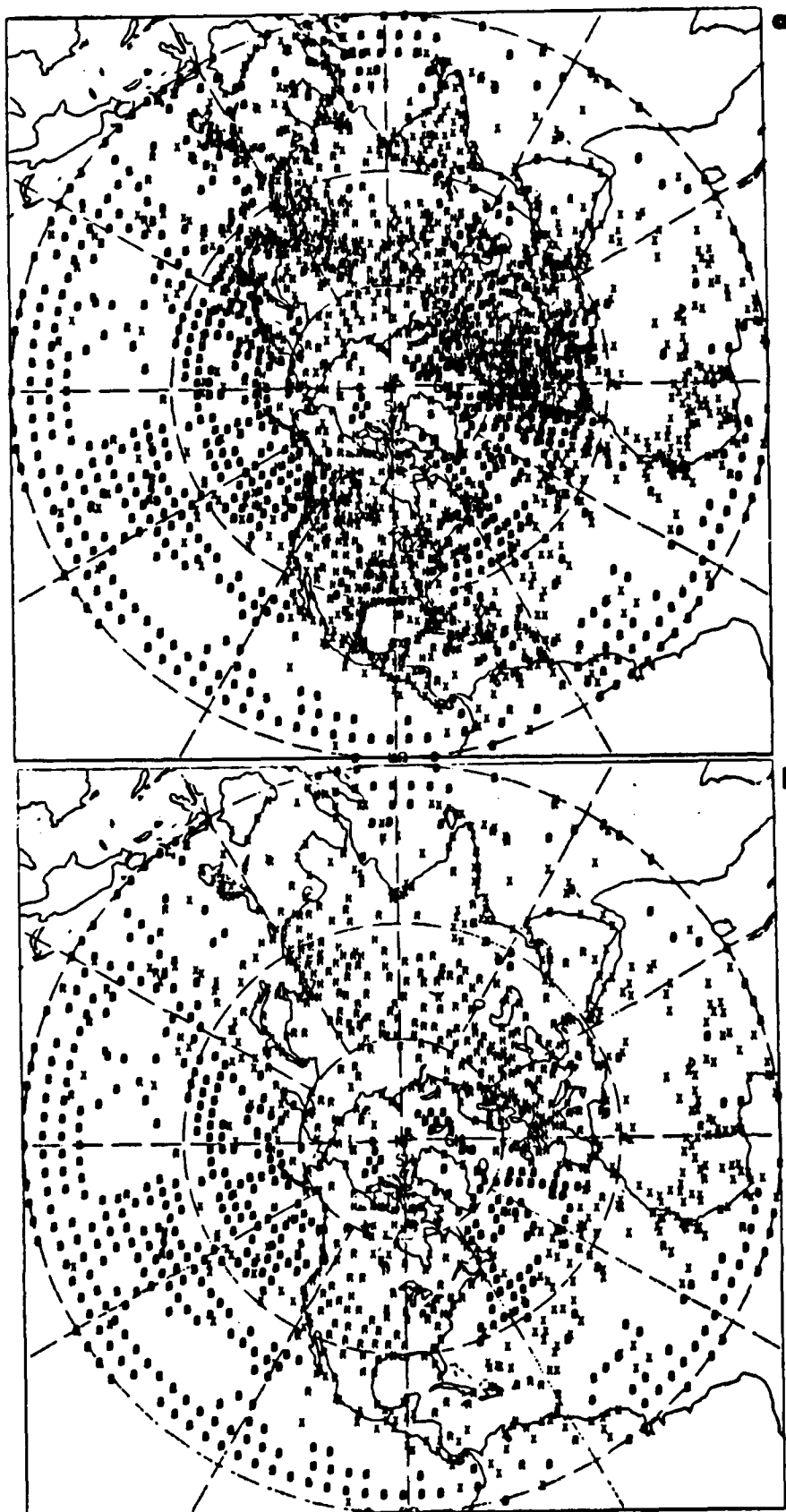
Fig. 21(a,b)   Location of (a) Checked and (b) Used Relative Humidity
Observations for ASAP (Opt. 2) Analysis of 2/17/79, 12Z at
σ_2 (~860 mb).   R = Rawinsonde, X = Surface Weather
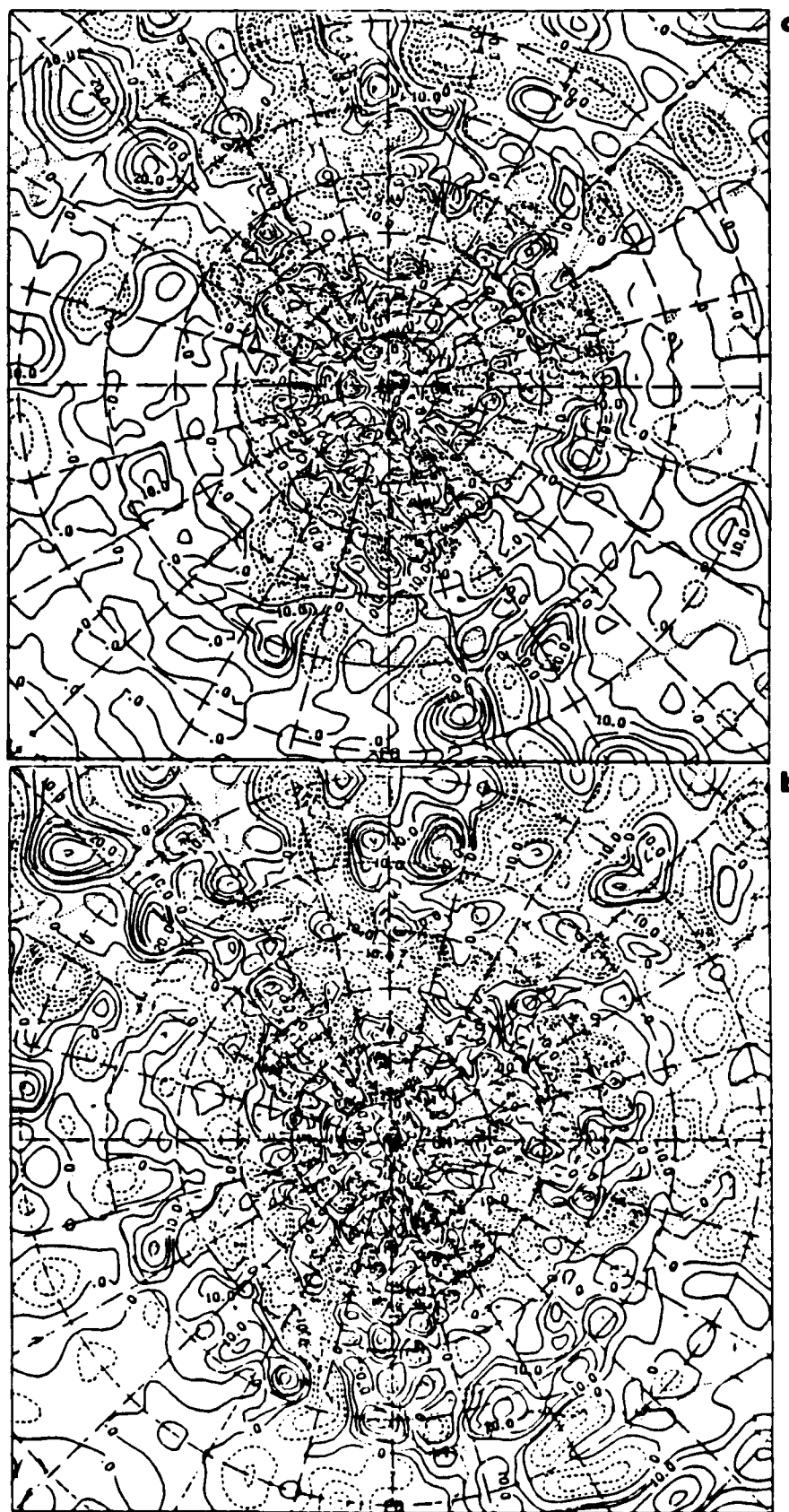Observation Inferred, ● = 3DNEPH Inferred.

Fig. 22(a,b) Analysis Corrections for ASAP Relative Humidity Analyses (a) Opt. 1 and (b) Opt. 2 for 2/17/79, 12Z at σ_2 (~860 mb). Contour Interval is 5%. Dashed Contours Indicate Negative Corrections.
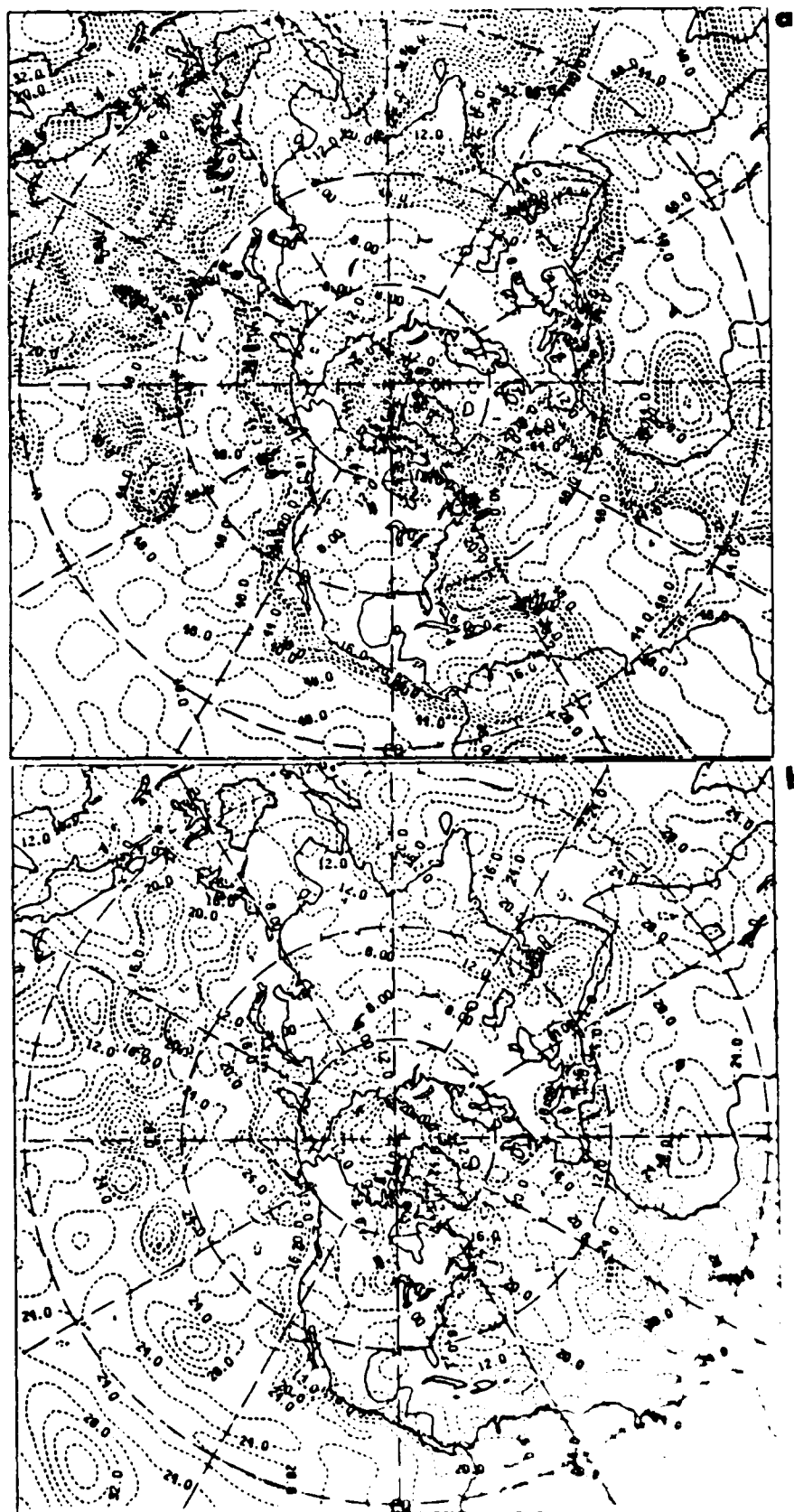
Fig. 23(a,b) Analysis Errors for ASAP Relative Humidity Analyses (a) Opt.
1 and (b) Opt. 2 for 2/17/79, 12Z at σ₂

91

MICROCOPY RESOLUTION TEST CHART
NATIONAL BUREAU OF STANDARDS-1963-A

rawinsonde sparse but alternative data rich regions the analysis error is
noticeably reduced below the maximum allowed (48 percent), which occurs in
all of the rawinsonde void regions remaining essentially uncorrected through
the assimilation. Thus, it appears that the use of the alternative
information leads to reduced analysis errors over no analysis, but that the
corrections in areas dominated by alternative information are generally
smaller than in rawinsonde rich areas. The smaller corrections are to be
expected because the analysis error in alternative rich regions (typically
20-24 percent) is larger than in rawinsonde rich regions (8 percent); thus
any alternative observations would have corresponding less weight in the
analysis. Larger OESD's lead to less weight for the observations (and thus
generally a smaller total correction), which in turn leads to higher
analysis errors. Notice in Fig. 23(b) that in all of the alternative
humidity rich areas, the analysis error (and thus the FESD) is maintained at
a level approximating the OESD for 850 mb SWO's and 3DN's (see Table 13).
Comparing the original values of relative humidity FESD used at the
beginning of the assimilation (see Table 4), it appears that the alternative
sources of humidity information are effective in holding the FESD at a
relatively level value through the assimilation for areas where they are
relatively plentiful.

Because the 3DNEPH cloud amounts represent an analysis themselves, it
is not necessary to perform an additional analysis to move them to the grid
locations. The horizontally averaged cloud amount are available on a 50 km
(quarter-mesh) grid, and as such very little error is introduced in simply
interpolating bilinearly the gridded cloud amounts (converted to cos
[(π/100) · % cloud amount]) to the analysis points at each σ layer.
This was done for the cloudy regions in moisture option 3, and the relative
humidity inferred from these cloudy analysis point cloud amounts was used to
directly replace the first guess relative humidity at each analysis time.
At non-cloudy analysis points, an OI analysis using rawinsonde relative
humidity only was performed if such data were available nearby, otherwise
the first guess value was maintained. Table 16 gives the percentage of
analysis points through the five day period which fell into each of the
three categories. Since the 3DN replacement occurred at cloudy analysis
points only, the 3DN percentages are an estimate of global cloud cover at

Table 16. Percent of Analysis Points in ASAP3

(3DN) Replacement by 3DN Values Occurred, (OI) Rawinsonde OI Occurred, (FG) First Guess Was Maintained

MB	3DN	OI	FG
275	22	49	29
337	22	50	28
436	18	54	28
574	31	46	23
724	51	33	16
862	51	36	13
962	48	38	14

each σ layer. Fig. 24(a-c) shows these same percentages as zonal averages for the five day period. According to Fig. 24(a), cloud cover is generally a maximum at the lower levels through most of the summer hemisphere, and at the 724 mb layer in the higher latitudes of the winter hemisphere. At the 436 mb layer and above, cloud cover is for the most part less than 30 percent, and it is at these layers and in the descending Hadley branch that conventional OI reaches its maximum values (Fig. 24b). Maintenance of the first guess exceeds 50 percent only in the highest three layers and high latitudes of the Southern Hemisphere.

Fig. 25(a,b) shows the zonal, time average of the five day option 3 analysis and its difference from observations respectively. Of immediate interest is the comparison of the analysis-observation differences for moisture option 2 (Fig. 20(b)) and 3 (Fig. 25(b)). Notice that the two moist anomalies in the ASAP2-OBS figure are reduced dramatically in the ASAP3-OBS figure. The Southern Hemisphere anomaly, centered at the 712 mb layer at 30°S-40°S, is in an area of about 50 percent replacement by the 3DN analysis point values and about 30 percent conventionally analyzed observation sites in the zonal mean. Thus, it appears that the replacement 3DN values had an improving effect on the humidity analysis at this locale. The other ASAP2-OBS anomaly, in the descending Hadley branch, is in a region of about 20 percent 3DN replacement and 60 percent conventional OI. The anomaly is reduced by about half in magnitude, and this must be due primarily to the conventional OI without the use of the alternative data. This would reinforce the earlier idea that this anomaly is a result of the worsening of the analysis by the use of the alternative information used in the OI mode. It is important in the case of the 3DN to make the distinction between use as pseudo-observations in the OI as opposed to its use in a direct replacement of the first guess value. In the former case, it takes the form of a correction whose weight is roughly equal to the first guess field it seeks to correct. In the replacement case, it completely replaces the first guess, acting as having a weight of 1.0 vs. the first guess weight of 0.0. Thus, in cloudy regions the analysis field is completely dominated by the features of relative humidity inferred from cloud amounts. In such areas (indicated by over 50 percent 3DN replacement in Fig. 25(a), such as
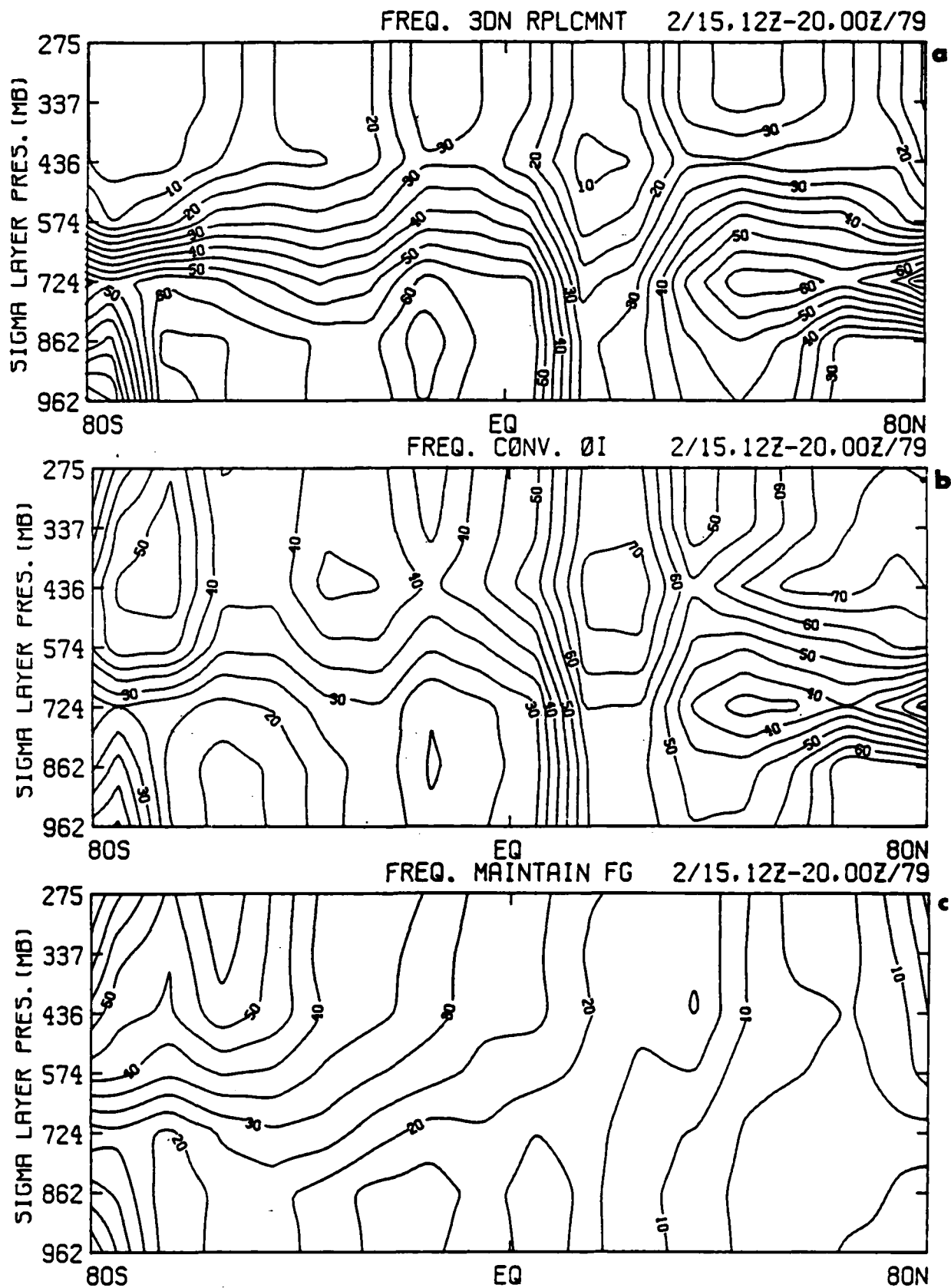
Fig. 24(a-c)   Zonal Averages of Percent Frequency of (a) 3DNEPH Replacement, (b) Conventional OI Using Rawinsonde Observations, and (c) Maintaining the First Guess during the Ten 00,12Z Cycles of the ASAP (Opt. 3) Relative Humidity Assimilation Experiment.
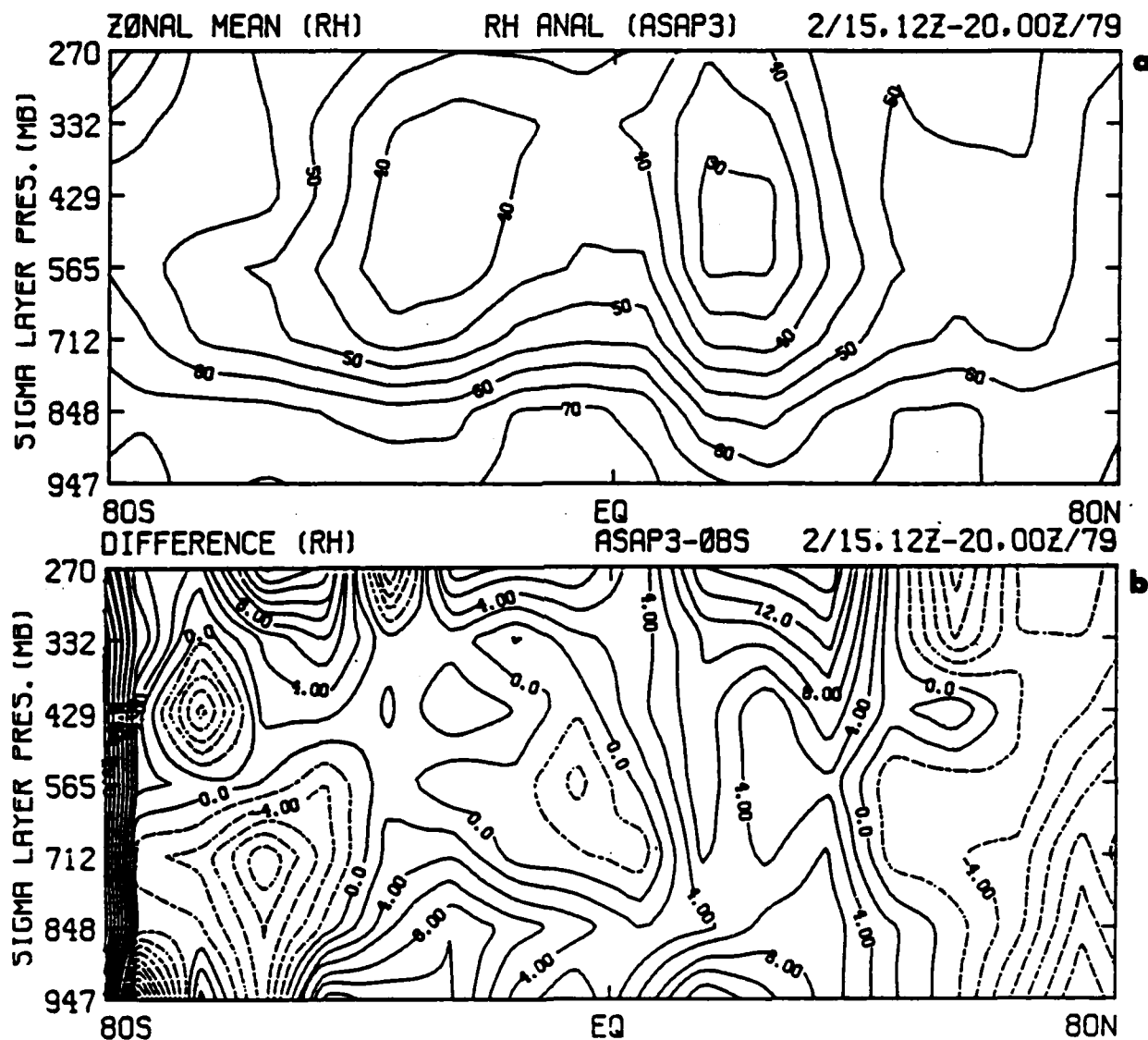
Fig. 25(a,b)   Zonal, Time Average Relative Humidity for (a) ASAP (Opt. 3)
Analyses and (b) Difference between (a) and Basis Observations
(Fig. 17(a)).   Contour Interval for (a) is 5%, for (b) is 2%.
Dashed Contours Indicate Negative Values.

at σ_3 and below throughout the Southern Hemisphere and at $\sigma_2-\sigma_4$ in the Northern Hemisphere extratropics), the 3DN replacement performs quite favorably in comparison to the option 1 analyses (Fig. 17(c)). In fact, the moist bias occurring at the lowest layer in the ASAP1-OBS figure is reduced significantly through the Southern Hemisphere. Yet, the mid-layers in the Northern Hemisphere extratropics are only slightly drier (~2 percent) in the ASAP3 analyses than in the ASAP1 analyses. Thus, it appears that the 3DN inferred humidities are contributing positively to the analysis when used in the replacement mode, even though they may not be doing so when used in conjunction with SWO inferred humidities in the OI mode. In the latter case, it could be that their relatively high assigned OESD values result in a damping of their contribution, being masked by the first guess which is considered equally as valid by the analysis procedure. Looking back at Tables 13 and 14, it is clear that if the OESD for rawinsonde relative humidities were raised to 15 percent at all levels, the OESD values for the alternative observations would drop 3-5 percent, which would give them more impact in the analysis. However, the fact that their straight replacement in the analysis appears to be making a positive contribution to the assimilation analyses would suggest that they should be used with their fullest effect, namely as replacements rather than observations for interpolation. Then it would remain to be seen if SWO observations by themselves result in an improvement of the first guess in the OI mode.

In this vein, three further experiments were conducted to examine the effects of 3DN replacement and SWO OI analysis in areas where the resulting analyses can be compared to a plentiful supply of high quality observations, namely rawinsondes. It would then be assumed that alternative information would have the same effect on the analyses in conventionally data sparse areas. Moisture option 4 involved the use of 3DN replacement in cloudy regions only (i.e, no conventional OI in non-cloudy regions). Moisture option 5 allowed no correction to the first guess anywhere during the course of the assimilation (to act as an experimental control). Moisture option 6 allowed the use of only surface weather observations in the OI, with maintenance of the first guess elsewhere. In the option 6 case, the OESD's for SWO's were reduced to a level corresponding to OESD's of 15 percent RH for rawinsondes. Thus their values at levels 1000-300 mb were assigned as

8.0, 16.0, 20.0, 19.0, 18.0, 16.0. This was done to allow them to have their fullest effect in the analysis in order to better assess their impact on the first guess.

RMS differences and bias against the basis set of rawinsonde relative humidity at 00Z, 12Z times were computed and plotted in Figs. 26 and 27. The solid curve in each plot (no humidity analysis) represents the tendency of the forecast model in its development of relative humidity vs. observed humidity. In the RMS curves, there is a clear growth of RMS difference for the "no analysis" curves, especially at σ layers 3 and above. The corresponding bias curves show a tendency of the model to generate slightly too moist a forecast at σ_1, too dry at σ_2, σ_3, and substantially too moist at $\sigma_4-\sigma_7$.

As for the ASAP4 (3DN replacement) and ASAP6 (SWO OI only), it is fair only to compare each against the "no analysis" curves, and not against each other. This is because the ASAP4 analyses represent 3DN replacment only where clouds occur, which would show no geographic preference for where comparative rawinsondes are located. Since the ASAP4 curves represent the effect of changes from the background field only in the area of comparative rawinsondes, this would represent in general only about half of the total effect of 3DN replacement globally. On the other hand, a majority of the SWO's occur in areas rich in rawinsondes, especially over certain land regions (see for example, Fig. 19(a)). Therefore, most of their effect on the analysis will be felt in areas where there are rawinsondes against which to measure their impact on the analysis.

Looking first at the RMS and bias for the 3DN replacement case, the RMS curves appear to represent an improvement to the uncorrected first guess ("no analysis" curves) at all layers except possibly σ_1, where on the whole it shows no clear improvement over the model generated humidity field. The bias curves for 3DN replacement show a lessening of the bias from the "no analysis" case at σ_1 and $\sigma_4-\sigma_7$, and an introduction of a substantial moist bias at σ_2, σ_3. At these two layers, the tendency of a model dry bias is overcompensated for by an apparently larger moist bias due to the 3DN replacement. That the 3DN replacement curves show a moist bias relative to the model generated humidity fields is somewhat surprising in light of Table 12, which shows a dry bias at all levels in the 3DN-rawinsonde collocation study using the Tibaldi method. However, the
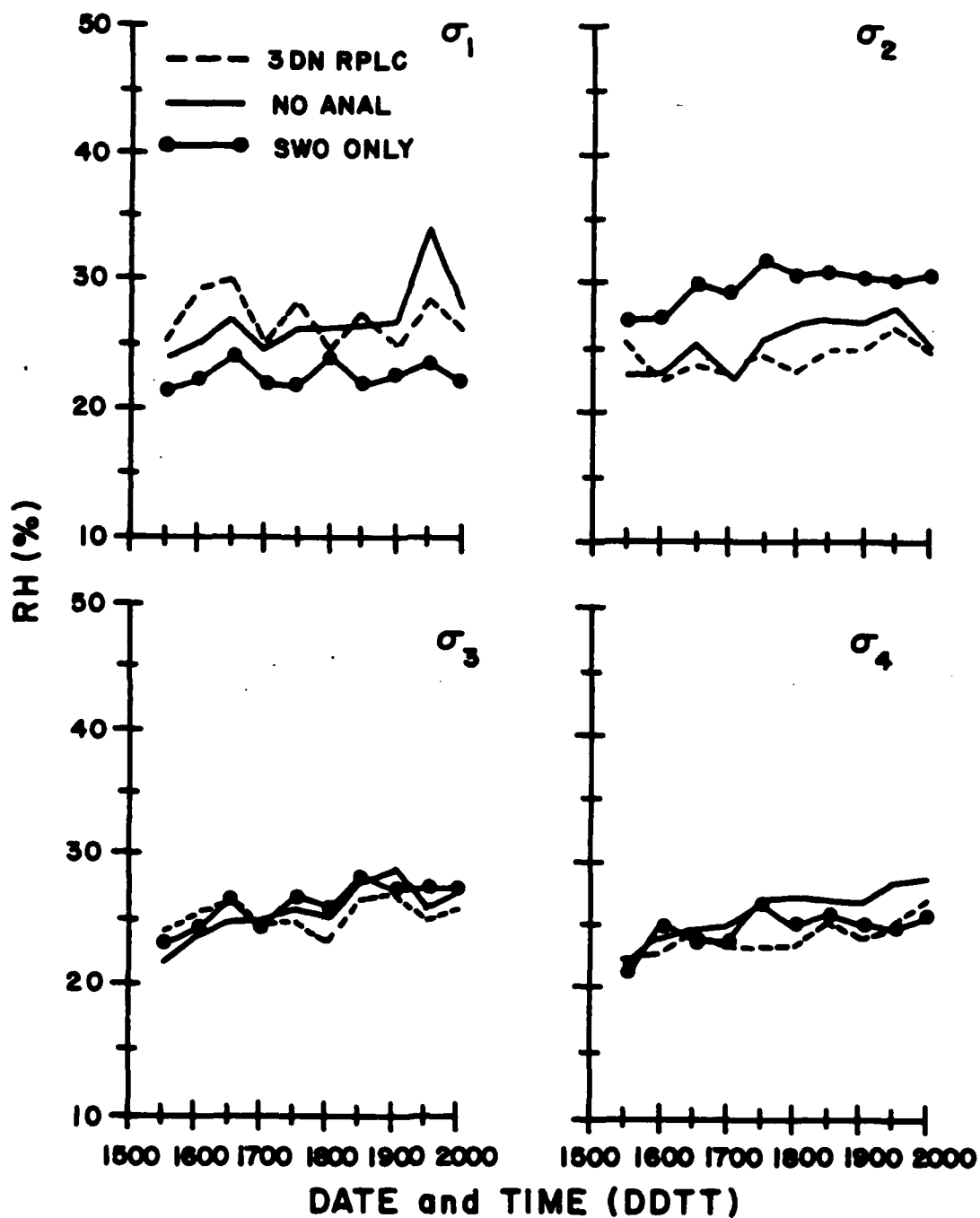
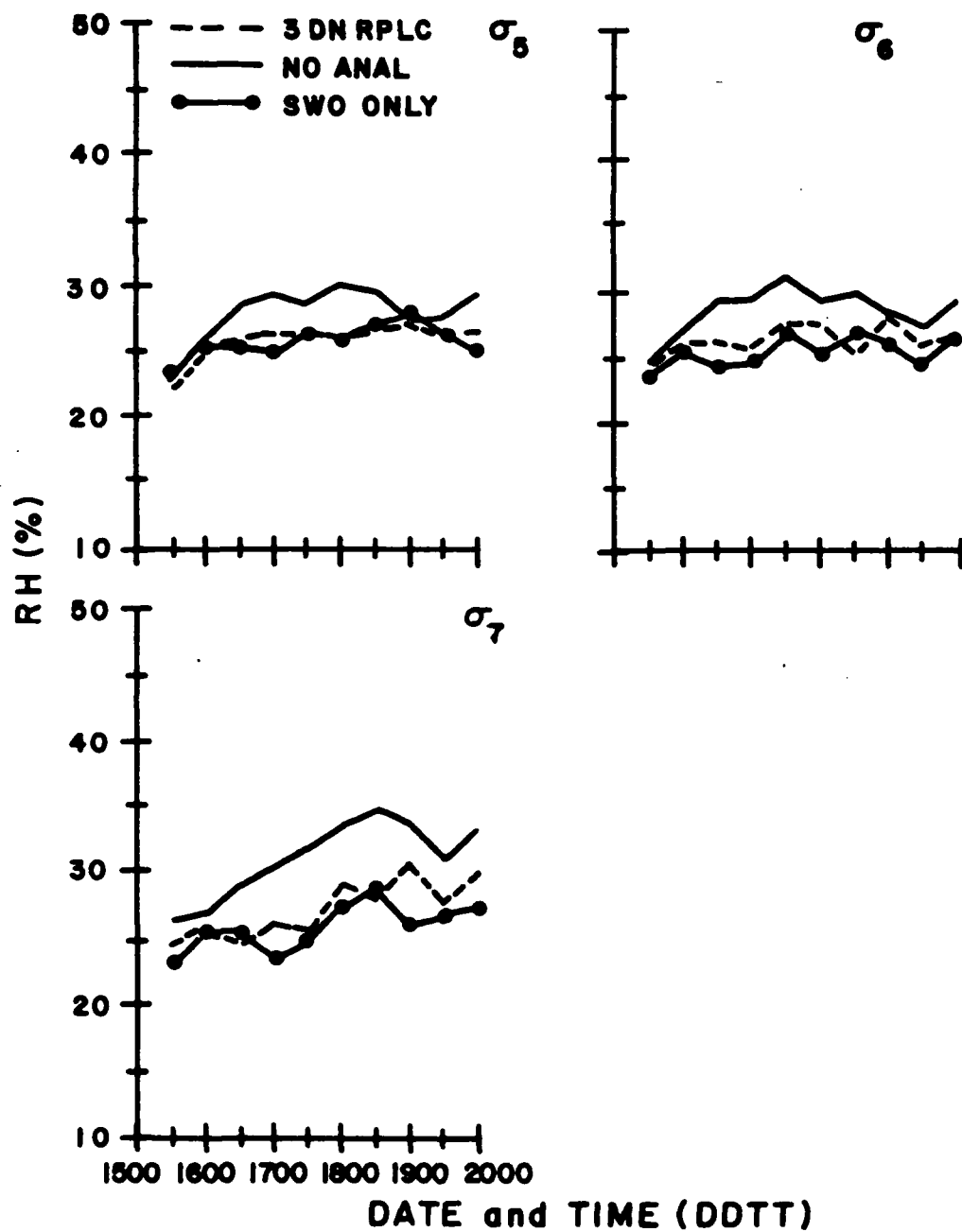Fig. 26 RMS Differences on σ Layers between Relative Humidity Fields and Basis Observations
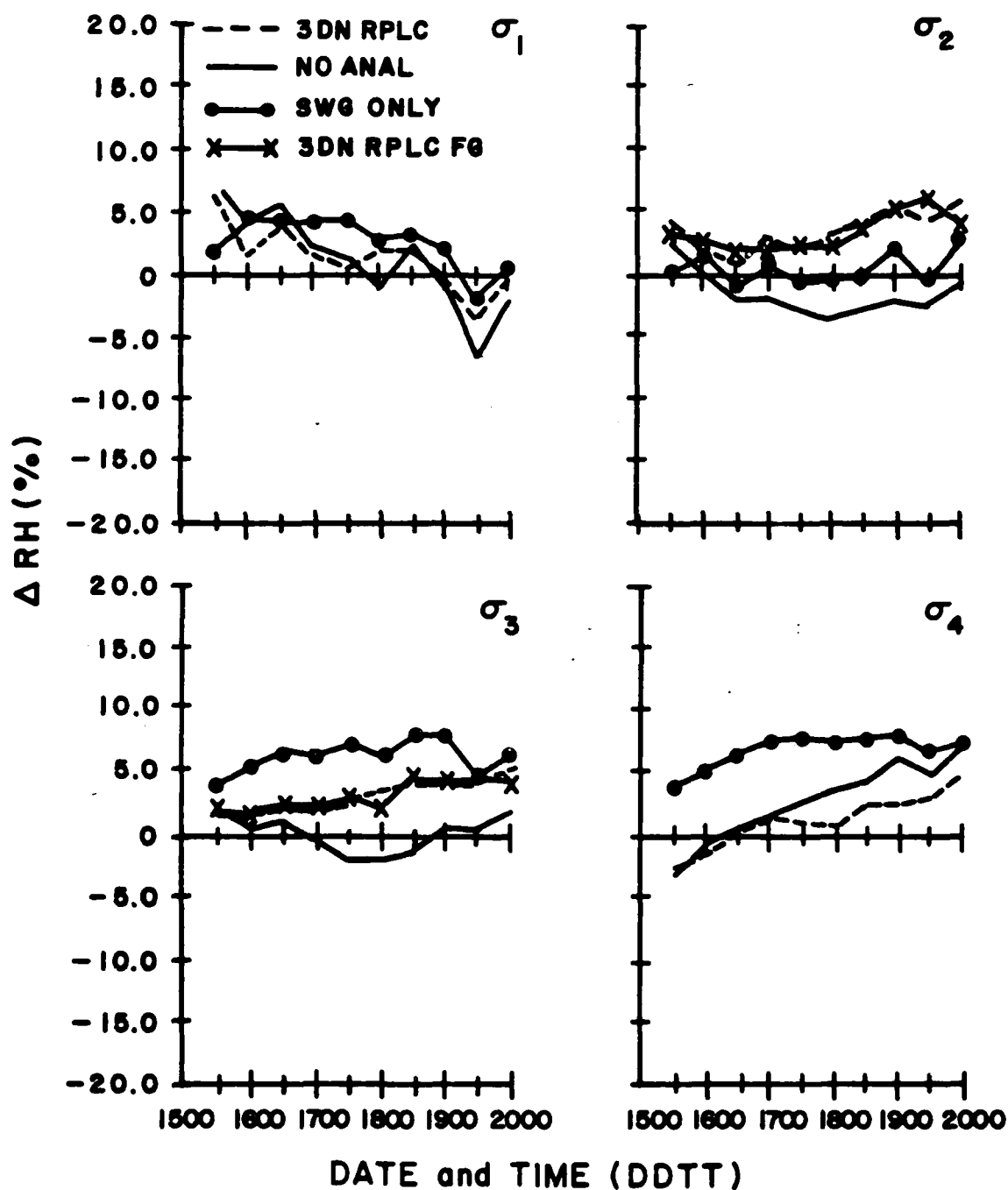
Fig. 26 (cont.)

Fig. 27 Field–Observation Bias for σ Layer Relative Humidity (Basis Observations)
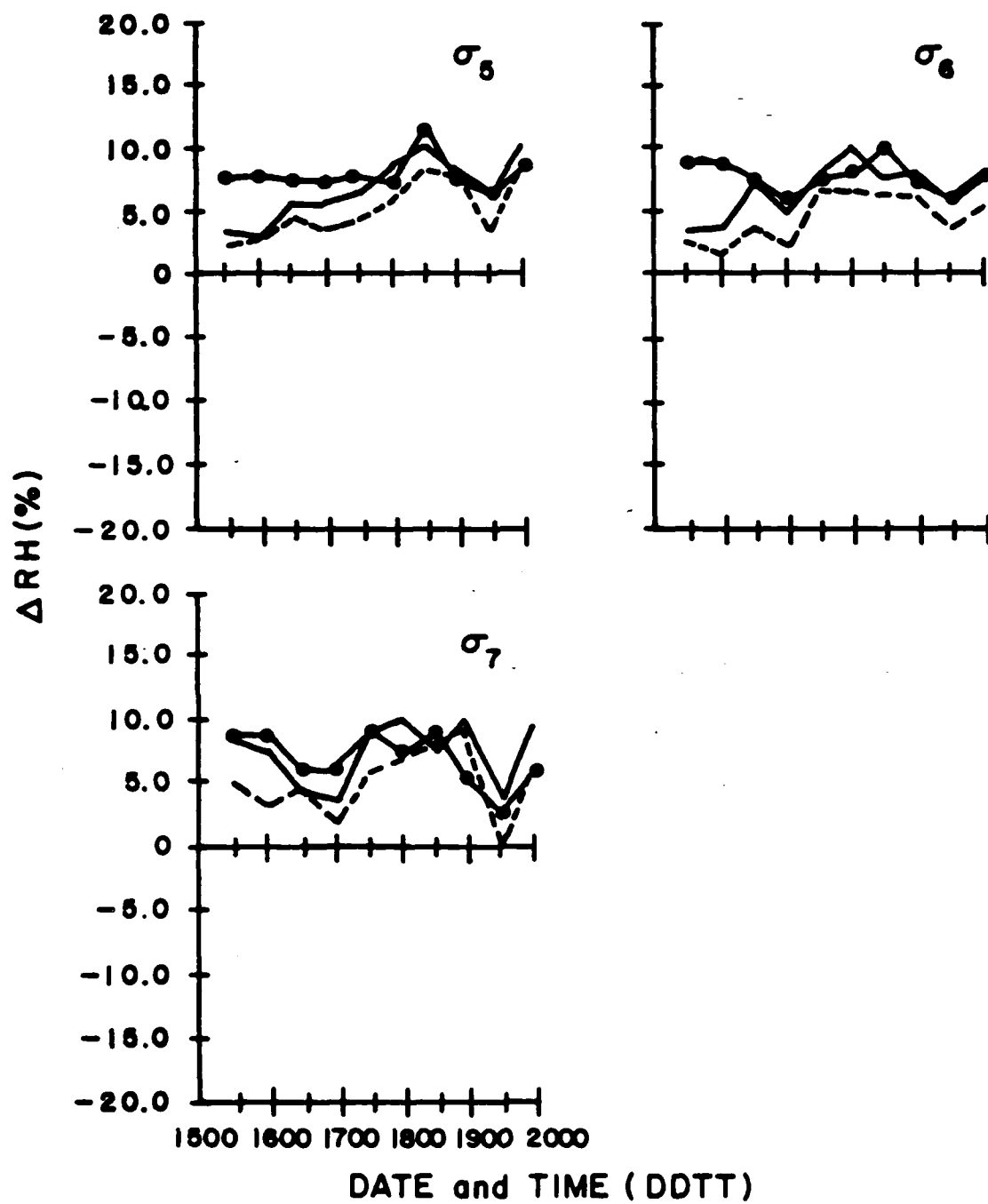
Fig. 27 (cont.)

102

more important matter here is how the forecast model responds to the replacements. That is, does the 3DN replacement lead to a more moist 6h forecast at these layers than would occur if no replacement took place? To determine the relative bias of the 3DN replacement assimilation first guess fields, they were compared with the same basis rawinsonde relative humidities at all 00, 12Z times, and their bias is plotted on the σ_2, σ_3 bias plots. The results make it clear that at these two layers, the 3DN replacement analyses lead to 6h forecast fields that are more moist than an uncorrected first guess. In the GSM, the modest dry bias in the uncorrected first guess is replaced by a more substantial moist bias in the 6h forecast when the 3DN humidities from cloudy areas are used in place of the model generated first guess for the initial conditions. This relative moist bias is retained in later analyses as the replacement method is ineffective in removing it. At all other layers where the uncorrected first guess was too moist, the 3DN replacement analyses were definitely and consistently less moist than their counterpart first guess, so in these layers the replacement was effective in reducing the model moist bias.

The SWO analyses, in considering both RMS and bias at each layer, are actually in poorer agreement with rawinsonde relative humidity than the "no analysis" fields at all layers. Whereas the RMS curves for SWO show better agreement at all layers except σ_2, σ_3, the bias curves show a greater bias at all layers except σ_2. It appears that the use of SWO values in conventionally data sparse regions would lead to an artificially too moist depiction of the atmospheric state except for possibly at σ_2, where the RMS fit is much poorer than the uncorrected first guess. On the basis of these results, one would be better off to leave the GSM uncorrected in such areas rather than use the SWO's to attempt a correction. This conclusion of course is model dependent, and cannot necessarily be applied to other global forecast models used for data assimilation.

Finally, it is of interest to examine the model generated humidity fields in an averaged sense. Fig. 28(a) is a zonal, time average of the uncorrected (ASAP5) 6h forecast fields averaged over all 00, 12Z times in the five day assimilation. Fig. 28(b) represents the difference between this plot and the same plot for the basis rawinsondes. Note the tendency for the model forecast to be too moist in the lowest and highest layers. A comparison of Fig. 28(b) with Fig. 17(b) (ASAP1) and Fig. 25(b) (ASAP3)
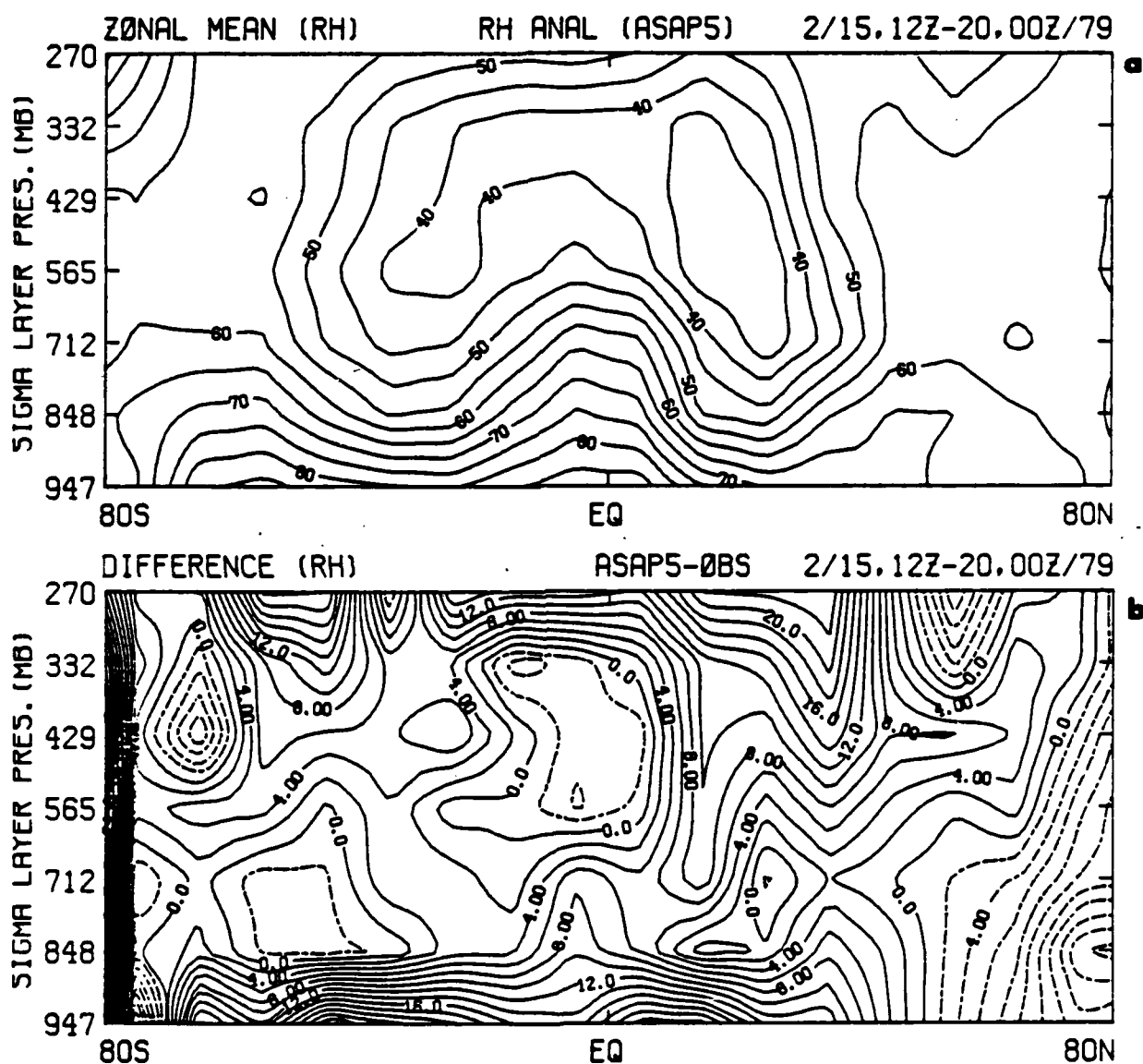
Fig. 28(a,b)   Zonal, Time Average Relative Humidity for (a) ASAP (No Humidity
Analysis) Analyses and (b) Difference between (a) and Basis
Observations (Fig. 17(a)).   Contour Interval for (a) is 5%, for
(b) is 2%.   Dashed Contours Indicate Negative Values.

reveals that a good analysis scheme will on the average lead to a good time averaged depiction of the relative humidity when produced by an objective data assimilation system.

Now that it is acknowledged that certain types of humidity information can lead to good analyses of relative humidity on the average, the question of whether this in turn leads to a better long term forecast of relative humidity must be addressed. At this point, the particular characteristics of the model being used to produce such a forecast become the most important factor in determining the answer to the question. Can a somewhat coarse resolution model with modest physical parameterizations such as the GSM be sufficiently sensitive to an initial relative humidity field so as to produce a more highly verified forecast from an initial field that more closely agrees with its objective verification data? Or, are the initial mass and motion fields more important in determining the forecast distribution of humidity? In an attempt to answer these questions, the 48h humidity forecast results at 12h intervals based on the 2/17/79 12Z analysis were compared with basis rawinsondes and RMS and bias curves were produced and plotted in Figs. 29 and 30. Fig. 31 is a plot of the RMS differences and bias for the initial RH analyses at 2/17/79 12Z for ASAP and F3A along with the RMS and bias for all ten 00, 12Z times. It is clear from both the RMS curves and bias curves that the initially closer fit of the ASAP1 analysis to the observations than that for F3A as seen in Fig. 31 did not in this case lead to a closer fit for the forecast in Figs. 29 and 30.

Notice first in the RMS curves, by comparing the 12h forecast curves with the initial curves, that the forecast model quickly moves the RMS values to the 20-30 percent range where the initial F3A values were. In fact, after 12h the RMS differences for F3A based forecast are slightly lower at all layers except the lowest, and continues to be lower even after 48h. Clearly, the better initial RMS fit in the ASAP1 analysis had no positive impact upon the resulting forecast, and the fact that the ASAP1 forecast RMS values are actually greater than those for the F3A-based forecasts suggests that other differences (mass-motion) between the two analyses had a greater effect than initial humidity on the humidity forecast. The three ASAP based forecasts show little difference in RMS; however, the ASAP2 does appear to have higher values than the other two.
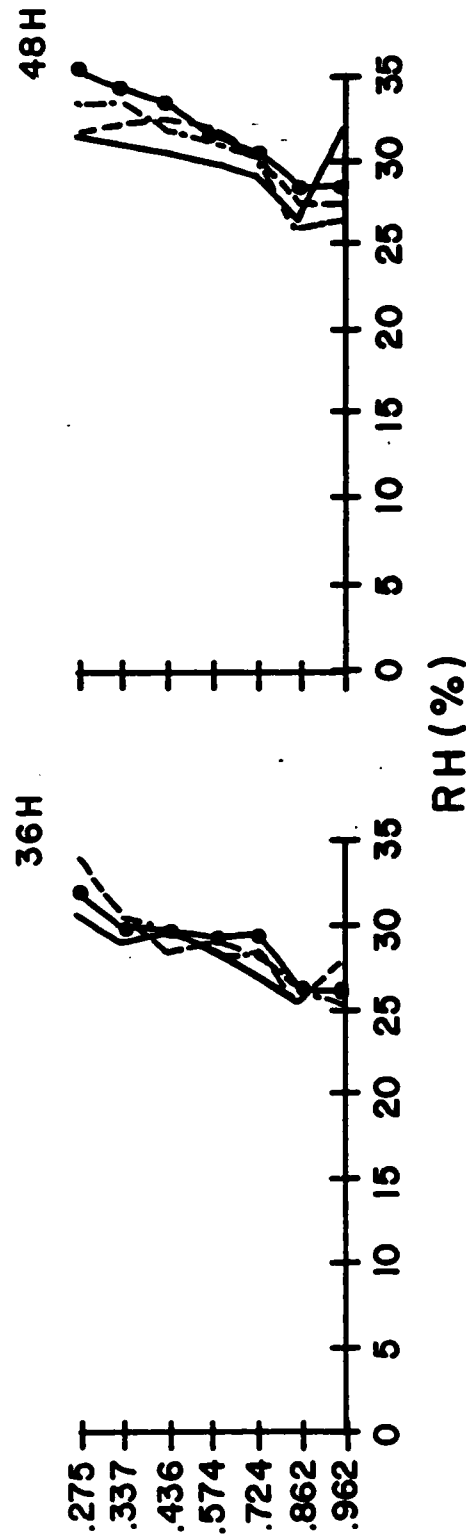
105
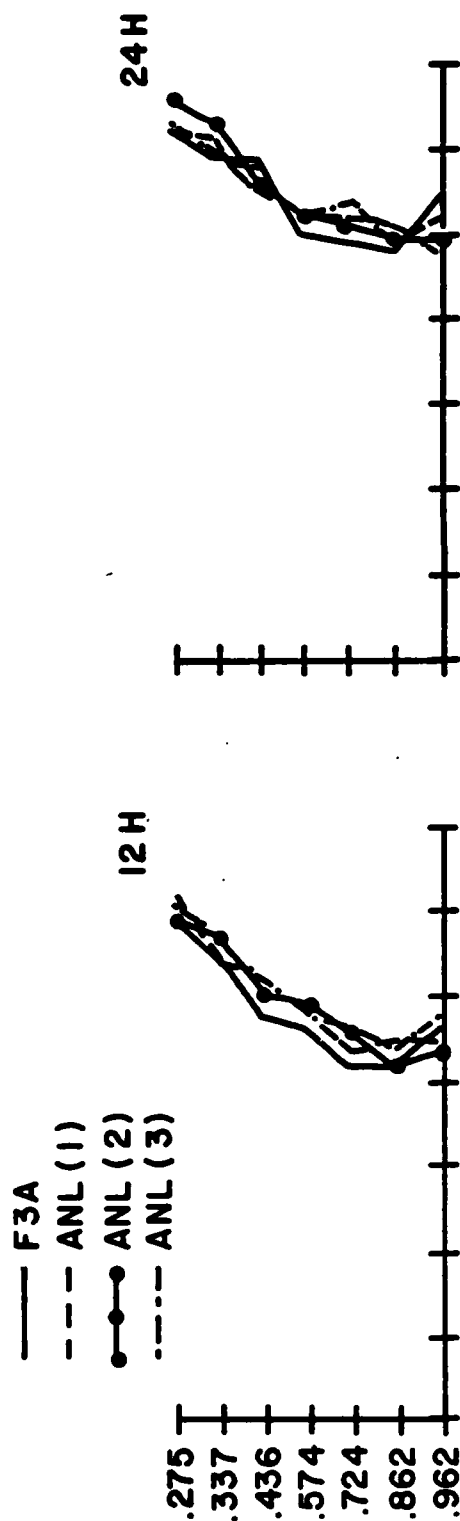
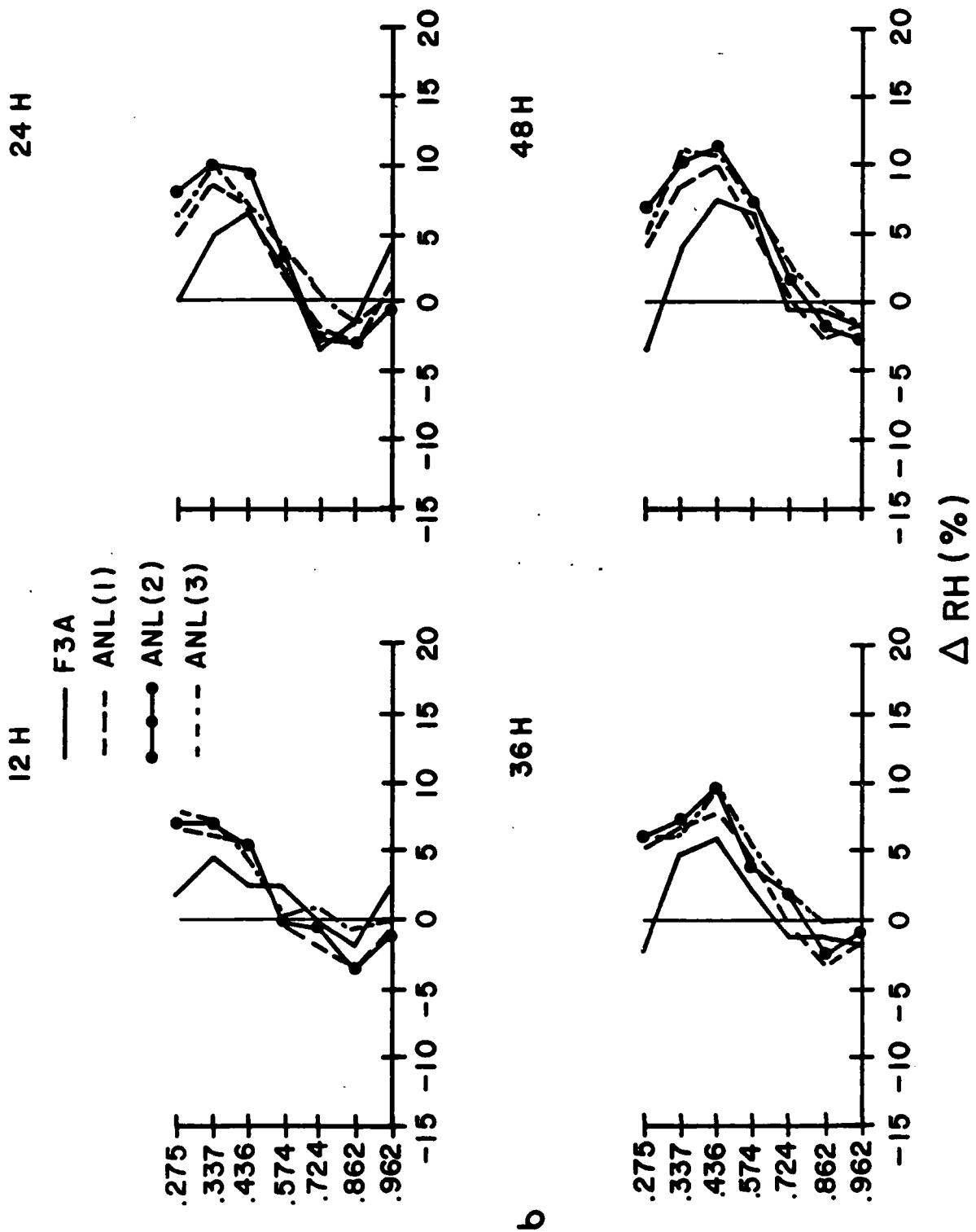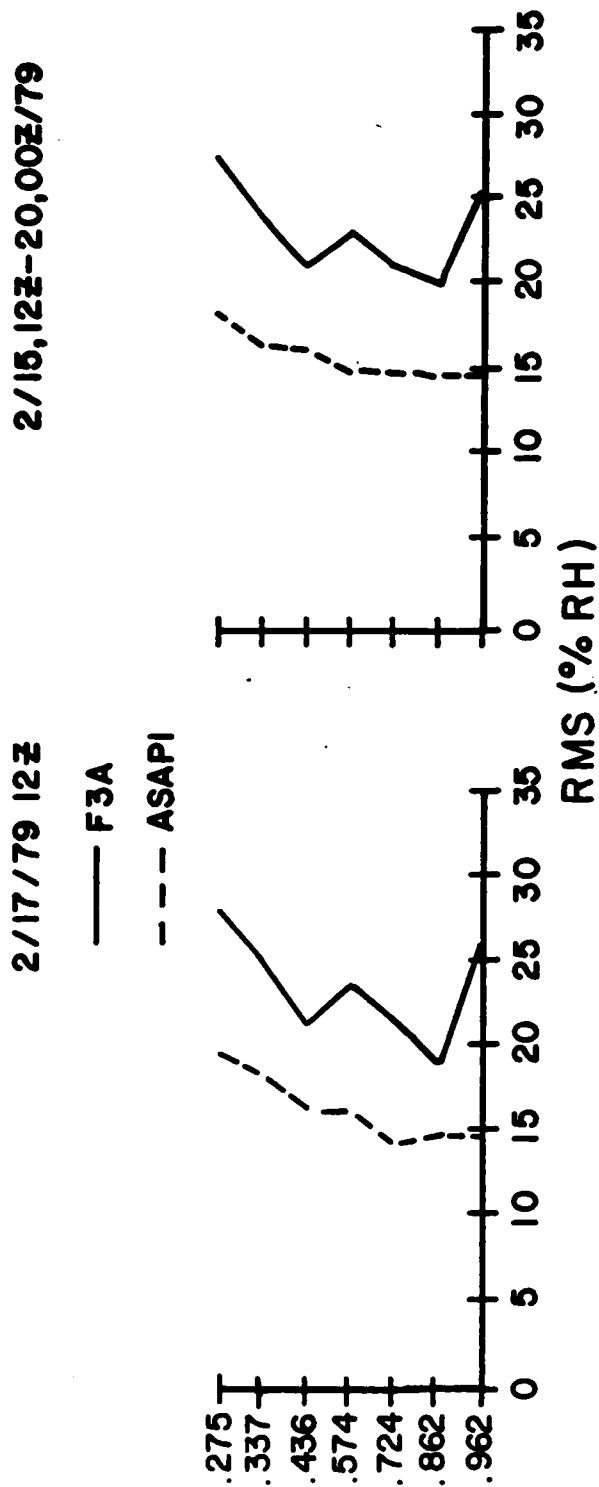Fig. 29 RMS Differences on σ Layers between Forecast Relative Humidity Fields and Basis Observations

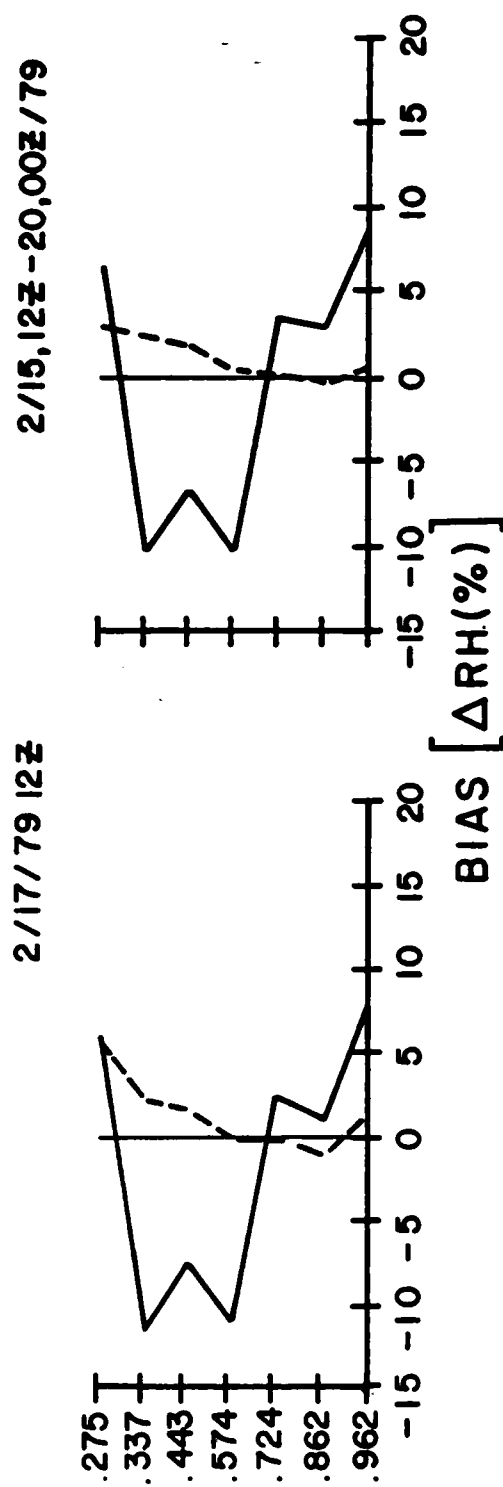Fig. 30 Forecast Field - Observation Bias for σ Layer Relative Humidity (Basis Observations)

Fig. 31 RMS Differences between Analysis Fields and Observations and Field-Observation Bias for σ Layer Relative Humidity

A look at the forecast bias for the F3A based forecast as compared to the ASAP based forecasts in Fig. 30 reveals that the F3A based forecasts tend to be less dry in the four lowest layers and less moist in the three highest layers after 12h. By 48h, the F3A and ASAP based forecasts all show about the same amount of dry bias in the lowest four layers, but the F3A based forecast shows less of a moist bias in the upper three layers. The reason for these trends is clear from a comparison with the initial biases in Fig. 31. The F3A analysis has a clear moist bias in the lowest three layers where the forecast model tends to generate humidities that are too low, while in the next three layers the F3A analysis shows a pronounced dry bias where the model tends to generate humidities that are too high. Thus, when the model moves the bias to the left (drier) in the lowest three layers and to the right (more moist) in the next three layers, the F3A based forecast shows lower bias because its initial fields compensated in sign more greatly than did the lower bias ASAP1 fields. It is evident from these results that the model establishes its own bias profile configuration without regard to the configuration of the initial bias. Here again, very little difference is seen among the biases for the three ASAP based forecasts, although the ASAP2, ASAP3 biases are higher than ASAP1 after 48h.

It is apparent in this case that for the GSM under these circumstances, closeness of fit of the initial humidities with observations did not result in better verification with observations in the ensuing forecast. Presumably the GSM in its present configuration is not capable of preserving the better initial verification of the ASAP humidity fields in its forecast. It may be that the difference between the F3A and ASAP mass and motion fields plays a bigger role in determining the forecast distribution of humidity than does the initial humidity distribution. This was a conclusion reached by Lejenäs (1979) in a study using a regional model for precipitation forecasting. He concluded that vertical velocities in the initial wind field are more important than fine detail in the moisture field for short term (<24h) forecasts, and that for global long term forecasts initial humidity specification is of little importance to the forecast humidity. Similar conclusions were reached by Smagorinsky et al. (1970), who found that after about 6 hours, there were generally no significant differences in forecast precipitation rate between forecasts involving various moisture specifications. However, in the present study cloud

distribution is of more importance, which in turn suggests that humidity rather than precipitation is the more important factor. In response to the conclusion by Lejenäs, it must be stated that the degree to which that conclusion is true is dependent upon the forecast model, as was stated previously. To determine whether the mass-motion fields might have the greater effect on the humidity forecast in the case of the GSM, the relative humidity fields in the F3A and ASAP1 analyses were switched and new 48h forecasts were generated. Forecast RMS difference and bias in comparison to basis observations were generated and are displayed in Figs. 32 and 33. To distinguish more clearly the effect of switching the relative humidity between the two initial analyses on the resulting forecasts, the RMS and bias curves from Figs. 29 and 30 are included.

Considering first the RMS curves, it is apparent in the comparison of the two dashed (F3A mass-motion) curves that using the better fitting initial ASAP humidities had very little effect on the humidity forecast. The relative humidity forecast from the F3A analysis improved only slightly (at most levels less than 1 percent RMS) when the better fitting initial ASAP1 humidity analysis replaced the F3A humidity analysis. However, the relative humidity forecast from the ASAP analysis became more substantially worse (at most layers more than 2 percent RMS) when the poorer fitting initial F3A humidity analysis replaced the initial ASAP1 analysis. This suggests that closeness of fit of the original humidity analysis played a greater role in the humidity forecast for the ASAP based forecast than for the F3A based forecast. In general, the humidity forecasts from the F3A height-wind fields have a lower RMS than the forecasts from the ASAP1 fields regardless of which initial relative humidity analysis was used. This indicates that the initial mass-motion analysis has a greater role than initial relative humidity in determining GSM relative humidity forecast accuracy. However, the fact that the use of ASAP1 initial humidities in the ASAP1 analyses led to better humidity forecasts than using F3A initial humidities indicates that accuracy in initial humidity analyses can play a secondary role in the resulting humidity forecast.

The bias curves in Fig. 33 confirm the earlier conclusion that the GSM establishes its own moisture bias regardless of initial humidity bias configuration. The comparisons between the two F3A based forecasts (dashed curves) and two ASAP1 based forecasts (solid curves) are shown only for 36h
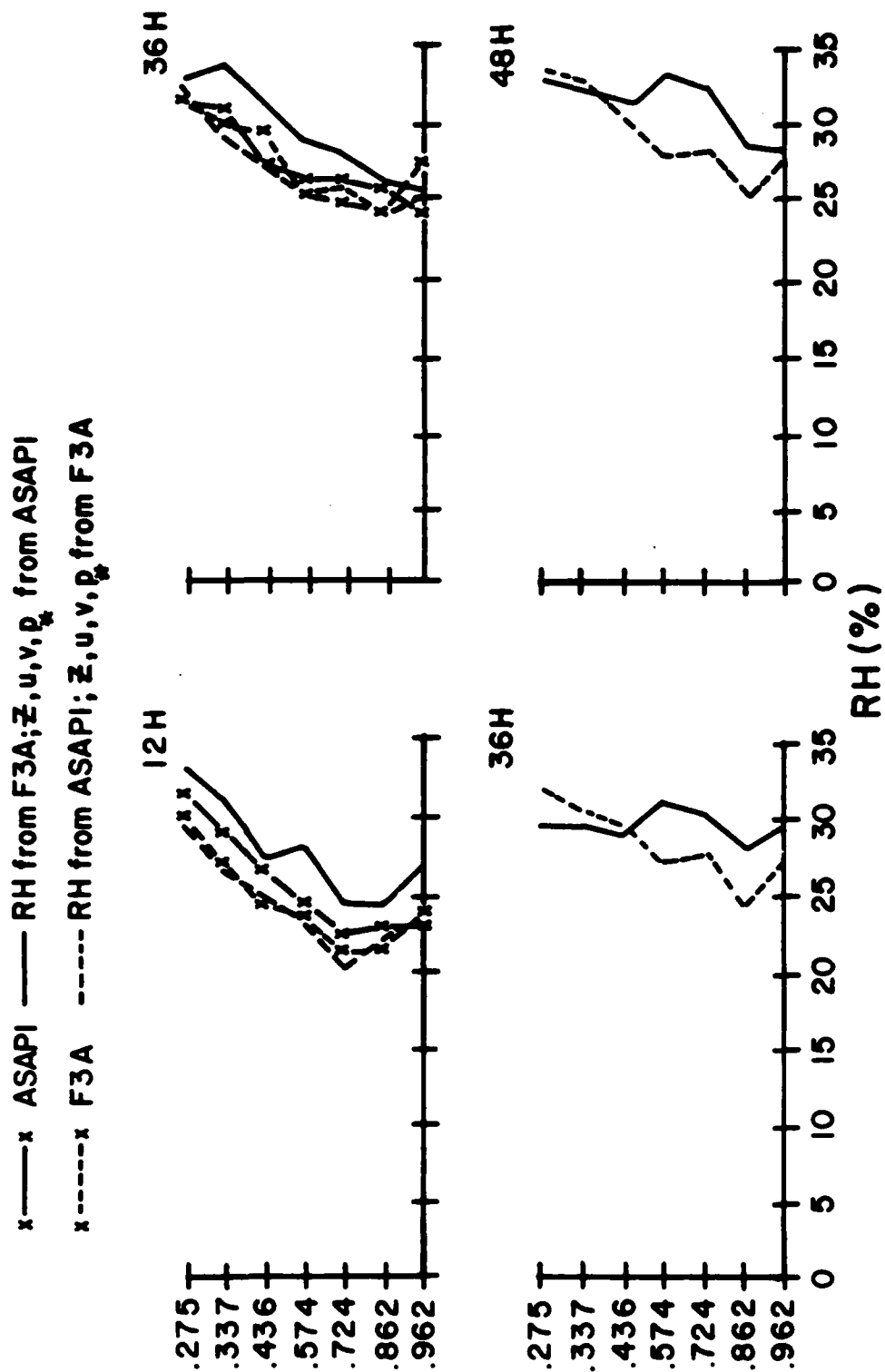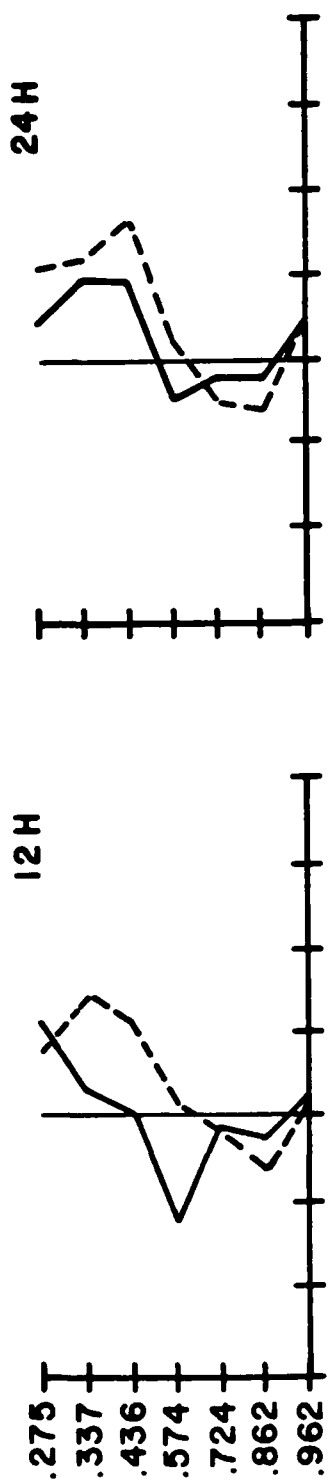
110

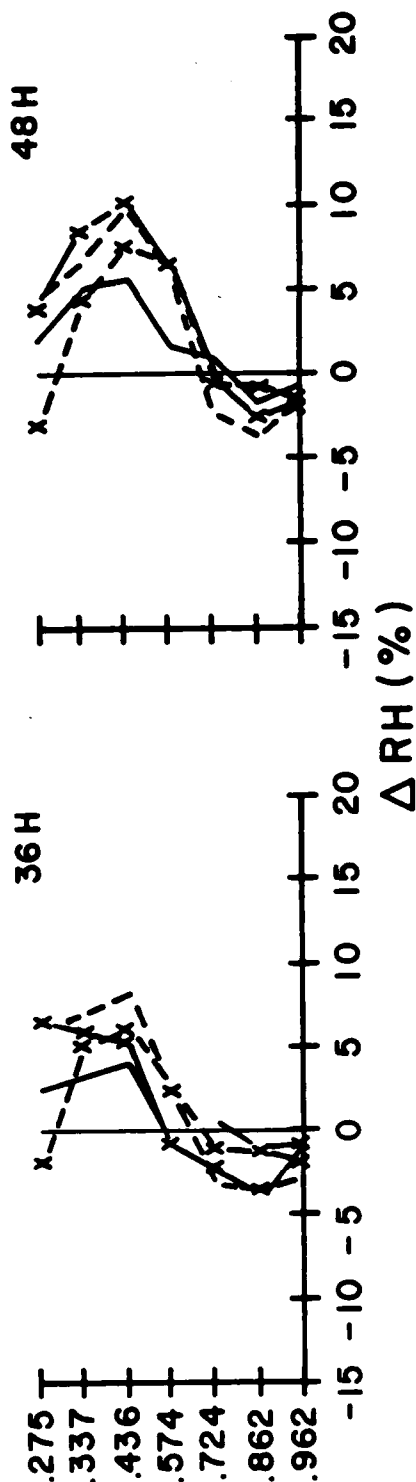Fig. 32 RMS Differences on σ Layers between Forecast Relative Humidity Fields and Basis Observations

Fig. 33 Forecast Field – Observation Bias for σ Layer Relative Humidity (Basis Observations)

112

and 48h when the model has clearly established its bias configuration. In both pairs of curves, the lower dry biases and upper moist biases are lower for the forecasts which use the initial F3A relative humidities. This is due to the earlier stated fact that the initial F3A bias configuration more substantially compensated for the model generated biases. Here again, it is clear that the mechanics of the model overwhelmingly determine the bias of the forecast humidity fields, and the initial humidity biases play very little role in affecting the trends (as opposed to actual values) of the model generated bias. To determine the role of the initial mass-motion analysis in the forecast humidity bias, we compare the two curves with F3A relative humidity (————— and x---x) on one hand, and the two curves with ASAP1 relative humidity (---- and x———x) on the other. In both cases, the solid curves (ASAP1 mass-motion) show moderately less bias at 36h than their F3A mass-motion counterparts at all layers except the top. However, much of the difference is lost by 48h and in some cases is actually reversed. At most, the mass-motion analyses play a secondary role in determining GSM humidity forecast bias, with the model itself playing the greatest role.

VII. CONCLUSIONS AND RECOMMENDATIONS FOR FURTHER STUDY

On the basis of the results of the five day assimilation experiments described in this report, the following conclusions are given.

1) Observation error standard deviation chosen for mass and wind fields plays a crucial role in determining degree of fit of the analysis to observations. A good index of relative observation error influence is the ratio of normalized observation error for height to the same for winds.

2) The baseline AFGL GSM used in the data assimilation system produces a large positive height bias at the $\hat{\sigma} = 0.05$ level, which is a result of a warm temperature bias in the layer topped by this level. Because of the lack of high quality height and wind data available at or near that level, the ASAP analysis is unable to correct this bias substantially at each analysis time. As a result, the bias grows in time during the course of the assimilation. However, the unabated growth of the bias in the assimilation analyses is restricted to the layer above $\hat{\sigma} = 0.10$.

3) Initial fit to observations appears to play a greater role in forecast verification for winds than it does for heights in 48h forecasts

113

produced by the GSM. A close fit to heights in the initial conditions does not necessarily result in a better height forecast verification, whereas the GSM does seem to preserve the relationship between the relative observational data fits for winds for several initial conditions through the forecast period.

4) Fit of univariate relative humidity analyses to observations is very much dependent upon the observation error standard deviations assigned to the various observation types. Small observation error standard deviation (OESD) values for a certain data type result in a closer fit of the analysis to that type of observational data.

5) The relatively low values of OESD for rawinsonde relative humidity observations and the relatively high values of OESD for alternative humidity sources lead to a strong preference for use of rawinsonde observations in a mixed analysis. Thus, in areas with even a few, somewhat scattered rawinsonde observations, the analysis procedure will use those before using closer and more densely concentrated alternative humidity estimates. In regions rich in rawinsonde observations, alternative humidity sources are effectively excluded from use in the analysis.

6) Though the magnitude of relative humidity corrections may be appreciably smaller in alternative humidity rich areas than in their rawinsonde rich counterparts, the analysis error in the alternative data rich area is appreciably reduced from its value when no corrections are made in the area. Thus, the analysis error in alternative data rich areas is at a level above that for rawinsonde rich areas but significantly below climatological limits of the assimilation system.

7) 3DNEPH replacement of first guess relative humidity has a more positive effect overall on the analysis than the use of 3DNEPH and surface weather observation (SWO) inferred humidities used as pseudo-observations in an analysis mode. This suggests that since the 3D nephanalysis is already a form of humidity analysis, 3DNEPH inferred humidities should be used in a replacement mode rather than in an analysis correction mode to achieve their maximum positive effect.

8) Use of 3DNEPH inferred relative humidities in cloudy regions as a direct replacement of first guess humidities represents an improvement over no humidity correction to the first guess at layers σ_1 and σ_4 – σ_7. At σ_2 and σ_3, use of 3DNEPH humidities as first guess

replacements leads to a significant moist bias in the ensuing 6h GSM forecast, where a modest dry bias had occurred when no replacement had taken place. The replacements at these layers were not effective in reducing the moist bias in later analyses.

9) Use of surface weather observation inferred humidities in an OI analysis mode represents a worse analysis overall than no humidity correction to the GSM first guess. This is due to the introduction of a significant moist bias over the "no analysis" case at all layers except σ_2, where the RMS differences with rawinsonde relative humidity were excessive. This conclusion is dependent upon the algorithm used to infer humidities from SWO's and on the particular assimilation model. In the case of this study, the Tibaldi (ECMWF) algorithm is used for the former and the AFGL GSM (physics as in Sela, 1980) is used for the latter.

10) A closer fit to observations in one initial relative humidity analysis over another analysis does not necessarily result in a better verification against observations of a 48h forecast when the GSM is initialized by the two humidity analyses. Initial RMS fit to data in the relative humidity analysis has less of an effect on the humidity forecast RMS fit than does the initial mass-motion field. The GSM tends to create its own humidity forecast bias configuration (too dry in the lower layers, too moist in the upper layers) without the initial humidity bias having any effect on the production of these bias trends. Unfortunately, it was discovered after the completion of the experiments that the version of the GSM used both in assimilation and forecasting had effectively no moist convective adjustment. A companion journal article (submitted to Monthly Weather Review) includes additional results for cases when the moist convective adjustment scheme is utilized as described by Sela (1980). In general, the present version of the GSM is generally insensitive to specification of initial relative humidity conditions in its generation of humidity forecasts. It may be that later upgrades in the GSM moist convection parameterization (NMC 1983, NMC 1985), or new parameterizations of moist convection, boundary layer physics, and radiation developed for AFGL will lead to an improvement in model sensitivity to initial humidity distribution. This would make efforts to analyze more accurately both conventional data rich and conventional data sparse (alternative data rich) regions worthwhile in that they would lead in turn to more accurate humidity

forecasts in both types of regions.

The research activities described in this report are a first attempt to use the AFGL GSM as a global data assimilation model. As such, the results of this study answer some questions about data assimilation possibilities at AFGL, but suggest many more questions that need to be answered about such a system. The following list of suggestions for further study is by no means exhaustive, but merely represents the most obvious starting point for further exploration of the role of various types of observations in four-dimensional data assimilation.

1) In light of the use of height on σ layers as the mass field analysis medium, more study of the best means of converting height analysis corrections to temperature corrections should be undertaken.

2) The cause of the large warm temperature bias at σ layer σ_{11} (i.e., the layer between $\sigma = 0.1$ and $\sigma = 0.05$) in the 12 layer version of the GSM should be explored and resolved.

3) At least two more days of assimilations following the five day experimental period described in this study should be carried out to verify that the RMS differences between analysis winds and observational winds do not grow in magnitude beyond their fifth day level.

4) The effect of global average temperature changes in the assimilation on global averaged surface pressure, diagnosed from analyzed σ layer temperatures, should be studied in more detail to verify the realism of the derived surface pressures.

5) More long term forecasts should be run, especially from initial fields later in the assimilation period, to verify conclusions about forecast characteristics of the GSM.

6) A new collocation study of FGGE II-B satellite derived layer precipitable water values with rawinsondes should be conducted using the reprocessed data set. A ln q vs. ln p assumption should be used in each report layer to convert layer precipitable water to q.

7) Error statistics for satellite soundings from collocation studies with rawinsondes for both Z and RH should be conducted for land and ocean based satellite soundings for a comparison of error levels with those obtained previously for all soundings. If the land based levels are found to be of comparable quality to ocean based soundings, such soundings should be included in the assimilation data pool.

8) Other methods of horizontal and vertical compaction of 3DENPH cloud amounts should be tested in rawinsonde humidity collocation studies in order to maximize the amount of information that can be derived from the cloud analysis while minimizing the collocation differences with rawinsonde humidities. Also, the collocation study should be carried out for the June period to verify that the preference for the Tibaldi method is not seasonally dependent.

9) More long term humidity forecasts should be generated using the GSM and ASAP, FGGE III-A initial conditions, to better ascertain the sensitivity of the model to initial conditions and to gain a better understanding of its humidity forecast characteristics.

10) A new study has been initiated elsewhere to study the effect of using satellite derived data (both temperature and moisture) in the ASAP OI procedures on the data assimilation analyses while using new GSM parameterization schemes for boundary layer, moist convection, and radiation physics. Once these studies and tests have been completed and the upper level temperature bias corrected in the GSM, the ASAP experiments ASAP1 (conventional RH only), ASAP5 (no RH analysis), ASAP4 (3DN replacement only), and a combination of conventional RH OI where such data are fairly plentiful and 3DN replacement where possible elsewhere, should be run in an assimilation mode. Forecasts generated from these fields should be examined to see if humidity forecasts from these GSM versions benefit from better specification of initial humidity in both conventional data rich and conventional data sparse (alternative data rich) regions.

APPENDIX A. Flattery Algorithm

Given the system of linear constraints imposed on the interface temperatures $\{\hat{T}_k\}$, $k = 1, \ldots, K + 1$ and the layer temperatures $\{T_k\}$, $k = 1, \ldots, K$. We assume:

(1) that the layer temperature T_k is the arithmetic average of the bounding interface temperatures $\hat{T}_k$, $\hat{T}_{k+1}$

$$T_k = \frac{1}{2}(\hat{T}_k + \hat{T}_{k+1}), \quad k = 1, \ldots, K; \tag{A1}$$

(2) that temperature in the layer bounded by two pressure levels $\bar{p}_k$, $\bar{p}_{k+1}$ is linear in $\ln p$, so that the interface temperature $\hat{T}_{k+1}$ is given in terms of the layer temperatures T_k and T_{k+1} as

$$\hat{T}_{k+1} = T_k W_{L,\,k+1} + T_{k+1} W_{U,\,k+1}$$

where

$$W_{L,k+1} = \frac{\ln\,(\hat{p}_{k+1}/\bar{p}_{k+1})}{\ln\,(\bar{p}_k/\bar{p}_{k+1})}, \quad W_{U,k+1} = \frac{\ln\,(\bar{p}_k/\hat{p}_{k+1})}{\ln\,(\bar{p}_k/\bar{p}_{k+1})} \tag{A2}$$

$$k = 1, \ldots, K;$$

(3) that both Eq. (A1) and Eq. (A2) are valid also at the lowest and highest bounding interfaces, i.e., $\hat{p}_1$ and $\hat{p}_{K+1}$. Hence

$$\hat{T}_1 = 2T_1 - \hat{T}_2$$

$$= 2T_1 - (T_1 W_{L,2} + T_2 W_{U,2})$$

or

$$\hat{T}_1 = (2 - W_{L,2})T_1 - W_{U,2}T_2 \tag{A3}$$

$$\equiv T_L W_{L,1} + T_2 W_{U,1}.$$

118

Similarly

$$\hat{T}_{K+1} = 2\hat{T}_K - \hat{T}_K$$

$$= 2T_K - (T_{K-1}W_{L,K} + T_K W_{U,K})$$

or   (A4)

$$\hat{T}_{K+1} = (2 - W_{U,K}) T_K - W_{L,K} T_{K-1}$$

$$\equiv T_{K-1}W_{L,K+1} + T_K W_{U,K+1}.$$

Here, the subscript k designates level in the vertical and is chosen to increase upward. The geometrical configuration may be depicted as follows:
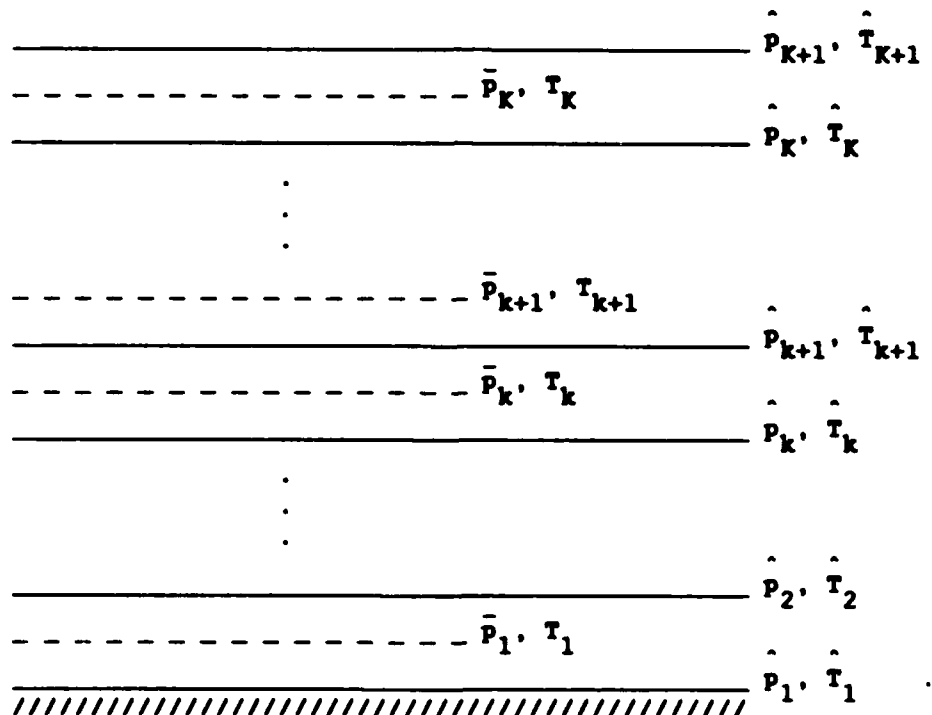
When $\hat{p}_{K+1} = 0$, we cannot employ this method. There are different alternatives here:

(1) Introduce $\hat{p}'_{K+1}$, which is between $\hat{p}_K$ and $\hat{p}_{K+1}$

(2) Assume that the layer above p_K is isothermal so that

$$\hat{T}_{K+1} = T_K.$$

The constraints listed above may be put into matrix form given by

$$\hat{A}\hat{T} = BT \tag{A5}$$

where matrices A, B and vectors $\hat{T}$, T are defined as follows:

$$
A = \begin{bmatrix}
0.5 & 0.5 & 0 & \cdots & 0 \\
0 & 0.5 & 0.5 & \cdots & 0 \\
0 & 0 & 0.5 & \cdots & 0 \\
\cdot & \cdot & \cdot & & \\
\cdots & \cdots & \cdots & 0.5 & 0.5 \\
1 & 0 & 0 & \cdots & 0 \\
0 & 1 & 0 & \cdots & 0 \\
\cdot & \cdot & \cdot & & \\
0 & 0 & 0 & & 1
\end{bmatrix}
\begin{array}{l} \left. \vphantom{\begin{matrix}1\\1\\1\\1\end{matrix}} \right\} K \\[2em] \left. \vphantom{\begin{matrix}1\\1\\1\\1\end{matrix}} \right\} (K+1) \end{array}
\qquad
\hat{T} = \begin{bmatrix}
\hat{T}_1 \\
\hat{T}_2 \\
\hat{T}_3 \\
\cdot \\
\cdot \\
\cdot \\
\hat{T}_K \\
\hat{T}_{K+1}
\end{bmatrix}
\right\} (K+1)
$$

$$\longleftarrow (K+1) \longrightarrow$$

$$
B = \begin{bmatrix}
1 & 0 & 0 & \cdots & 0 \\
0 & 1 & 0 & \cdots & 0 \\
0 & 0 & 1 & \cdots & 0 \\
\cdot & \cdot & \cdot & & \\
0 & 0 & 0 & \cdots & 1 \\
W_{L,1} & W_{U,1} & 0 & \cdots & 0 \\
W_{L,2} & W_{U,2} & 0 & \cdots & 0 \\
\cdot & \cdot & \cdot & & \\
0 & 0 & 0 & W_{L,K} & W_{U,K} \\
0 & 0 & 0 & W_{L,K+1} & W_{U,K+1}
\end{bmatrix}
\begin{array}{l} \left. \vphantom{\begin{matrix}1\\1\\1\\1\end{matrix}} \right\} K \\[3em] \left. \vphantom{\begin{matrix}1\\1\\1\\1\end{matrix}} \right\} (K+1) \end{array}
\qquad
T = \begin{bmatrix}
T_1 \\
T_2 \\
T_3 \\
\cdot \\
\cdot \\
\cdot \\
\cdot \\
T_{K-1} \\
T_K
\end{bmatrix}
\right\} K
$$

$$\longleftarrow K \longrightarrow$$

To solve Eq. (A5) in accordance with the least-squares principle we proceed as follows:

(A) When $\{T_k\}$ is given,
$$\hat{T} = (A^TA)^{-1}A^TBT \tag{A6}$$

(B) When $\{\hat{T}_k\}$ is given,
$$T = (B^TB)^{-1}B^TA\hat{T} . \tag{A7}$$

APPENDIX B. Computation of Surface Pressure from Analyzed
Heights of σ Levels and Terrain Height

The analysis of temperature implies a correction to the geopotential height at all σ levels. This in turn implies a change in the surface pressure at the fixed height of the model terrain. To estimate the update surface pressure p_* given the original geopotential Φ and update geopotential $\hat{\Phi}$ of the σ levels, consider the hydrostatic equation in the form

$$\partial \Phi / \partial \ln p = -RT.$$

Rewriting in the form $p \dfrac{\partial \Phi}{\partial p} = -RT$, and noting that

$$\frac{\partial \Phi}{\partial p} = \frac{\partial \Phi}{\partial \sigma} \frac{\partial \sigma}{\partial p}$$

where $\sigma = p/p_*$ and $\partial \sigma / \partial p = 1/p_*$, we have

$$p \frac{\partial \Phi}{\partial p} = \sigma \frac{\partial \Phi}{\partial \sigma} \quad .$$

Thus, $\dfrac{\partial \Phi}{\partial \ln \sigma} = -RT$, and if we assume T varies linearly in $\ln \sigma$, then Φ must vary quadratically in $\ln \sigma$:

$$\Phi(\ln \sigma) = C + A \ln \sigma + B \ln^2 \sigma.$$

If we denote $\hat{\Phi}_2$, $\hat{\Phi}_3$, $\hat{\Phi}_4$ to be the first guess geopotential at levels σ_2, σ_3, σ_4, the three σ levels immediately above $\sigma_1 = 1.0$, then by writing the above quadratic expression in terms of these three levels, and solving the resulting equations for A, B, C, we have

$$B = [(\hat{\Phi}_3 - \hat{\Phi}_2)/(\ln \hat{\sigma}_3 - \ln \hat{\sigma}_2) - (\hat{\Phi}_4 - \hat{\Phi}_3)/(\ln \hat{\sigma}_4 - \ln \hat{\sigma}_3)]/(\ln \hat{\sigma}_2 - \ln \hat{\sigma}_4)$$

$$A = [(\phi_4 - \phi_3) - B(\ln^2 \hat\sigma_4 - \ln^2 \hat\sigma_3)]/(\ln \hat\sigma_4 - \ln \hat\sigma_3)$$

$$C = \phi_3 - A \ln \hat\sigma_3 - B \ln^2 \hat\sigma_3 \ .$$

Similar expressions exist for A', B', C' in terms of the geopotentials ϕ_2', ϕ_3', ϕ_4' of the analyzed field. Using these values, we can evaluate the computation terrain geopotential ϕ_*^C, ϕ_*^C at $\hat\sigma_1 = 1.0$ from both fields:

$$\phi_*^C = C + A \ln \hat\sigma_1 + B \ln^2 \hat\sigma_1 = C \ ; \quad \phi_*^{C'} = C' + A' \ln \hat\sigma_1 + B' \ln^2 \hat\sigma_1 = C' \ .$$

Given the first guess surface pressure p_* on the actual model terrain geopotential ϕ_*, we can estimate the computational values of surface pressure from

$$p_*^C = p_* \exp[(\phi_* - \phi_*^C)/(R\bar T)] \ ; \quad p_*^{C'} = p_* \exp[(\phi_* - \phi_*^{C'})/(R\bar T')]$$

where

$$\bar T = \frac{1}{2}(T_1 + T^C) \ ; \quad T^C = (\phi_2 - \phi_*^C)/[R(\ln \hat\sigma_1 - \ln \hat\sigma_2)]$$

$$\bar T' = \frac{1}{2}(T_1' + T^{C'}) \ ; \quad T^{C'} = (\phi_2' - \phi_*^{C'})/[R(\ln \hat\sigma_1 - \ln \hat\sigma_2)] \ .$$

Then the final estimate of updated surface pressure is

$$p_*' = p_* + (p_*^{C'} - p_*^C) \ .$$

APPENDIX C. NMC Subroutine PTOSIG

The subroutine generates estimates of values of dynamic variables such as temperature T, wind speeds u, v, and specific humidity q, all of which are defined as layer variables. The underlying assumptions are:

(1) The geopotential of a pressure surface is a quadratic function of ln p.
(2) The winds and natural logarithm (ln) of specific humidity are linear functions of ln p.
(3) The temperature T in the layer is estimated from ϕ at the surrounding model levels using the hydrostatic equation

$$\partial\phi/\partial \ln p = -RT.$$

A. Calculation of Layer Temperature

The first step is to calculate the geopotential at the model layer interfaces (levels) from geopotential ϕ_1, ϕ_2, ..., ϕ_L and temperature T_1, T_2, ..., T_L known at the pressure levels p_1, p_2, ..., p_L. Assuming ϕ is quadratic in ln p, we have

$$\phi(\ln p) = \phi (\overline{\ln p}) + A(\ln p - \overline{\ln p}) + \frac{B}{2} (\ln p - \overline{\ln p})^2 \qquad (C1)$$

for $p_2 \leq p \leq p_1$. Here A and B are constants and

$$\overline{\ln p} = \frac{1}{2} (\ln p_1 + \ln p_2). \qquad (C2)$$

By the hydrostatic assumption, we have

$$\partial\phi/\partial \ln p = -RT = A + B(\ln p - \overline{\ln p})$$

124

$$\partial^2 \phi / \partial (\ln p)^2 = -R(\partial T / \partial \ln p) = B.$$

The last relation in the second equation states that T must be a linear function in ln p; hence

$$\partial T / \partial \ln p = (T_1 - T_2)/(\ln p_1 - \ln p_2) \text{ in } p_2 \le p \le p_1$$

and

$$B = -R(T_1 - T_2)/(\ln p_1 - \ln p_2). \tag{C3}$$

Next, by substituting ϕ_1, ϕ_2 in Eq. (C1) we obtain

$$\phi_1 = \phi(\overline{\ln p}) + A(\ln p_1 - \overline{\ln p}) + \frac{B}{2}(\ln p_1 - \overline{\ln p})^2 \tag{C4}$$

$$\phi_2 = \phi(\overline{\ln p}) + A(\ln p_2 - \overline{\ln p}) + \frac{B}{2}(\ln p_2 - \overline{\ln p})^2. \tag{C5}$$

Adding these two and noting the definition of $\overline{\ln p}$ in Eq. (C2), we find

$$\frac{1}{2}(\phi_1 + \phi_2) = \phi(\overline{\ln p}) + \frac{B}{2}\{[\ln p_1 - \frac{1}{2}(\ln p_1 + \ln p_2)]^2 +$$

$$[\ln p_2 - \frac{1}{2}(\ln p_1 + \ln p_2)]\} = \phi(\overline{\ln p}) + \frac{B}{8}(\ln p_1 - \ln p_2)^2;$$

that is,

$$\phi(\overline{\ln p}) = \frac{1}{2}(\phi_1 + \phi_2) - \frac{B}{8}(\ln p_1 - \ln p_2)^2. \tag{C6}$$

Subtracting Eq. (C5) from Eq. (C4), on the other hand, we find

$$A = (\phi_1 - \phi_2)/(\ln p_1 - \ln p_2). \tag{C7}$$

Eqs. (C3), (C6), and (C7) define all the parameters for evaluation of $\phi(\ln p)$ in Eq. (C1), where $p_2 \le p \le p_1$. Once $\phi(\ln p)$ is found for levels bordering (above and below) the layer for which T is desired, the local hydrostatic form

$$T = (\phi_2 - \phi_1)/[R \ln (p_1/p_2)]$$

is used to calculate layer temperature.

125

B. Calculation of Wind Components and Specific Humidity

A linear in ln p assumption is used to obtain a value $X(\ln p)$ at a desired pressure p from values of X_1, X_2, ..., X_L at pressure levels p_1, p_2, ..., p_L, where $X = u, v, \ln q$. Assume then that

$$X(\ln p) = X(\overline{\ln p}) + A(\ln p - \overline{\ln p})$$

where A is a constant in $p_2 \leq p \leq p_1$ and $\overline{\ln p} = \frac{1}{2}(\ln p_1 + \ln p_2)$. Since X is linear in ln p,

$$\partial X / \partial \ln p = A = \text{constant} = (X_1 - X_2)/(\ln p_1 - \ln p_2).$$

Then

$$X_1 = X(\overline{\ln p}) + A[\ln p_1 - \frac{1}{2}(\ln p_1 + \ln p_2)]$$

and

$$X_2 = X(\overline{\ln p}) + A[\ln p_2 - \frac{1}{2}(\ln p_1 + \ln p_2)].$$

Hence

$$X(\overline{\ln p}) = \frac{1}{2}(X_1 + X_2)$$

and

$$X(\ln p) = \frac{1}{2}(X_1 + X_2) + \frac{X_1 - X_2}{\ln p_1 - \ln p_2} [\ln p - \frac{1}{2}(\ln p_1 + \ln p_2)].$$

This last equation is the form used to interpolate between known values of X_1, X_2 for $p_2 \leq p \leq p_1$ to obtain X at p, for $X = u, v, \ln q$.

APPENDIX D. Method of Obtaining Satellite Level Temperatures
From Satellite Layer Temperatures

Given $K_s - 1$ values of satellite layer temperature $\bar{T}_k$ between layer interface pressures p_k, $k = 1$, K_s, the Flattery algorithm (see Appendix A) is used to get preliminary values of the satellite level temperatures $\hat{T}_k$, $k=1$, K_s. Then one of these values (called $\hat{T}_A$ at p_A) is picked to anchor the recalculation of the other values in the following way. Assume that the layer average temperature is defined in terms of the integral expression

$$\bar{T}_k = (p_k - p_{k+1})^{-1} \int_{p_{k+1}}^{p_k} T \, dp \qquad (D1)$$

where $T = a + b \ln p$, a linear function of $\ln p$, and $T(p_k) = \hat{T}_k$. If we denote $\Delta p_k = p_k - p_{k+1}$, $k = 1$, $K_s - 1$, then substituting the linear expression into the integral and performing the integration yields

$$\bar{T}_k = a + (b/\Delta p_k)[p_k(\ln p_k - 1) - p_{k+1}(\ln p_{k+1} - 1)]. \qquad (D2)$$

If we choose to solve upward for $\hat{T}_{k+1}$ using $\hat{T}_k$ and $\bar{T}_k$, then use

$$\hat{T}_k = a + b \ln p_k . \qquad (D3)$$

Subtracting Eq. (D3) from Eq. (D2) and solving for b yields

$$b = (\bar{T}_k - \hat{T}_k)\{[p_k(\ln p_k - 1) - p_{k+1}(\ln p_{k+1} - 1)]/\Delta p_k - \ln p_k\}^{-1} \qquad (D4)$$

and from Eq. (D3),

$$a = \hat{T}_k - b \ln p_k. \qquad (D5)$$

Then $\hat{T}_{k+1} = a + b \ln p_{k+1}$ using these values of a,b.

If, on the other hand, we wish to solve for $\hat{T}_k$ when $\hat{T}_{k+1}$, $\bar{T}_k$ are known (solving downward), we use

$$\hat{T}_{k+1} = a + b \ln p_{k+1}. \tag{D6}$$

Subtracting Eq. (D6) from Eq. (D2) and solving for b gives

$$b = (\bar{T}_k - \hat{T}_{k+1}) \; \{[p_k(\ln p_k - 1) - p_{k+1}(\ln p_{k+1} - 1)]\Delta p_k - \ln p_{k+1}\}^{-1} \tag{D7}$$

and solving Eq. (D6) for a gives

$$a = \hat{T}_{k+1} - b \ln p_{k+1} . \tag{D8}$$

Then $\hat{T}_k = a + b \ln p_k$ using these values of a, b. $\hat{T}_A$, p_A are the anchor levels from which values of $\hat{T}_k$ at levels above and below can be evaluated in a stepwise fashion.

This method serves as an alternative to using the Flattery method to estimate the level temperatures $\hat{T}_k$ at all levels from the layer temperatures $\bar{T}_k$. A test was performed using a radiosonde sounding to simulate satellite data to determine which of the two methods produced the better estimates of level height from layer temperature. The following heights and temperatures were taken from a radiosonde sounding, for pressure levels usually included in a satellite sounding:

p (mb)	Z (m)	T (°k)
1000	100	291.36
850	1479	284.86
700	3080	275.56
500	5716	259.06
400	7364	246.16
300	9389	232.46
200	12023	212.46
100	16235	206.86
70	18376	207.86
50	20423	209.96
30	23628	218.26
10	30418	220.86

Using the above Z values, $\bar{T}$ for each layer was computed from the thickness hydrostatically. These "satellite layer temperatures" were converted to "satellite level temperatures" using two methods: (1) Flattery method entirely, (2) Flattery method to get 400 mb $\bar{T}$, then integrating the definition of layer mean temperature upward and downward as described earlier in this Appendix. Results are shown in the following table.

p (mb)	Actual T (°K)	Method 1 (°K)	Method 2 (°K)
1000	291.36	293.39	293.39
850	284.86	286.06	285.78
700	275.56	276.55	276.97
500	259.06	258.09	256.83
400	246.16	247.09	247.09
300	232.46	232.16	232.86
200	212.46	214.62	209.11
100	206.86	204.57	205.38
70	207.86	205.88	204.43
50	209.96	210.85	211.35
30	218.26	213.94	217.58
10	220.86	208.67	201.56

A first guess surface pressure of 1015.75 mb at the radiosonde location was used to form the basis for an interpolation of the Method 1 and 2 results to σ layer pressures. As a reference for comparison, the PTOSIG routine is used with radiosonde heights and temperatures to interpolate Z quadratically to σ levels, beginning with the first σ level above the surface (939.56 mb) since no extrapolation is allowed. Then this σ level height is used as a base for Methods 1 and 2 in the computation of Z at other levels. Temperatures at σ layers from the quadratically interpolated rawinsonde heights were also computed for comparison. All values are shown in the following table.

Sigma Layer Temperatures and Sigma Level Heights

$\hat{P}$	P	PTOSIG $\hat{Z}$	T	METHOD 1 $\hat{Z}$	T	METHOD 2 $\hat{Z}$	T
939.56		632.61		632.61		632.61	
	875.53		287.40		287.39		287.17
812.60		1857.79		1854.74		1853.79	
	735.47		278.71		278.97		279.22
660.23		3549.86		3551.43		3551.96	
	582.87		266.41		266.51		266.01
507.87		5597.21		5599.50		5596.20	
	443.30		251.50		252.16		251.58
380.90		7716.47		7724.31		7716.09	
	342.31		239.52		239.01		239.38
304.72		9282.00		9286.49		9280.72	
	279.05		228.20		229.03		228.62
253.94		10500.67		10509.61		10501.62	
	228.21		218.06		220.33		216.84
203.15		11925.91		11949.70		11918.89	
	177.32		209.32		212.88		208.46
152.36		13689.76		13743.50		13675.49	
	126.36		206.42		207.97		206.64
101.57		16141.32		16213.39		16129.60	
	75.15		206.19		205.62		204.62
50.79		20327.50		20388.03		20284.00	
	21.07		211.99		212.25		212.43
10.00		30418.00		30449.84		30395.41	

In this case, the $\hat{Z}$ values from Method 2 are in closer agreement with the
PTOSIG (method of obtaining estimates of rawinsonde Z, T on levels, layers)
values than are the Method 1 values at the 507.87 mb level and above. At the
lowest two levels they are only slightly worse. On this basis, Method 2 was
chosen to process the satellite data to produce σ level Z and σ layer T
estimates, so that their values would be most consistent with those for
rawinsondes.

APPENDIX E. Conversion of Cloud Amount to Relative Humidity

1. AFGWC Method

Percent cloud amounts are converted to condensation pressure spread (CPS)
using the curves given in Fig. E1 (data tables obtained from AFGWC/SDDN,
Offutt AFB, NE 68113). CPS is then converted to dew point depression (DPD)
on a pressure surface P (mb) using

$$DPD = CPS[4.9 + 0.93(P/1000) + 9.0(P/1000)^2]^{-1}.$$

Finally, temperatures from an appropriate source (observation or analysis) are
used to convert DPD to relative humidity.

2. ECMWF Method

Total fractional cloud cover is estimated from observed relative humidity
at layer k using

$$CLC_k = \{max[(\frac{RH_k - RHC_k}{1 - RHC_k}), 0]\}^2$$

where

$$RHC_k + 1 - 2\sigma_k + 2\sigma_k^2 + \sqrt{3}\ \sigma_k(1 - 3\sigma_k + 2\sigma_k^2) \ .$$

$$\sigma_k = P_k/P_* \ .$$

Curves of relative humidity vs. fractional cloud cover generated from this
expression are given for several mandatory pressures in Fig. E2. Solving this
expression for RH_k in terms of fractional cloud cover yields

$$RH_k = RHC + \sqrt{CLC} \ (1 - RHC_k) \quad \text{for } RH_k > RHC_k \leq 1.$$

This computation requires a knowledge of σ_k, which in turn requires a
knowledge of the model terrain surface pressure at the geographic location in
question. Thus, in the processing of the 3DNEPH data that do not include
surface pressure information, one can go only as far as calculating $\sqrt{CLC}$ for
$0.01 \leq CLC \leq 1$, bilinearly interpolating these to the desired regular
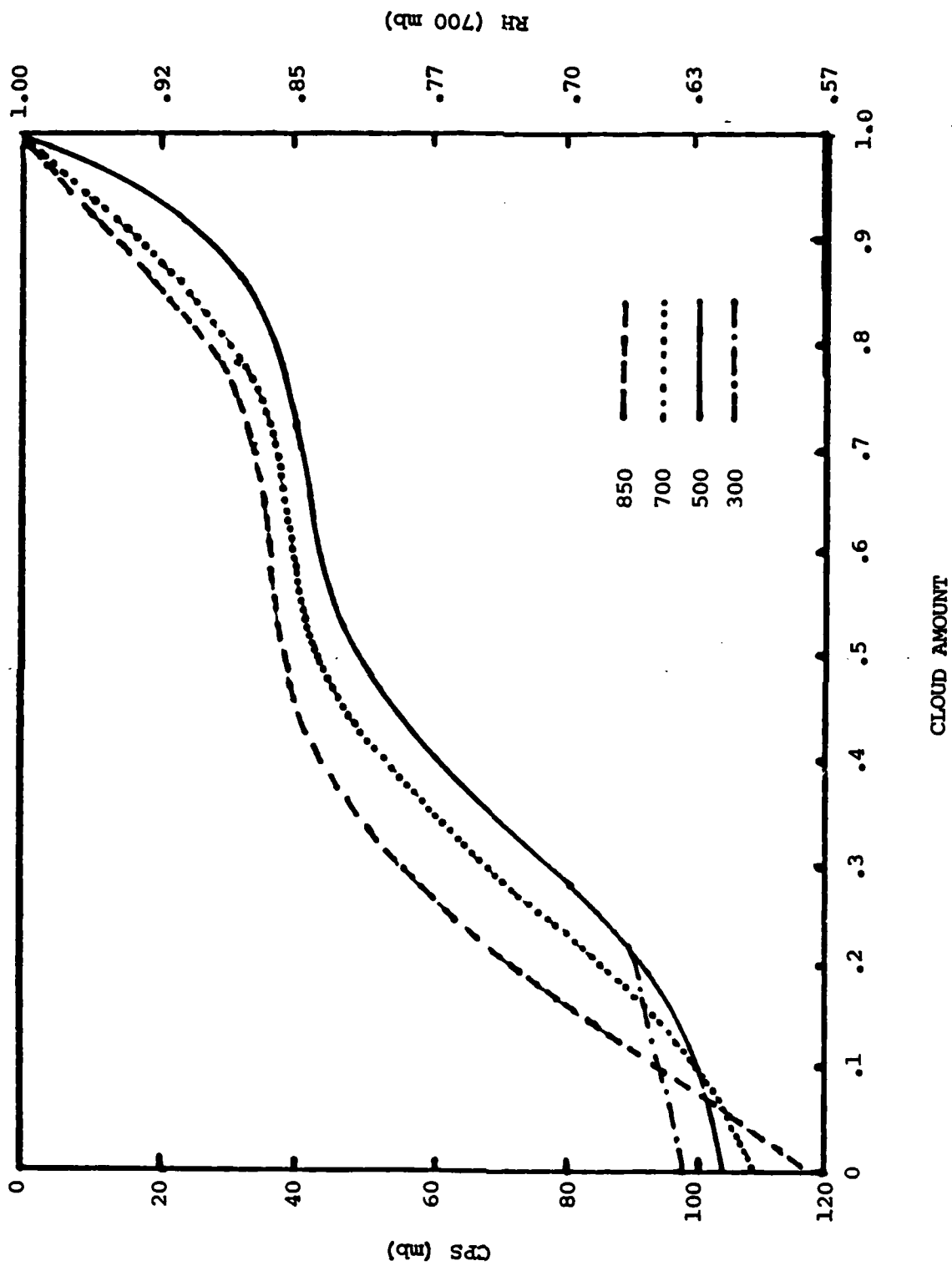
131

Fig. E1 AFGWC RH - Cloud Amount Conversion Scheme. 700 mb RH on Right Ordinate Derived from CPS Using Standard Atmosphere Temperatures.
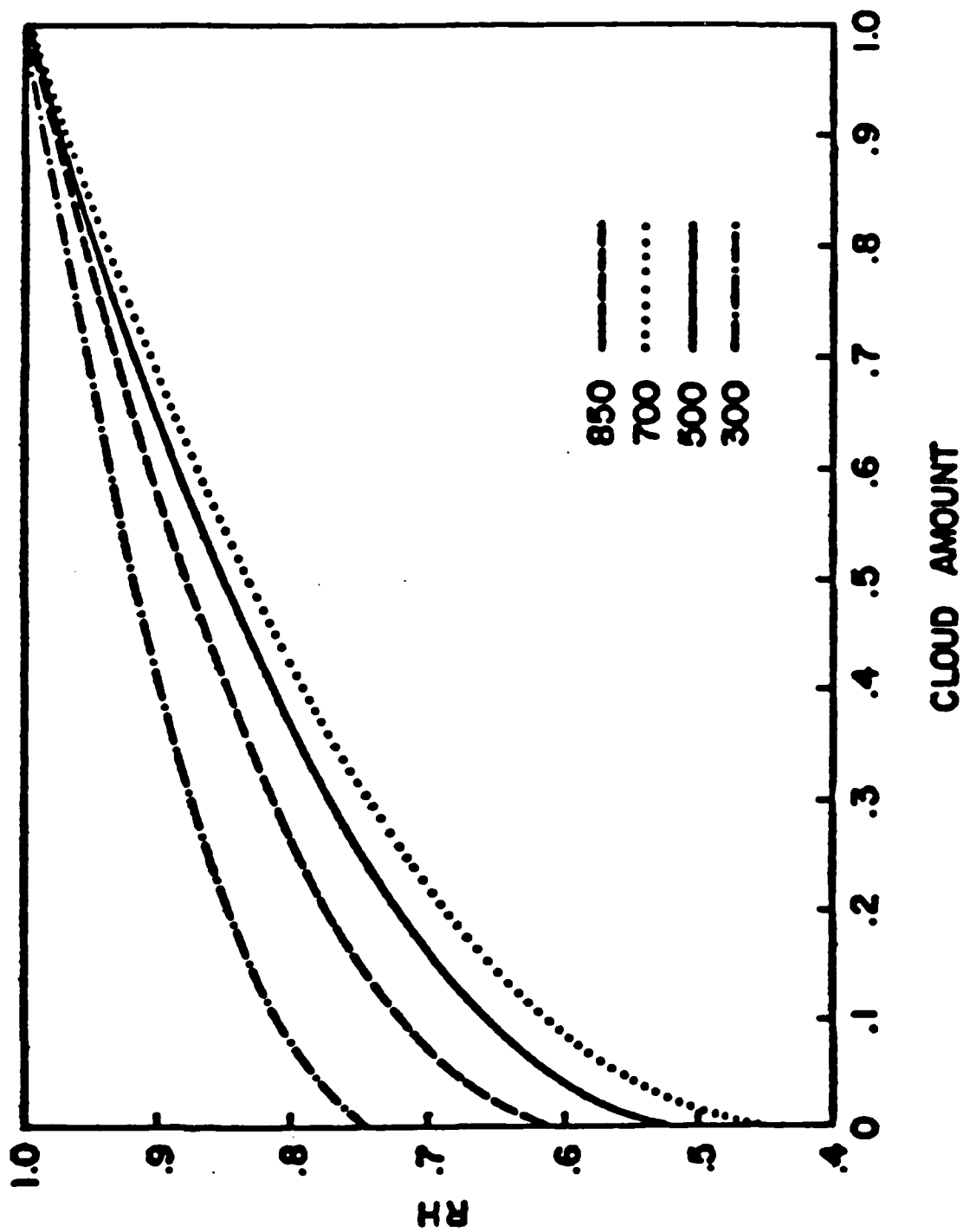
Fig. E2 ECMWF RH – Cloud Amount Conversion Scheme

latitude-longitude positions, and then later using surface pressures on the same positions to evaluate RH_k.

3. Tibaldi (from Chu-Parrish) Method

As used in the surface weather observation conversion of cloud amount to relative humidity expression

$$RH_j = M_j - A_j \cos[(\pi/100) \cdot \% \text{ cloud amount}],$$

this method simply uses percentage cloud cover for four cloud level categories to estimate relative humidity. The layers indexed by j and the corresponding values of M_j and A_j are given by

j		M_j	A_j
4	high $(p_4 - p_5)$	0.55	0.10
3	middle $(p_3 - p_4$	0.60	0.15
2	low $(p_2 - p_3$	0.75	0.15
1	P.B.L. $(p_1 - p_2)$	0.80	0.20 .

Fig. E3 shows curves of relative humidity vs. cloud amount (in eighths) as generated by this equation. The layer pressure interfaces are defined by

$$p_1 = p_*$$
$$p_2 = p_1 - 50 \text{ mb}$$
$$p_3 = p_2 - (1/3)(p_2 - p_5)$$
$$p_4 = p_3 - (1/3)(p_2 - p_5)$$
$$p_5 = 300 \text{ mb} .$$

The surface pressure p_* in the analysis is the first guess surface pressure on the model terrain. However, since no information on surface pressure of the 3DNEPH points is included with the cloud analysis, it is only possible to compute $\cos[(\pi/100) \cdot \% \text{ cloud amount}]$ at each level in the 3DNEPH processing. These values are then bilinearly interpolated to the desired positions for use in the analysis. Then the first guess surface pressures can be used to prescribe the values of $p_1 - p_5$ at each observation or analysis point, and these in turn will dictate which values of A_j, M_j to use for each of the five levels of the vertically compacted 3DNEPH cloud amount values to convert them to relative humidity.
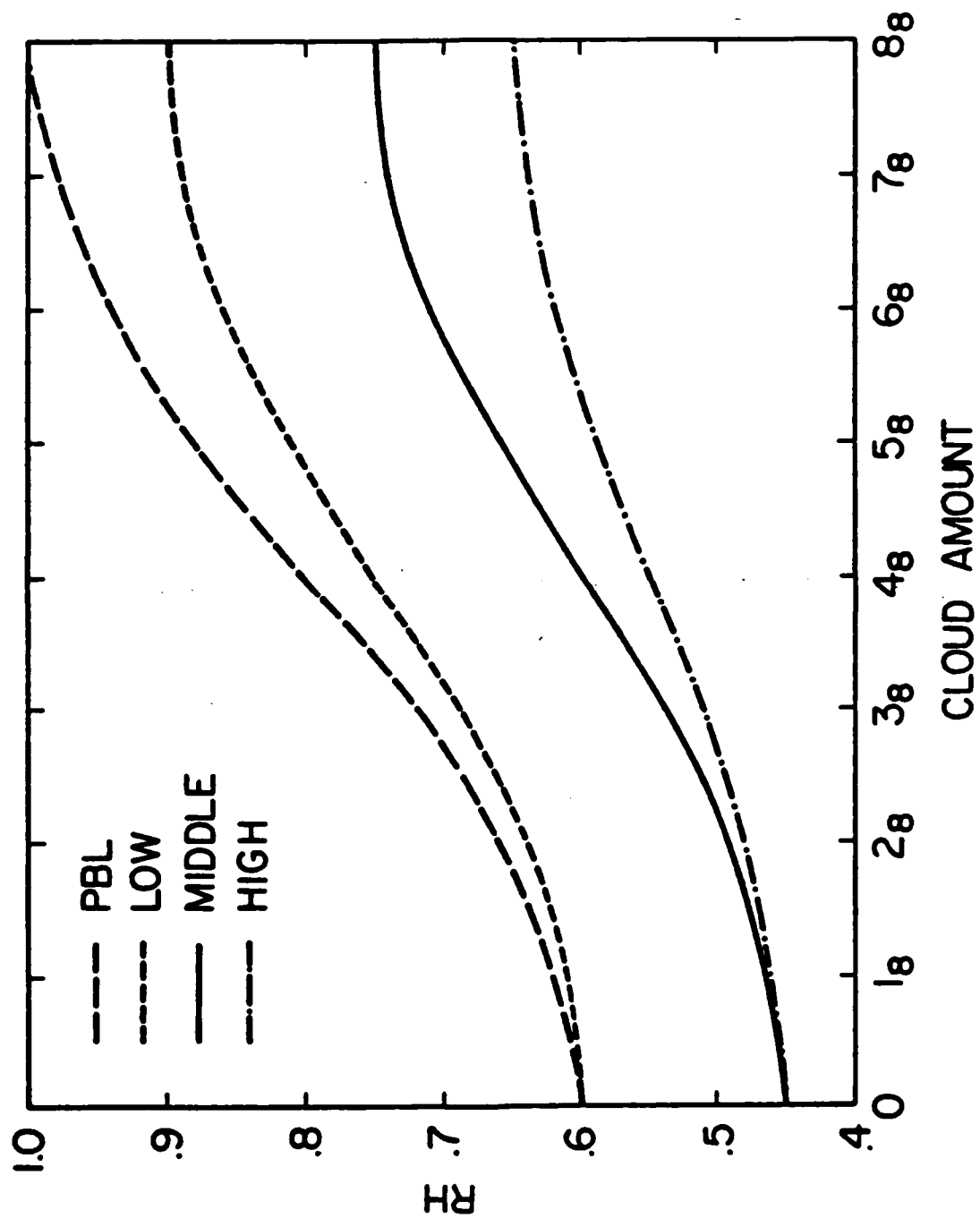
Fig. E3 MMC (Chu-Parrish) RH - Cloud Amount Conversion Scheme

APPENDIX F. NMC Subroutine GETPS

This subroutine estimates the value of $\ln p_\star$, where $p_\star$ is the surface pressure, from data on known pressure levels. The geopotential of the level where $p_\star$ is desired, the surface topography, is given and denoted by $\phi_\star$.

Assume we are given ϕ_1, ϕ_2, ..., ϕ_L, T_1, T_2, ..., T_L at the known pressure levels p_1, p_2, ..., p_L. Also, assume that ϕ is a quadratic function of $\ln p$ in an individual layer $p_k \leq p \leq p_{k-1}$ where here the indices increase upward in the atmosphere. Thus, we assume the form

$$\phi(\ln p) = \phi(\overline{\ln p}) + A(\ln p - \overline{\ln p}) + \frac{B}{2}(\ln p - \overline{\ln p})^2 \qquad (F1)$$

that satisfies the hydrostatic equation

$$\partial\phi/\partial \ln p = -RT = A + B(\ln p - \overline{\ln p})$$

so that

$$\partial^2\phi/\partial(\ln p)^2 = -R(\partial T/\partial \ln p) = B . \qquad (F2)$$

The first step is to find the levels ϕ_k, ϕ_{k-1} that surround the surface topography geopotential $\phi_\star$. Then letting

$$DH = \ln p_{k-1} - \ln p_K > 0$$

$$A = (\phi_{k-1} - \phi_k)/DH < 0$$

$$B = -R(T_{k-1} - T_k)/DH \quad \begin{array}{l} < 0 \text{ lapse} \\ = 0 \text{ isothermal} \\ > 0 \text{ inversion} \end{array}$$

$$\phi_0 \equiv \phi(\overline{\ln p}) = \frac{1}{2}(\phi_{k-1} + \phi_k) - \frac{B}{8}(DH)^2 .$$

If we let $X_\star = \overline{\ln p_\star}$, $X_0 = \ln p$, then rewriting Eq. (F1) gives

136

$$\frac{B}{2}(X_\star - X_0)^2 + A(X_\star - X_0) + \phi_0 - \phi_\star = 0 \ . \qquad\qquad (F3)$$

Using the quadratic equation to solve for $X_\star - X_0$ yields

$$X_\star - X_0 = -\frac{A \pm \sqrt{D}}{B}$$

where $D \equiv A^2 - 2B(\phi_0 - \phi_\star) \geq 0$. Choosing the + sign gives

$$X_\star - X_0 = -\frac{A + \sqrt{D}}{B} \ .$$

Rationalizing the numerator, using the definition of D, and noting that $-A = |A|$ since $A < 0$ in all cases, yields

$$X_\star - X_0 = 2(\phi_0 - \phi_\star)/(|A| + \sqrt{D}).$$

Solving for $X_\star$ and using $p_\star = \exp(X_\star)$ gives the surface pressure.

REFERENCES

1. Ballish, B. A., 1980: <u>Initialization, Theory, and Application to the NMC Spectral Model</u>. Ph.D. thesis, Univ. of Maryland, 151 pp.

2. Bengtsson, L., M. Kanamitsu, P. Källberg, and S. Uppala, 1982: FGGE 4-dimensional data assimilation at ECMWF. <u>Bull. Amer. Met. Soc.</u>, <u>59</u>, 1603-1611.

3. Brenner, S., C. H. Yang, and K. Mitchell, 1984: <u>The AFGL Global Spectral Model: Expanded Resolution Baseline Version</u>. AFGL-TR-84-0308, Air Force Geophysics Laboratory, Hanscom AFB, MA, ADA160370.

4. Bergman, K. H., 1979: Multivariate analysis of temperature and winds using optimum interpolation. <u>Mon. Wea. Rev.</u>, <u>107</u>, 1423-1444.

5. Bergman, K. H., 1978: Role of observational errors in optimum interpolation analysis. <u>Bull. Amer. Met. Soc.</u>, <u>59</u>, 1603-1611.

6. Chu, R., and D. Parrish, 1977: Humidity analysis for operational prediction models at the National Meteorological Center. NOAA NMC Office Note 140.

7. Dey, C. H., 1983: The NMC optimum interpolation procedure. Presented at NMC workshop on vector processing and the statistical analysis of meteorological data, Camp Springs, MD.

8. Dey, C. H., and L. L. Morone, 1985: Evolution of the National Meteorological Center Global Data Assmiliation System: January 1982-December 1983. <u>Mon. Wea. Rev.</u>, <u>113</u>, 304-318.

9. Fye, F. K., 1978: <u>The AFGWC Automated Cloud Analysis Model</u>. AFGWC Technical Memorandum 78-002, Offutt AFB, NE.

10. Gustafsson, N., 1981: A review of methods for objective analysis. <u>Dynamic Meteorology: Data Assimilation Methods</u>, Vol. 36, Applied Mathematical Sciences Series, L. Bengtsson, M. Ghil, and E. Källen, eds., Springer-Verlag, 330 pp.

11. Hollingsworth, A., A. C. Lorenc, M. S. Tracton, K. Arpe, G. Cats, S. Uppala, and P. Kallberg, 1983: The response of numerical weather prediction systems to FGGE II-B data. Proceedings of Workshop on Current Problems in Data Assimilation, European Centre for Medium Range Weather Forecasts, Reading, U.K., 8-10 November 1982, pp. 19-120.

12. Illari, L. 1985: The quality of ECMWF humidity analysis. Proceedings of Workshop on High Resolution Analysis, European Centre for Medium Range Weather Forecasts, Reading, U. K., 24-26 June 1985, pp. 41-68.

13. Lejenäs, H., 1979: Initialization of moisture in primitive equation models. Mon. Wea. Rev., 107, 1299-1305.

14. Lorenc, A. C., 1981: A global three-dimensional multivariate statistical interpolation scheme. Mon. Wea. Rev., 109, 701-721.

15. McPherson, R. D., K. H. Bergman, R. E. Kistler, G. E. Rasch, and D. S. Gordon, 1979: The NMC operational global data assimilation system. Mon. Wea. Rev., 107, 1445-1461.

16. Mitchell, K. E., 1985: A comparison of moisture variables in the vertical interpolations of a 4-d data assimilation system. Preprints, Seventh Conference on Numerical Weather Prediction, Montreal, Amer. Met. Soc., 310-317.

17. Morone, L. L., 1986: The observational error of automated wind reports from aircraft. Bull. Amer. Met. Soc., 67, 177-185.

18. Sela, J., 1980: Spectral modeling at the National Meteorological Center, Mon. Wea. Rev., 108, 1279-1292.

19. Slingo, J., and B. Ritter, 1985: Cloud Prediction in the ECMWF Model. ECMWF Tech. Rep. No. 46, Reading, U.K.

20. Smagorinsky, J., K. Miyakoda, and R. F. Strickler, 1970: The relative importance of variables in initial conditions for dynamical weather prediction. Tellus, 22, 141-157.

21. Stobie, J., 1984: Cholesky Method for Solving a Series of Linear Equations. TSIN Office Note 84-1, Air Force Global Weather Central, Offutt AFB, NE.

22. Tibaldi, S., 1982: The ECMWF humidity analysis and its general impact on global forecasts and on the forecast in the Mediterranean area in particular. Rivista di Meteorologia Aeronautica, 42, 309-328 (portion used in this report also available in the book Atmospheric Water Vapor, 1980, Academic Press, ISBN 0-12-208440-3).

23. Obtained from Department of the Air Force, OL-A, USAF Environmental Technical Applications Center (MAC), Federal Building, Asheville, NC, 28801.

EMD

6 — 87

DTIC